Microfluidic Droplet Generation Device with Flexible Walls

SAJAD YAZDANPARAST

A THESIS SUBMITTED TO

THE FACULTY OF GRADUATE STUDIES

IN PARTIAL FULFILLMENT OF THE REQUIREMENTS

FOR THE DEGREE OF

MASTER OF APPLIED SCIENCE

GRADUATE PROGRAM IN

MECHANICAL ENGINEERING

YORK UNIVERSITY
TORONTO, ONTARIO

JANUARY 2022

Abstract

Droplet microfluidic systems involve the controlled generation of discrete or dispersed microdroplets of one fluid (d-phase fluid) inside another immiscible fluid (continuous or c-phase fluid) inside microchannels. In the co-flow droplet generation method, the d-phase fluid flows into the c-phase fluid through parallel channels. Controlling droplet sizes is one of the most important aspects of droplet formation due to its effect on the droplets' physical and chemical properties and performance. Researchers mostly use c-phase flow rate to control the droplet size. However, c-phase flow rate based modulation is applicable only before droplet generation transitions to the high-polydispersity regimes.

We utilized a device with controllable c-phase channel size to fine-tune droplet size. Taking advantage of the increasing of the axial drag force stems from the increase of shear rate, droplet sizes can be controlled by the flexible walls of c-phase channel. The present study provides the first comprehensive investigation of the effect of channel size on the droplet size in the co-flow method to extend the range of droplet sizes generated in a single device.

The first step was to design and develop a co-flow microfluidic droplet generation device with a size-tunable channel. The proposed device was made of PDMS and planar, in which the channel width (w) can be changed from 1 to 0.3 mm. By changing channel width from 1 to 0.3 mm, two distinct regimes were observed at low d-phase Weber number (We_d), dripping (at high and medium channel widths), and plug regimes (at low channel widths). Both regimes are monodispersed. By increasing Wed such that Wed ~ O(0.1), a transition from dripping or plug to wide jetting regime was encountered in which the average polydispersity increased from 1.3% to 2.9%.

Firstly, the effect of channel width on the droplet size at the constant c-phase velocities was investigated. The diameter of droplets was inversely proportional to the root square of channel width in constant c-phase velocity or Capillary number. The design was benefited from the increased shear force due to the channel width decrease and controlled droplet size. Then, the effect of channel width on the droplet size in constant c-phase velocity and for different c-phase viscosities and channel heights was studied. The results indicated that, in a lower channel height, the effect of channel width on droplet size increased due to the enhanced role of the wall effect.

Then, the effect of channel width on the droplet size at the constant c-phase flow rates was studied. Droplet size change in the constant c-phase flow rates was more than that in the constant c-phase velocity. This is because, in the constant flow rates, a decrease in channel width not only increases the wall effect but also increases the axial velocity, which leads to a stronger drag force. The range of droplets generated in the developed device was exceptionally 111% wider compared to the reported device in which the widest range of droplets was generated.

Finally, Buckingham's Π theorem was used to develop a model for the prediction of droplet size. The model indicated that the droplet size is greatly affected by three parameters, c-phase Capillary number (Ca_c), c-phase Reynolds number (Re_c), and the ratio of channel height to channel width (h/w). The model predicted the droplet size with an average error of only 3.9 %, indicating it can be used to predict the intermediate values.

The present study has gone some way towards our understanding of the effect of channel size on droplet size under different conditions. To develop a full picture of the effect of channel size on the droplet size, additional studies will be needed with the inclusion of more parameters (e.g., interfacial tension and d-phase viscosity) and considering wider ranges of parameters (e.g., c-

phase viscosity and channel height). The proposed device showed the droplet sizes could be tuned on-demand by controlling the channel width. For the further extension of the range of droplets, the challenge now is to develop a device in which the height and width of channel can be simultaneously controlled.

Dedication

To my mother and father for their love and support throughout my life.

Acknowledgments

I would like to express my sincere gratitude to my supervisors Prof. Amirfazli and Prof. Rezai for their continuous support of my master’s study and research.

Table of Contents

List of Tables

List of Figures

Chapter 1: INTRODUCTION

1.1 Microdroplets and their applications

Microdroplets refer to micro-scale droplets of a target fluid (called dispersed or d-phase fluid) in a suspension fluid (called continuous or c-phase fluid), whose diverse applications have attracted increasing attention [1]–[3]. Single-emulsion microdroplets consist of one d-phase and one c-phase fluid (Figure 1-1 (a)), whereas more complex microdroplets (e.g., double-emulsion microdroplets in Figure 1-1 (b-d)) may include more than one d-phase fluid encapsulated in various configurations in a c-phase fluid. Microdroplets provide significant advantages in sample processing and monitoring, such as facile automation, increasing practical flexibility, decreasing analysis time, and small volumes. Molecular synthesis [4], diagnostics [5], [6], cell biology [7], [8], chemical reactions [9], imaging [10]–[12], and food processing and production [13], [14] are among their prominent applications.

One of the important applications of microdroplets is in drug delivery [15]–[17]. Microdroplets are functionally used to deliver drugs and nutrients [18]. In the pharmaceutical field, the structure of the drug is designed for a controllable release profile. Drug encapsulation in microdroplets is a promising approach that can offer excellent features in terms of packing efficiency, temporal release profile, and degradation prevention [19], [20]. The drug-environment interfacial force determines the release rate. In addition to functional properties, it is necessary to control the size and shape of drug droplets due to their direct impact on the drug effectiveness [21].

1.2 Microdroplet generation methods

Microdroplets can be generally prepared through three main methods: membrane emulsification, microchannel emulsification, and microfluidic devices. Table 1-1 briefly compared these methods.

In membrane emulsification, microdroplets are generated by passing the dispersed phase target fluid through micron-sized pores of a membrane [22]. Despite the high frequency of droplet generation due to a large number of pores, polydispersity (the ratio of the standard deviation of droplet diameter to mean diameter of droplet population [11]) is high. Moreover, controlling the droplet size and the number of droplets in double emulsions is challenging; thus, this method is not a flexible approach for generating Janus and non-spherical droplets [23].

In the microchannel emulsification method, droplets are generated in the photolithographically prepared microgrooves [24], micro-cutting in stainless steel [25], and PMMA injection molding [26]. The main drawback of this method is generating partially tunable droplets due to its fixed geometry [27]. Also, this method is low throughput compared to membrane emulsification. The maximum droplet generation frequency achieved in this method is about 40 kHz [28]. The main advantages of this method are monodispersity and highly controllability of droplet diameters [29].

Devices made by soft lithography, glass capillaries, 3D printing, or their combination are classified under the title of microfluidic devices. Microfluidic droplet generation techniques could offer all the advantages of a promising microdroplet platform. They enable the generation of droplets down to the diameter of 200 nm [30] and the production of highly monodispersed droplets [23], size-tunable single and double emulsions [31]–[33], and Janus droplets [34].

However, the major drawback of microfluidic emulsifiers is their low throughput (10^5 s^{-1}) [38], [39]compared to the membrane emulsifiers. This disadvantage can be overcome to some extent by the parallelized microfluidic emulsifiers.

Table 1-1. Comparison of membrane emulsification, microchannel emulsification, and microfluidic devices in microdroplets generation

	Membrane emulsification	Microchannel emulsification	Microfluidic devices
Minimum droplet size	0.1 µm [23]	1 µm [23]	0.2 µm [30]
Polydispersity (CV)	10-20 % [23]	CV < 5% [23]	CV < 3% [23]
Maximum droplet generation frequency (droplet/second)	10^{18} (3.72 cm^2 membrane) [23]	40000 [28]	10^5 [38], [39]
Possibility for the generation of tunable droplets	Yes (To some extent)	Yes (Almost)	Yes (Completely)
Ability to produce multi-emulsions	Yes [40]	Yes [41]	Yes [31]–[33]
Ability to produce Janus droplets	No	No	Yes [34]

1.3 Microfluidic droplet generation

In recent decades, microfluidic droplet generation has become a topic of increasing interest because of two main reasons. Firstly, microfluidic systems miniaturize device dimension, increase heat and mass transfer due to the high surface-to-volume ratio, facilitate the control of movement and interaction of samples, and allow parallelization, compartmentalization, and molecular analysis [3]. In chemical reactions, microreactor droplets can be manipulated in a controlled manner in terms of reagents mass ratio [42]–[44]. Secondly, the structure of droplets could be controlled in terms of size, reproducibility, and different combination of droplets. Microfluidic droplet generation can generate single droplet, double emulsions, multi emulsions, and Janus droplets (Figure 1-1). In these devices, the phase that is intended to be dispersed is surrounded by an immiscible carrier fluid. The phase by which droplets are generated is called a dispersed phase or d-phase, while the phase that carries droplets is called a continuous phase or c-phase (Figure 1-1 (a)).

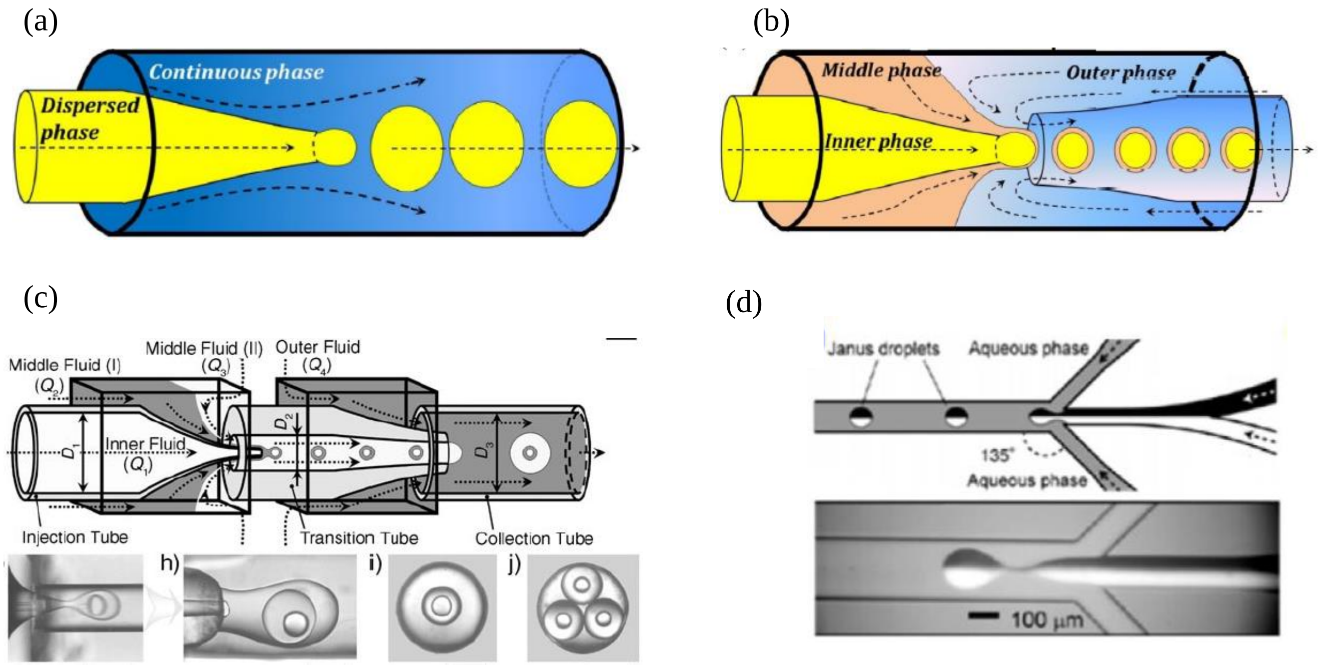

Figure 1-1. Microfluidic droplet generation methods. (a) single emulsion method. Image reprinted by permission from ref. [45], *Copyright 2019, Elsevier. (b) Double emulsions method. Image reprinted by permission from ref.* [45], *Copyright 2019, Elsevier. (c) Multi emulsions method. Image reprinted by permission from ref.* [46], *Copyright 2007, John Wiley and Sons. (d) Janus droplet generation. Image reprinted by permission from ref.* [3], *Copyright 2017, American Chemical Society.*

Two general methods have been developed in microfluidic droplet generation, i.e., passive and active methods. Active methods involve using an external force to change the force balance on the droplet during generation, in addition to the hydrodynamic effects of the flow. This external force can be electrical [47], magnetic [48], centrifugal [49], [50], optical [51]–[53], thermal [54]–[56], or mechanical [57]. In passive methods, there is no external energy or force to affect the droplet size, and the d- and c-phase fluids are only under the effect of hydrodynamic flows using upstream pumps.

Passive methods are classified into three different categories based on different arrangements and geometries of channels, i.e., flow-focusing method [58]–[65], T-junction method [66]–[77], and co-flow method [78]–[84] (Figure 1-2). In these methods, usually, the shear force applied by the c-phase fluid overcomes resistive forces such as interfacial tension and causes d-phase droplets to be pinched off. In the flow-focusing method, there is an orifice downstream of the tip of the d-phase channel. This orifice increases the shear force applied by c-phase fluid and causes the droplets to have extensively smaller sizes [1]. In the T-junction method, d-phase and c-phase channels are perpendiculars. If the channels meet at an angle other than 90°, the method is called Y-junction. In the co-flow method, d-phase fluid flows into the c-phase fluid through parallel channels.

The advantage of the co-flow method is that it allows the d-phase fluid and droplets to be fully surrounded by c-phase fluid and isolates droplets from channel walls. Therefore, it minimizes the possibility of the adhesion of droplets to the wall [1]. In the co-flow method, analysis of forces is also simpler because just two axial forces are involved (for the dripping regime, which will be described in Section 1.6.1). For the T-junction, the important forces depend on the propagation of the thread into the main channel (which will be discussed in detail in Section 1.5). In terms of fabrication, compared to co-flow devices, T-junction and flow-focusing devices are mostly made by soft lithography [58], [66].

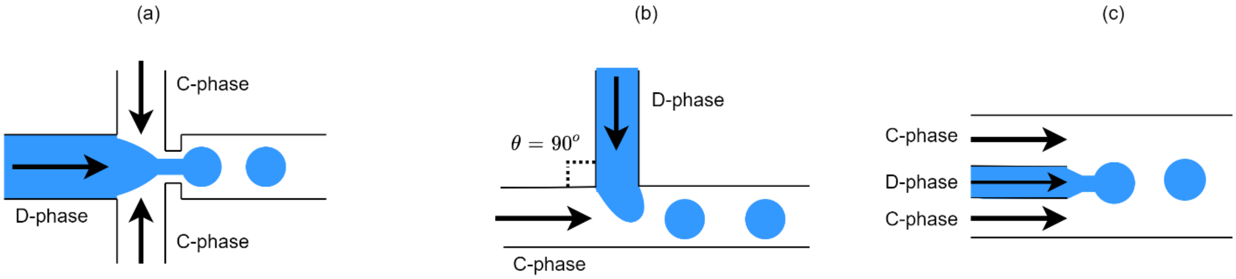

Figure 1-2. Passive microfluidic droplet generation methods. (a) Flow-focusing method, (b) T-junction method, and (c) Co-flow method

1.3.1 Important dimensionless numbers

Table 1-2 summarizes the important dimensionless numbers in microfluidic droplet generation. In low-inertia conditions, dominating forces are viscous and interfacial tension forces. The ratio of these forces is Capillary number ($Ca = \mu U/\Upsilon$ where μ, U, and Υ are viscosity, characteristic velocity, and interfacial tension, respectively) which determines the droplet size. Weber number ($We = \rho U^2 l/\Upsilon$ where ρ and l are density and characteristic length, respectively) shows the ratio of inertia to interfacial tension forces, which plays an important role in high-inertia conditions. In high-throughput devices with high d-phase velocity, the parameter of We can be more important than Ca. Reynolds number ($Re = \rho Ul/\mu$) is the ratio of inertial to viscous forces. The flow generally has a low Re in the microchannels due to the small scales. However, Re can be important in high-throughput systems [1]. Bond number ($Bo = \Delta\rho g l^2/\Upsilon$ where g is gravitational acceleration) refers to the ratio of gravitational to interfacial tension forces, which could be generally ignored in microdroplets.

Table 1-2. Important dimensionless numbers in microfluidic droplet generation

Name	Formula	Force ratio
Ca (Capillary number)	$Ca = \mu U/\gamma$	Viscous to interfacial
We (Weber number)	$We = \rho U^2 l/\gamma$	Inertial to interfacial
Re (Reynolds number)	$Re = \rho U l/\mu$	Inertial to viscous
Bo (Bond number)	$Bo = \Delta\rho g l^2/\gamma$	Gravitational to interfacial

1.4 Microfluidic droplet generation frequency

The number of droplet generator units in all microfluidic devices is low (e.g., maximum 256 parallel droplet generators (units) in Nisisako and Torii's device [39]) compared to membrane emulsifiers (10^5 pores in a 3.75 cm^2 membrane area [23]). For this reason, all microfluidic droplet generators are considered low throughput systems. Table 1-3 compares the frequency of droplet generation with microfluidic devices with one of multiple parallel droplet generators. Single droplet generators have a very low throughput. Erb et al.'s co-flow device [85] has the maximum throughput among the single droplet generators with a frequency of 1036 droplet/s. The droplet size at this frequency was 80 µm. At this size, the droplet generation frequency is limited. The reason is that further increasing of d-phase flow rate may lead to a transition to a polydisperse regime. Throughput increases with increasing the number of parallel droplet generators. Nisisako and Torii's device [39] has the highest throughput (about 1.9×10^5) by using 256 parallel channels.

Table 1-3 Droplet generation frequency in different microfluidic devices.

	Case	No. of parallel drop generators	D_d [μm]	f [1/s]	Reference
Single droplet generator	1	1	280	32	Erb et al. (2011)_1 [85]
	2	1	223	47.9	Erb et al. (2011)_2 [85]
	3	1	100	530.8	Erb et al. (2011)_3 [85]
	4	1	80	1036.7	Erb et al. (2011)_4 [85]
	5	1	126	15.9	Perro et al. (2011) [86]
	6	1	80	31.1	Deng et al. (2017) [82]
	7	1	666	6	Vijayan et al. (2019) [87]
Multi droplet generators	9	8	9.8	3.7×10^5	Bardin et al. (2013) [38]
	10	15	105	1.1×10^4	Romanowsky et al. (2012) [88]
	11	128	140	5.3×10^4	Li et al. (2009) [89]
	12	144	90.7	1.3×10^5	Nisisako et al. (2012) [90]
	13	256	96.4	1.9×10^5	Nisisako and Torii (2008) [39]

1.5 Flow focusing method

The flow-focusing method was developed by Anna et al. [58] to generate micron-sized and nearly submicron droplets by placing an orifice downstream of the thread. There are two types of channel cross-section geometries for this method, planar geometry (Figure 1-3 (a)) and circular geometry[a] (Figure 1-3 (b)). Making planar devices practically is easier by soft lithography fabrication. Cubaud et al. [61] characterized five different regimes for this method, i.e., threading, jetting, dripping, tubing, and viscous displacement. Figure 1-4 shows the regime map and different regimes for this method.

---

[a] In the flow-focusing method, the needle or capillary is placed before the orifice.

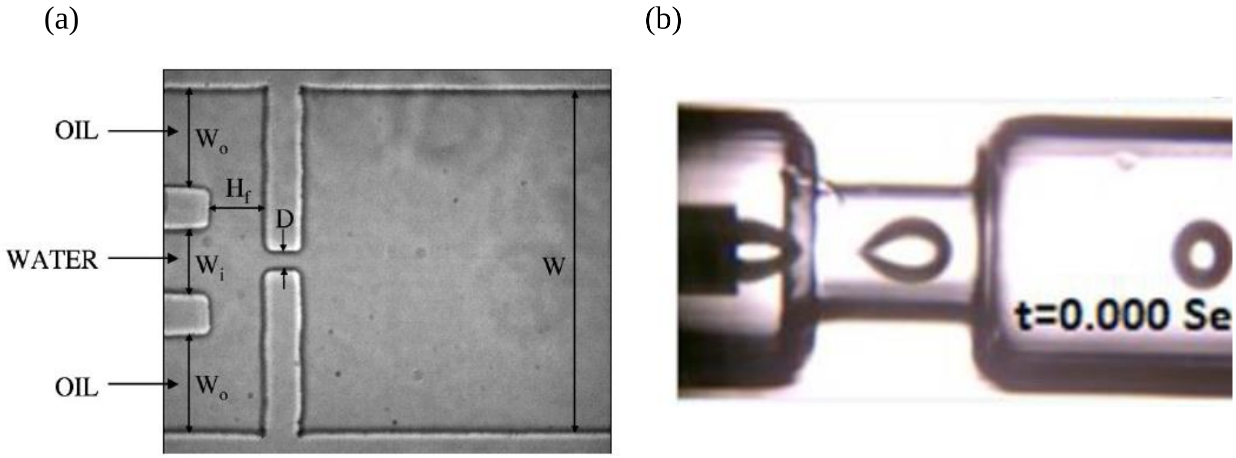

Figure 1-3. Different geometries used in the flow-focusing method, (a) Planar geometry. Image reprinted by permission from ref. [58], *Copyright 2003, AIP Publishing. (b) Circular geometry. Image reprinted by permission from ref.* [64], *Copyright 2003, Elsevier.*

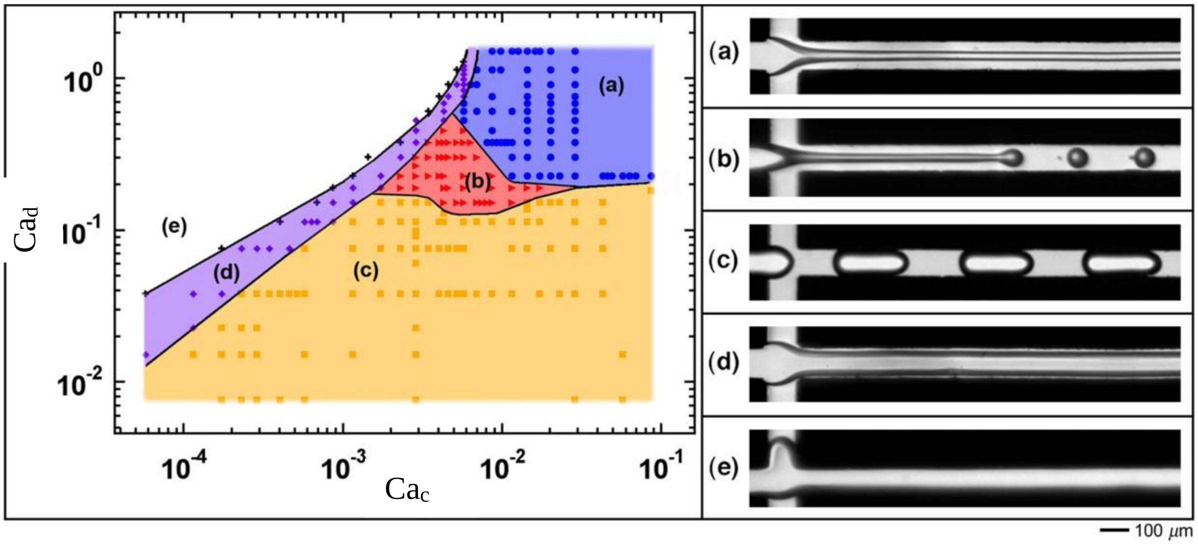

Figure 1-4 Map of regimes in flow-focusing method, (a) threading (●), (b) jetting (▶), (c) dripping (■), (d) tubing (♦), and € viscous displacement (+). Image reprinted by permission from ref. [61], *Copyright 2008, AIP publishing.*

In the threading regime, two coaxial flows are formed when c-phase viscosity is lower than d-phase viscosity ($Ca_c >> 0.1$). This phenomenon occurs even when the fluids are miscible under the same conditions ($\mu_c/\mu_d << 1$) [91]–[93]. Jetting regime can be observed when $0.1 < Ca_d < 0.5$. In this regime, due to the varicose perturbation and Rayleigh-Plateau instability, droplets as small as the jet are pinched off. The size of the droplet in this regime only depends on the flow rates of the d-phase and c-phase [61]. In the dripping regime, droplets are formed right at the end of the d-phase channel. This regime is seen at low $Ca_c < 0.1$ and $Ca_d < 0.1$. Dreyfus et al. [59] showed the importance of the wetting properties of channels. As droplet size is strongly affected by several parameters (c-phase flow rate, fluid viscosity, and channel geometry [60], [62], [64], [65]), the models proposed for this method are usually complicated.

1.6 T-junction method

Droplet generation in a T-shaped channel was introduced by Thorsen et al. [66]. The T-junction method involves three general regimes: squeezing, dripping, and parallel [94]. The ratio of the width of dispersed phase channel (w_d) to that of the continuous phase channel (w_c) ($x = w_d/w_c$) (Figure 1-5) determines the types of regimes for T-junction droplet generation which are discussed below.

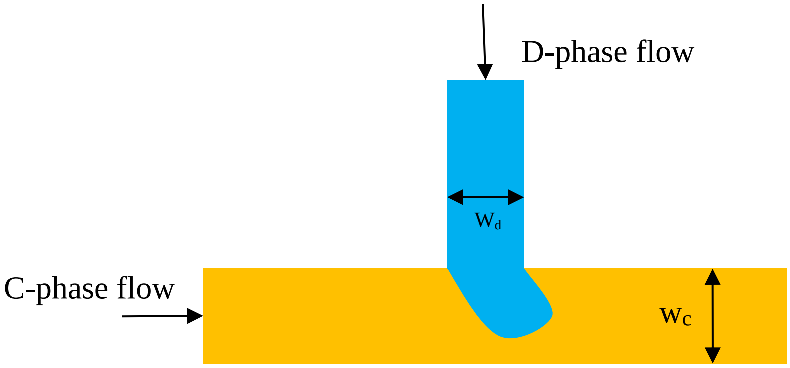

Figure 1-5. Geometry of T-junction droplet generation method

1.6.1 Break-up in the squeezing regime

The squeezing regime occurs at low capillary numbers at some specific channel geometries. In this regime, the width of the channel should be larger than the height of the channel; moreover, the width of the d-phase channel should be more than half of the width of the c-phase channel [70], [75]. The process of droplet formation in the squeezing regime of T-junction involves four steps. At first, the d-phase flow enters the main channel and forms an interface with the c-phase fluid (Figure 1-6 (a-b)). C-phase flow rate is low and cannot pinch off the d-phase stream by its shear force; therefore, d-phase fluid enters the main channel further until it blocks the main channel completely (Figure 1-6 (c)). During and after blockage of the main channel, the pressure behind the plug increases (by Bernoulli equation), pushing forward the interface between the two fluids until reaching the downstream edge of the d-phase channel (Figure 1-6 (d)). Then, the plug is pinched off, and the c-phase flow carries it to the outlet [70].

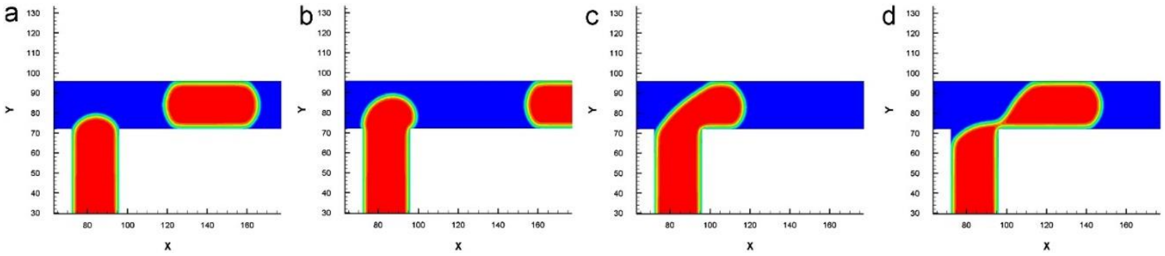

Figure 1-6. Droplet formation steps of squeezing regime in T-junction; the contour shows the volume fraction of phases in which the red color is for d-phase and blue color is for c-phase. Image reprinted by permission from ref. [77], *Copyright 2013, Elsevier.*

By using the above observations, the plug length (L) in T-junction is proved to be proportional to the ratio of d-phase to c-phase flow rates using Equation 1-1 [77]:

$$L/w_c = 1 + \alpha \frac{Q_{d-phase}}{Q_{c-phase}} \tag{1-1}$$

where α is a fitting parameter. Eq. 1-1 implies that droplet size does not depend on the properties of fluids which has been experimentally validated in [73]. The effect of flow rates on the plug length in Eq. 1-1 was confirmed in [69]–[71], [73], [74], [77].

1.6.2 Break-up in the dripping regime

In the dripping regime, due to the dominant effect of viscous forces, the d-phase thread does not block the main channel. There are three steps in the dripping regime until break-up. First, the d-phase stream enters the main channel and grows (Figure 1-7 (a-c)). In the second step, the momentum of the c-phase pushes the interface toward the edge of the d-phase channel downstream (Figure 1-7 (d)). In the third step, the droplet is pinched off and is carried by c-phase

(Figure 1-7 (e)). There is a small window of Ca in which droplet is generated in the dripping regime[b] [72].

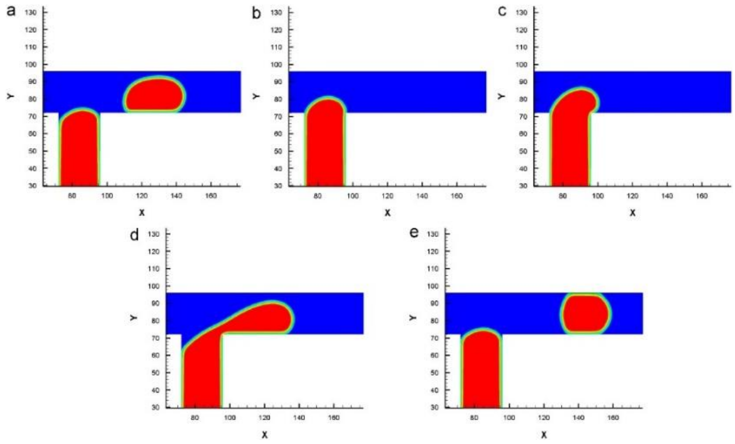

Figure 1-7. Droplet formation steps of the dripping regime in T-junction. (a-c) d-phase entering the main channel followed by growing. (d) the interface moves towards the d-phase channel edge at the downstream. (e) Droplet being pinched off; the contour shows the volume fraction of phases in which the red color is for d-phase and blue color is for c-phase. Image reprinted by permission from ref. [77], *Copyright 2013, Elsevier.*

1.6.3 Break-up in the jetting regime

Jetting regime occurs upon the enhancement of the d-phase flow rate [68]. Yang et al. [77] reported that this regime occurs when the Ca is equal to 0.056 and Q_d/Q_c exceeds 0.5; these values, however, depend on the device geometries and the properties of the fluid [76]. In this regime, the shear force pushes the d-phase stream to the bottom wall of the main channel, and a jet of d-phase fluid is formed (Figure 1-8 (a)). Because droplet pinching off is due to the interface instabilities, the generated droplet is polydisperse. The jet elongates gradually until the

---

[b] Authors use different definition for the regimes in T-junction. When said dripping regime, they mean generation of droplet at T-junction. In other words, generation of droplet without forming jet.

parallel flows occur, as shown in Figure 1-8 (e). Therefore, no droplets are generated in this regime.

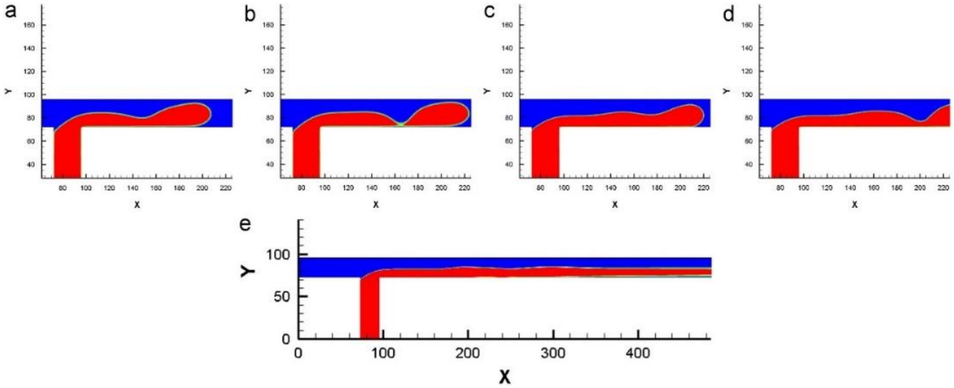

Figure 1-8. Evolution of jetting regime to parallel flow (a) t=4600 s, (b) t=5000 s (c), 29600 s, (d) 30200 s, and (e) 60000 s; the contour shows the volume fraction of phases in which the red color is for d-phase and blue color is for c-phase. Image reprinted by permission from ref. [77], *Copyright 2013, Elsevier.*

1.7 Co-flow method

The co-flow method was first introduced by Cramer [78]. Two flows join in parallel channels. There are two kinds of c-phase channels for the co-flow method, circular (Figure 1-9 (a)) and planar (Figure 1-9 (b)). The planar device is easily fabricated by soft lithography technique [95], while the circular devices are mostly fabricated by making an assembly of needles and transition tube in a square channel (to ensure the coaxial geometry) [46], [79], [80], [96] (Figure 1-10 (a)), or 3D-printing [45], [87], [97]–[99] (Figure 1-10 (b)). Three regimes are presented in the co-flow droplet generation method, i.e., dripping, narrow jetting, and wide jetting. The transition between these regimes depends on Ca of the c-phase flow and We of the d-phase flow [79], which will be discussed in the following sections.

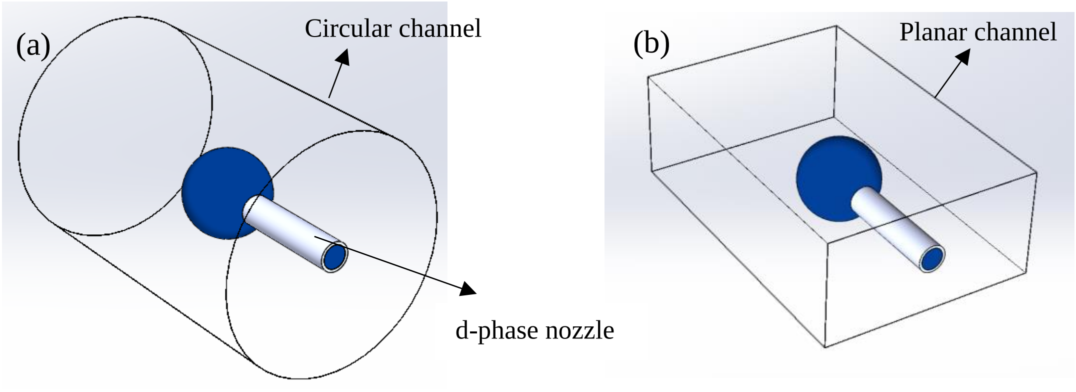

Figure 1-9. Different geometries used in the co-flow method, (a) Circular geometry, (b) Planar geometry

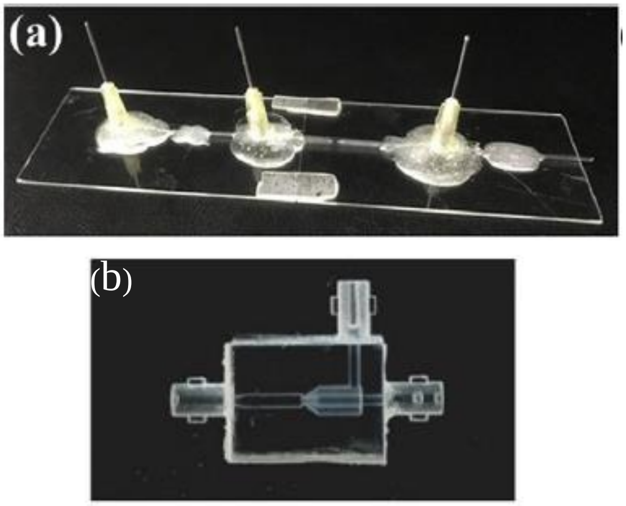

Figure 1-10. Different fabrication techniques for the co-flow method by (a) assembly of the capillary, circular channel, and square glass. The square glass is used to ensure that the capillary and circular channel are coaxial (Image reprinted by permission from ref. [45], *Copyright 2019, Elsevier) or by (b) 3D printing technique (Image reprinted by permission from ref.* [97], *Copyright 2019, Springer Nature)*

1.7.1 Dripping regime

At low velocities of the c-phase flow (Ca < 0.1, Figure 1-11), the applied viscous force on the droplet will be low, allowing the droplets to have a size in the order of injector tip size. This regime has no jet, and the instability is absolute [10]. In absolute instability, the perturbations progress in both downstream and upstream directions [100], [101]. In this kind of instability, perturbations come from the system giving rise to monodispersed droplets in the dripping regime. The polydispersity in this regime is less than 3% [102].

In the dripping regime, the droplet is generated when viscous force (F_τ) and surface tension force (F_γ) become equal ($F_\tau \sim F_\gamma$), which can roughly be written as $\mu_c u_c D_d \sim \gamma D_n$ [103] (D_d, D_n, μ_c, u_c, and γ are droplet diameter, nozzle diameter, c-phase viscosity, c-phase velocity, and interfacial tension coefficient, respectively). Therefore, droplet diameter can be estimated by:

$$D_d \sim \frac{\gamma D_n}{\mu_c u_c} \xrightarrow{\frac{\gamma}{\mu_c u_c}=\frac{1}{Ca}} D_d \sim \frac{D_n}{Ca_c} \qquad (1\text{-}2)$$

where Ca_c is the capillary number of the c-phase. As can be seen from Eq. 1-2, Ca_c has an adverse effect on the diameter of generated droplets. D-phase velocity mostly affects droplet generation frequency until the transition to the wide jetting regime. It is worth mentioning that it has a weak direct effect on the droplet size.

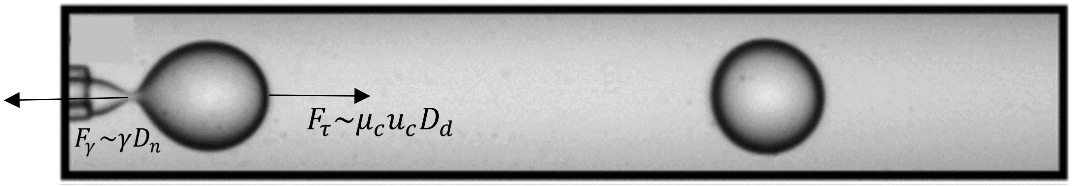

Figure 1-11. Dominant forces on a microdroplet in the dripping regime of the co-flow method. Image reprinted by permission from ref. [79], *Copyright 2007, American Physical Society.*

1.7.2 Narrow jetting regime

With increasing the velocity of c-phase flow ($Ca_c > 0.1$), viscous force becomes dominant over interfacial tension, giving rise to the transition to the narrow jetting regime (Figure 1-12 (a)). The high viscous force elongates d-phase stream, resulting in a narrow jet. Rayleigh-Plateau instability breaks up the jet in this regime [79]. Due to the Laplace pressure, the pressure at point A is larger than the pressure at point B, which drives the flow in the jet towards the neck (Figure 1-13 (b)). As a result, the jet is pinched off from point A:

$$P_A - P_{out} = \frac{\gamma}{R_A}, P_B - P_{out} = \frac{\gamma}{R_B} \rightarrow P_A > P_B \tag{1-3}$$

Droplet sizes in this regime are less than the nozzle diameter [1]. Polydispersity value in narrow jetting regime is higher than dripping regime because of perturbations moving along the jet interface [83].

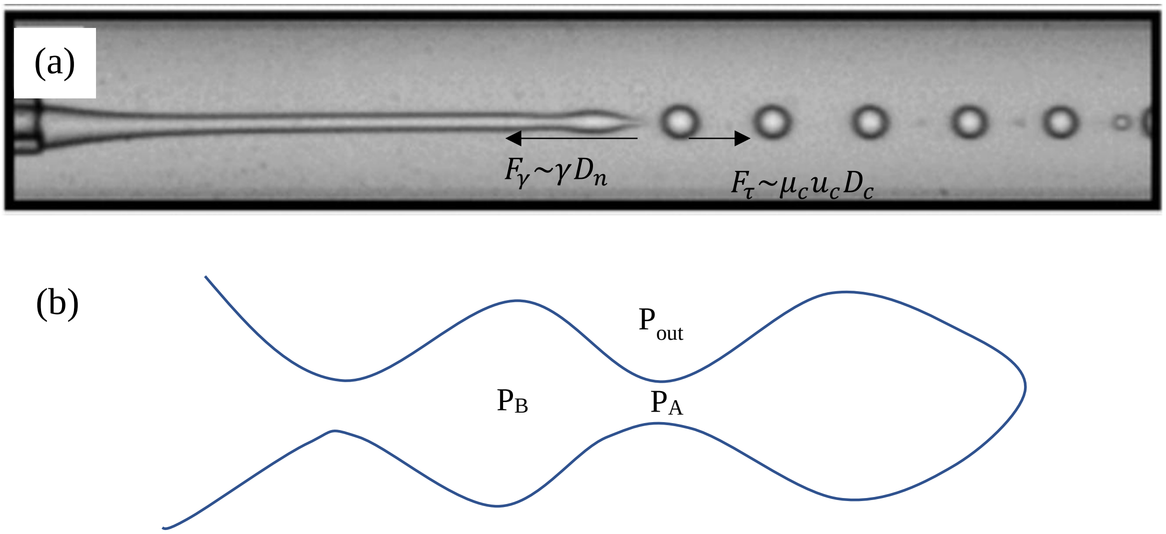

Figure 1-12. (a) Narrow jetting regime in the co-flow droplet generation method [79]. *Image reprinted by permission from ref.* [79], *Copyright 2007, American Physical Society. (b) Rayleigh-Plateau instability in a jet*

1.7.3 Wide jetting regime

Wide jetting regime occurs at high d-phase ($We_d > 1$) and low c-phase ($Ca_c < 1$) flow rates (Figure 1-13). The forces important in this regime are inertial and surface tension forces. There is a jet in this regime because of the high inertia of d-phase; moreover, droplets are larger because more liquid is injected into the channel. Inertial forces are dominant in this regime. For the wide jetting regime, the pinch-off can be assigned to absolute instability due to the decrease of We_d [11]–[14]. Figure 1-13 shows the three steps in which this instability causes droplets to pinch off. First, the Ca_c increases while the amplitude of oscillations grows until droplets as large as channel size are generated (Figure 1-13 (a)). In step 2, the oscillations become stable, and the rate of jet length changes with sharp increases of Ca_c (Figure 1-13 (b)). From step 2 to step 3, the jet length and jet neck grow, and droplets are pinched off when $We_{d,\ tip} \leq O(1)$ while $We_{d,\ injection} > O(1)$ (Figure 1-13 (c)) [81], [104].

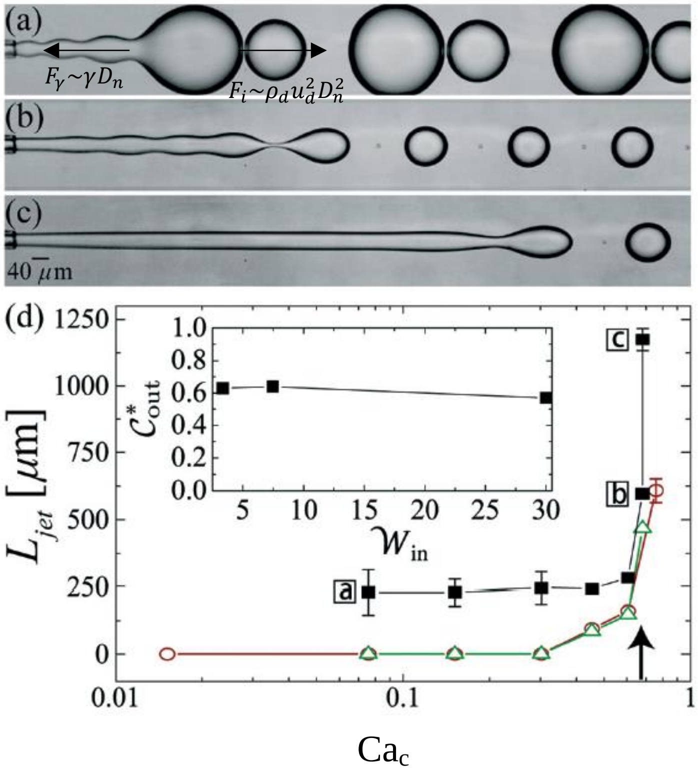

Figure 1-13. Stages in wide jetting regime break-up, (a) Increasing Ca_c to 0.69, (b) Oscillations become stable, (c) Droplets are pinched off at $We_d < O(1)$, (d) The change of jet length versus Ca_c. Image reprinted with permission from Ref. [81], *Copyright 2008, American Physical Society.*

1.7.4 Dripping to jetting transitions

Figure 1-14 shows the borders of regimes in the co-flow method in which the regimes are determined by two dimensionless numbers of Ca_c and We_d. At low Ca_c ($Ca_c < O(1)$) and We_d ($We_d < O(1)$), the droplet generation regime is dripping. At low Ca_c ($Ca_c < O(1)$) and high We_d ($We_d > O(1)$), the droplet generation regime is wide jetting regime. At high Ca_c ($Ca_c > O(1)$), the droplet generation regime is in the narrow jetting regime.

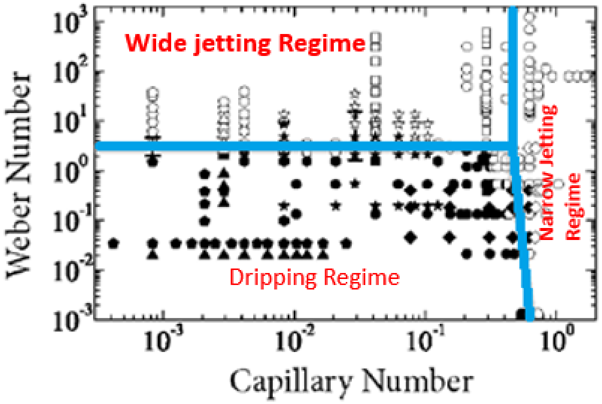

Figure 1-14. Borders of transitions from the dripping regime to the narrow jetting regime and the wide jetting regime based on Capillary Number of c-phase flow and Weber Number of d-phase flow. Image reprinted by permission from ref. [79], *Copyright 2019, American Physical Society.*

1.8 Droplet size range

Table 1-4 shows droplets generated in different microfluidic generation methods. The works listed have two criteria. Firstly, the droplets are generated in a monodispersed regime, dripping or squeezing regime. Secondly, they provided full details of their experiments, including fluids properties and geometry. Parameter D_c is the channel diameter for circular channels while w and h denote channel width and height, respectively, in rectangular channels.

In the flow-focusing method, channel size is the size of the orifice. In this method, droplet sizes are generally less than 100µm, except in the Rahimi et al. simulations [64], in which they used a large orifice (Dc = 450 µm). The interesting point about flow-focusing cases in Table 1-4 is its high Ca_{max} as this method was developed to apply high shear force on the thread, as a consequence, it generates smaller droplets compared to the co-flow method. Using small orifices in this method is a geometrical limitation for generating larger droplets.

In the T-junction method, droplet size is from 20 to 200 µm depending on the channel size and the break-up regime. The droplet size is generally larger in the plug regime as the thread occupies the whole channel, Ca_{max} in this method should not exceed 0.5 as the flow regime will be parallel, and the droplets will not be generated at all. In the co-flow method, droplets are wider in terms of size because the channel size used in this method is larger compared to the two other methods, generating larger droplets. The co-flow method has its own limitations. The range of droplets generated in this method also is limited by Ca, which should be less than 0.1 to have monodispersed droplets.

Relying just on the c-phase flow rate to change the droplet size with a wide range is not sufficient. If the flow rate exceeds a certain value, the viscous force becomes dominant, leading to the formation of a narrow jet. The droplets in this regime are not monodispersed. Moreover, the geometry of the channel limits the generation of large droplets. The range of droplet sizes can be thus expanded more by using channels with flexible walls. This work was aimed to investigate the possibility of using moving-wall structures to control the droplet size.

Table 1-4. Droplet size generated in different microfluidic droplet methods

	Case	Dc [μm]	w [μm]	h [μm]	μc [mPa.s]	Dn [μm]	ϒ [mN/m]	Ca_min	Ca_max	Dd_min [μm]	Dd_max [μm]	Dd change %	Reference
Flow-focusing method	1	NA	100	100	50	80	27	0.01235	0.12346	50	100	50	Cubaud et al. [2008][61]
	2	NA	49	96	40	126	4	0.29526	5.90514	20	60	66	Lee et al. [2009]
	3	NA	71	190	40	186	4	0.20591	0.82366	65	110	41	Lee et al. [2009]
	4	NA	45	68	40	99	4	0.90777	2.26943	48	79	39	Lee et al. [2009]
	5	450	NA	NA	86.4	250	26.3	0.03750	0.10700	150	500	70	Rahimi et. al [2019] [64]
	6	450	NA	NA	86.4	450	26.3	0.03750	0.10700	280	631	56	Rahimi et. al [2019] [64]
	7	450	NA	NA	86.4	650	26.3	0.05000	0.10700	590	805	36	Rahimi et. al [2019] [64]
T-junction method	8	NA	130	75	56.7	16	26	0.15456	0.54097	12	20	67	Okushima et al. [2004] [105]
	9	NA	150	90	1	106	26	0.00300	0.10216	74.2	84.8	14	Okushima et al. [2004] [105]
	10	NA	NA	NA	1	NA	26	NA	NA	150	225	50	Nisisako et al. [2005] [106]
	11	NA	100	33	10	50	35	0.0012	0.0476	85	196	131	Garstecki et al. [2006] [70]
	12	NA	100	33	100	50	35	0.0012	0.2410	85	196	131	Garstecki et al. [2006] [70]
	13	NA	NA	NA	NA	NA	NA	0.0020	0.0100	123.4943	216.115	75	Gupta et al. [2010] [74]
	14	NA	150	50	100	66.6	45.5	0.0001	0.5000	108	185	71	Christopher et al. [2008] [73]
Co-flow method	15	600	NA	NA	NA	40	25.4	NA	NA	255	553	54	Chu et al. (2007) [107]
	16	559	NA	NA	1.2	41	14	0.00002	0.00096	280	550	49	Erb et al. (2011) [85]
	17	396	NA	NA	1.2	47.4	14	0.00012	0.00191	223	389	43	Erb et al. (2011) [85]
	18	224	NA	NA	1.2	47	14	0.00037	0.00598	100	200	50	Erb et al. (2011) [85]
	19	111	NA	NA	1.2	45.4	14	0.00151	0.00985	80	100	20	Erb et al. (2011) [85]
	20	150	NA	NA	1	40	0.7	0.00034	0.01011	126	241	48	Perro et al. (2011) [86]
	21	300	NA	NA	49.5	40	19.4	0.10528	0.51137	80	168	43	Deng et al. (2017) [82]

1.9 Devices with flexible walls

Some researchers used the wall effect to control droplet size. Lin et al. [108] developed a T-junction device in which the size of the main channel could be changed by air pressure (Figure

1-15 (a)). By decreasing the width of the main channel from 29 to 24 μm (Figure 1-15 (b)), they showed a linear decrease in droplet size from 50 to about 20 μm (Figure 1-15 (c)). This shows the potential of controlling droplet size in the T-junction by pressing the wall of the main channel. Therefore, the strategy of a flexible wall may allow the generation of droplets over a wider range. Wu et al. [109] also showed that the droplet sizes could be tuned by pressing the top of the main channel at constant flow rates to decrease channel height. Therefore, a decrease in either height or width of the channel declines the droplet size due to the rise in shear forces.

Some computational studies examined the wall effect in the co-flow method using distinct channels rather than a single flexible one. Zhang [110] predicted an 80% increment in the size of the droplet with a 70% decrease in channel size (Figure 1-16 (a)). He said that the presence of walls deforms the thread to a prolate ellipsoid shape, giving the droplet more time for pinching off. On the other hand, Deng et al. [82] predicted an opposite trend. They predicted that a 95% reduction in channel size leads to a 66% decrease in droplet size (Figure 1-16 (b)). Based on them, a rise in wall effect enhanced the disturbances by the ambient fluid, which leads to a decrease in droplet size. Although some computational studies have been carried out, no single-device experimental study exists which investigate the effect of channel size on droplet size in the co-flow method under different conditions.

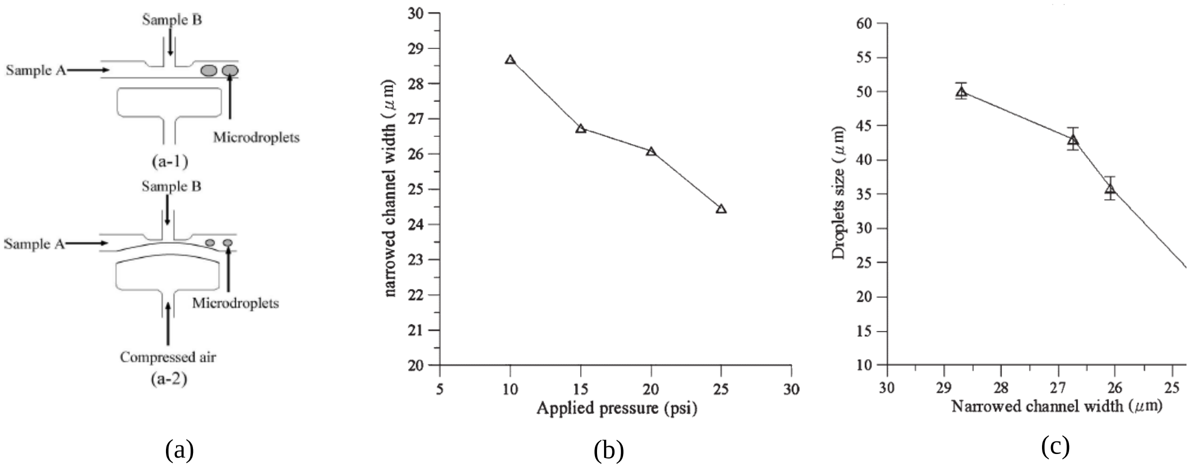

Figure 1-15. Schematic view of the device in which width of the main channel in the T-junction method is pressed for tuning the size of droplets. (a-1) Channel without deformation. (a-2) Pressed channel. (b) Change in width of channel versus applied pressure. (c) Change in droplet size versus the size of the deformed channel. Image reprinted by permission from ref. [108], *Copyright 2008, IEEE.*

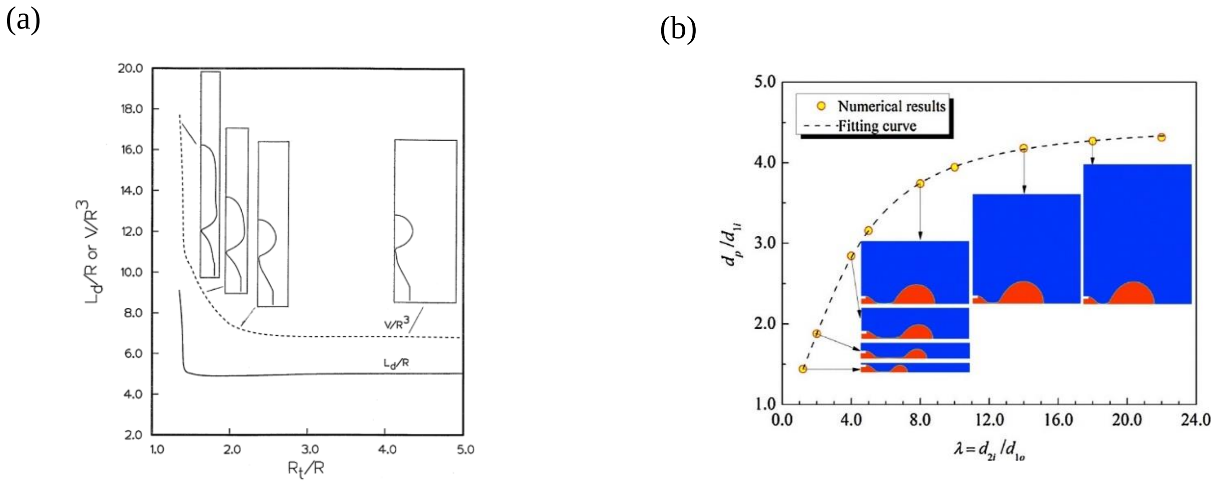

Figure 1-16. Contradictory prediction of wall effect on droplet size, (a) predicting an increase in droplet size with reduction of channel size (L_d, V, R_t, and R are plug length, plug volume, channel radius, and nozzle radius, respectively). Image reprinted by permission from ref. [110], *Copyright 1999, Elsevier. (b) a decrease in droplet size with channel size reduction (d_p, d_{1i}, d_{2i}, and d_{1o} are droplet diameter, the inner diameter of the nozzle, the inner diameter of channel, and the outer diameter of the nozzle, respectively). Image reprinted by permission from ref.* [82], *Copyright 2017, Elsevier.*

1.10 Thesis Statement and Objectives

The ultimate goal of this project is to generate droplets over a wide range of sizes by a single co-flow device with flexible walls. The objectives to reach this purpose can be summarized as:

Objective 1: Design and fabrication of a device with tunable channel size (Chapter 3)

Objective 2: Study of the effect of channel size on droplet size under different conditions considering parameters such as c-phase velocity (u_c), c-phase viscosity (μ_c), channel height (h), c-phase flow rate (Q_c), and d-phase flow rate (Q_d) (Chapter 4)

Objective 3: Generation of microdroplets over a wide range of sizes, from about 100 to 1000 μm by a single device (Chapter 4)

Objective 4: Develop a model to predict the size of droplets (Chapter 4)

Chapter 2: WORKING PRINCIPLES AND METHODS

2.1 Correlations in microfluidic droplet generation

Table 2-1 shows some correlations developed for passive methods. Here, just the correlations proposed for the monodispersed regimes are discussed. The effect of geometrical parameters on droplet size is included in all methods. The most complicated correlations are represented for the flow-focusing method as the droplet size is a function of many geometrical parameters such as orifice length and radius and the distance of capillary tip to the orifice. For the T-junction method in the plug regime, Eq. 2-3 was analytically developed. Controlling droplet generation frequency by d-phase flow rate is not possible in this method as it linearly increases the plug length. Eq. 2-4 to 2-6 were developed for the dripping regime in the co-flow method. In Eq. 2-4 and 2-5, the same exponents have been used for Q_d and Q_c, while many works have proved that the droplet size is mostly affected by Q_c rather than Q_d [78], [82], [84]. Eq. 2-6 is the most complete one and considered all important dimensionless numbers affecting the droplet size, including K (wall effect factor), Ca_c, Ca_d, and Re_d. The correlation shows when $\lambda = D_n/D_c$ is less than 8, the wall effect on droplet size significantly increases.

Table 2-1. Correlations developed for passive microfluidic droplet generation methods

Method	Regime	Equation	Parameters	Eq./Ref.
Flow-focusing	Dripping	$Ca_{crit.}\overline{D}^4 + (\bar{Q}_c + \bar{Q}_d)\overline{D}^3 - (Ca_{crit.}\overline{w}_{or}^2 + \bar{Q}_c + \bar{Q}_d)\overline{D}^2 - \bar{Q}_d\overline{w}_{or}^2\overline{D} + \bar{Q}_d\overline{w}_{or}^2 = 0$	$\overline{D} = \frac{D_d}{D_n}, \overline{w}_{or} = \frac{D_c}{D_n}$ $\bar{Q}_c = {}^{Q_c}/_{Q_o}, \bar{Q}_d = {}^{Q_d}/_{Q_o}$ $Ca_{crit.} = 0.1$	(2-1) /[85]
	Jetting	$\frac{V}{hw_c^2} = \alpha_f + \varsigma_f(\frac{Q_d}{Q_c})$	$\alpha_f = V_{EF}^* - V_{BF}^*$ $\varsigma_f = V_{EN}^* - V_{BN}^* + V_{gutter}^*$	(2-2) /[111]
T-junction	Squeezing	$L/w = 1 + \alpha\frac{Q_d}{Q_c}$	α: Fitting parameter	(2-3) /[70]
Co-flow	Dripping	$D_d = D_n^3(a\left({}^{Q_d}/_{Q_c}\right) + b)$	a, b: Fitting parameters	(2-4) /[46]
		$D_d = A({}^{Q_c}/_{Q_d})^{-\alpha}$	A, α: Fitting parameters	(2-5) /[86]
		$D_d = 0.234.D_nK.Ca_c^{-0.312}.Ca_d^{0.187}.Re_d^{-0.203}$	$K = {}^{0.327}/_{\lambda^{-1.765}} + 0.095 + 1.039$ $\lambda = \frac{D_n}{D_c}, Ca_c = {}^{\mu_c u_c}/_{\sigma}$ $Ca_d = {}^{\mu_d u_d}/_{\sigma}, Re_d = {}^{\rho_d D_n u_d}/_{\mu_d}$	(2-6) /[82]
	Narrow jetting	$D_{jet} = D_c(\frac{(1 + \varphi\lambda)^{1/2} - 1 - \varphi}{\lambda - 2 - \varphi})^{1/2}$	$\varphi = \frac{Q_d}{Q_c}, \lambda = \frac{\mu_d}{\mu_c}$	(2-7) /[112]
	Wide jetting	$D_{jet} = \sqrt[3]{\frac{4Q_d}{\pi\omega_{i,max}}}$		(2-8) /[113]

2.2 Wall effect

In fluid dynamics, in the absence of walls, the drag force on a sphere is generally expressed in terms of Reynolds number ($Re = \rho ul/\mu$), which is defined as the ratio of inertia force to viscous force. If the droplet is close to the wall, the flow will be squeezed between the wall and the droplet. This leads to an increase in shear rate, causing the droplet pinch-off to happen sooner and with a smaller diameter. In the presence of walls and for low Re, the drag force is a function of the droplet size relative to the channel [114].

Figure 2-1 shows a schematic view of two planar devices in which $w_1 > w_2$ (channel width of the first device is larger than that of the second device) and average c-phase velocities are the same. The interfacial tension forces, F_γ, are equal in both cases, but the viscous force, F_τ, in the 2nd device is higher because of the higher shear rate. Therefore, it can be hypothesized that droplets are smaller in the 2nd case. In other words:

$$\left[\begin{array}{l} F_{\gamma,1} = F_{\gamma,2} \\ \dot{\gamma}_{max,1} < \dot{\gamma}_{max,2} \rightarrow F_{\tau,1} < F_{\tau,2} \end{array}\right. \quad \Longrightarrow \quad D_{d,1} > D_{d,2} \tag{2-9}$$

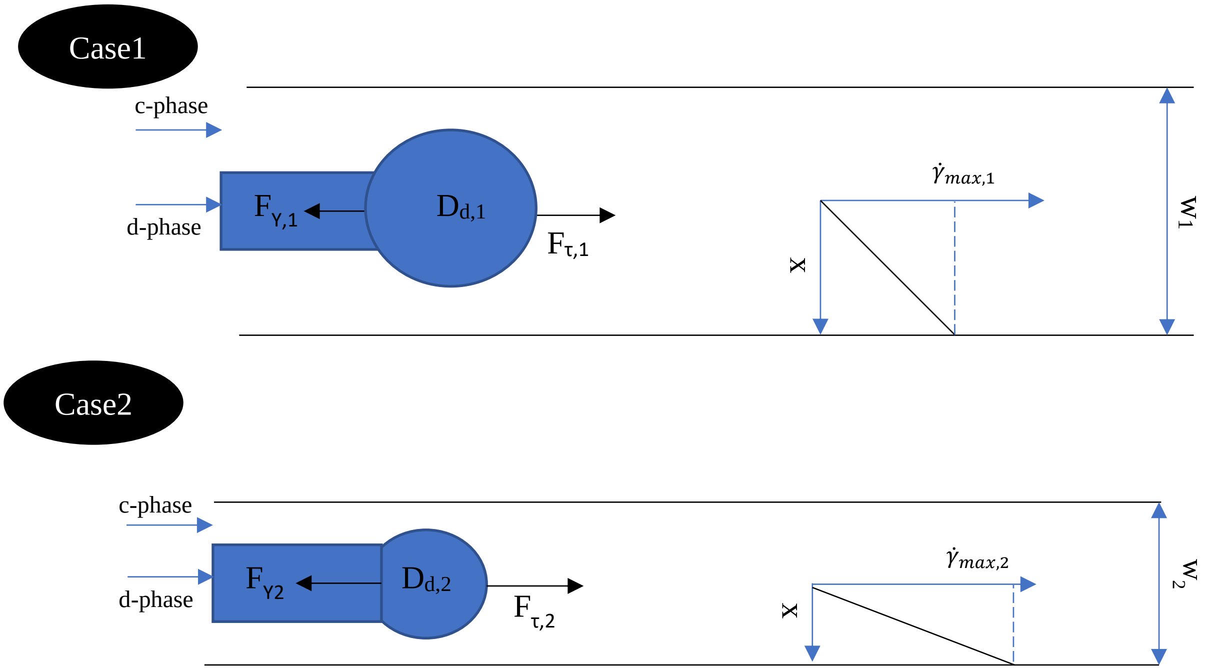

Figure 2-1. Hypothesized effect of channel width, w, on the droplet size, D_d*, through shear rate,* $\dot{\gamma}_{max}$*.* $w_1<w_2$*.*

2.3 The proposed approach in the current research

In this project, we tend to control droplet size over a wide range by a single device with controllable moving walls. There are some works have been done on the device with flexible walls, but there are more to be done, especially for the co-flow. Firstly, based on Table 1-4, the co-flow method is generally more capable of generating droplets of different sizes. Secondly, there are important scientific gaps about the wall effect on droplet size in this method. Very little was found in the literature on the question of what is the effect of channel size on the droplet size at constant c-phase velocity and flow rate. The impact of viscosity and channel heights on the range of droplets will also be addressed. Upon transition from a dripping regime to a new regime, the new regime and important forces will be studied.

There are some considerable benefits in changing channel width rather than c-phase flow rates to control droplet size. Firstly, there will be no physical and geometrical constraints to control droplet size. Secondly, some instabilities occur upon alteration of flow rates due to the flexibility of connecting tubes and PDMS channels [108]. That is why polydispersity of droplets by locally adjusting channel size is less [109]. Thirdly, syringe pumps provide unstable flow rates, especially at low flow rates [108]. Fourthly, the single emulsion device with flexible walls can be used in two-step double emulsion systems to control two-layer droplets. In double emulsions, changing the c-phase flow (middle phase in double emulsions generation) rate not only affects the core size but also influences the whole fluid dynamics of the second step of double emulsions. The better option could be using channel size to control core droplet sizes.

2.4 Experimental procedures

2.4.1 Materials

polydimethylsiloxane (PDMS) (Sylgard 184 kit, Dow Corning, USA) pre-polymer with a 10:1 ratio of base to curing agent were mixed. The mixture was then put into the degasification chamber to lose its bubbles. Then it was poured on a replication mold for the fabrication of a microchannel for the co-flow droplet generation process. The tubing between syringes and the device was achieved by flexible silicon tubing (Masterflex, Cole-Parmer Instruments CO, USA). Pulled glass capillary (OD: 1.0 mm, 1B100–4, World Precision Instruments, USA) was used as a d-phase injector. Deionized (DI) water droplets were dispersed into a c-phase flow of silicone oil (Silicone oil, Sigma-Aldrich co., Germany). Properties of materials are as follow:

Table 2-2. Properties of materials used in this project

Material	*Density (Kg/m^3)*	*Viscosity (cSt)*	*Interfacial tension (mN/m)*
Silicone oil-1	*960*	*100*	*35.18* [115]
Water	*998*	*1.004*	
Silicone oil-2	*950*	*50*	*35.26* [116]

2.4.2 Device fabrication

The standard soft lithography technique was utilized to fabricate the co-flow droplet generator. A degassed PDMS mixture (base to curing agent ratio of 10:1) was poured into the molds of top layer and bottom layer. The replication molds were designed with SolidWorks 2020 (SolidWorks Co., USA) and 3D printed using PolyJet technology (Connex 3 Objet 260, Stratasys Ltd., USA) with the resolution of 32 µm. The top and bottom PDMS layers were polymerized on a heater at 85 °C for 3 hours. The cured PDMS layers were carefully peeled off the mold. Cured top layer and bottom layers are shown in Figure 2-2. PDMS layers were bonded using an oxygen plasma bonding machine (Harrick Plasma, PDC-001, USA). Then, the PDMS device was bonded to two microscope glass slides from the top and bottom using the oxygen plasma technique. The device was inserted into a fixture shown in Figure 2-3 (a-b). The channel was squeezed by two moving blocks pushed by two micro-positioners installed on both sides of the fixture by bolts and nuts. The design process of the device will be described in Chapter 3.

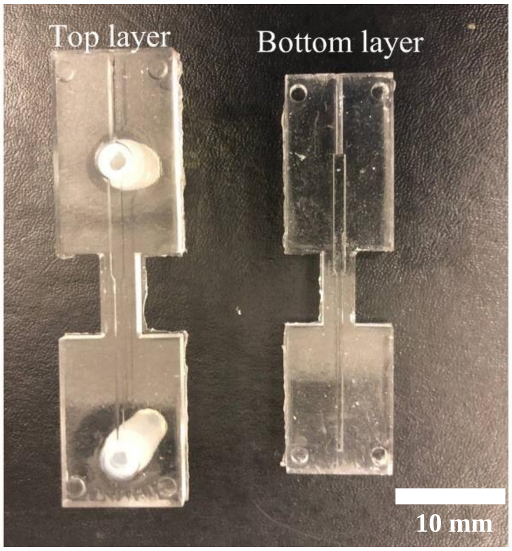

Figure 2-2. Top layer and bottom layer of the device. The layers were fabricated using the soft lithography technique.

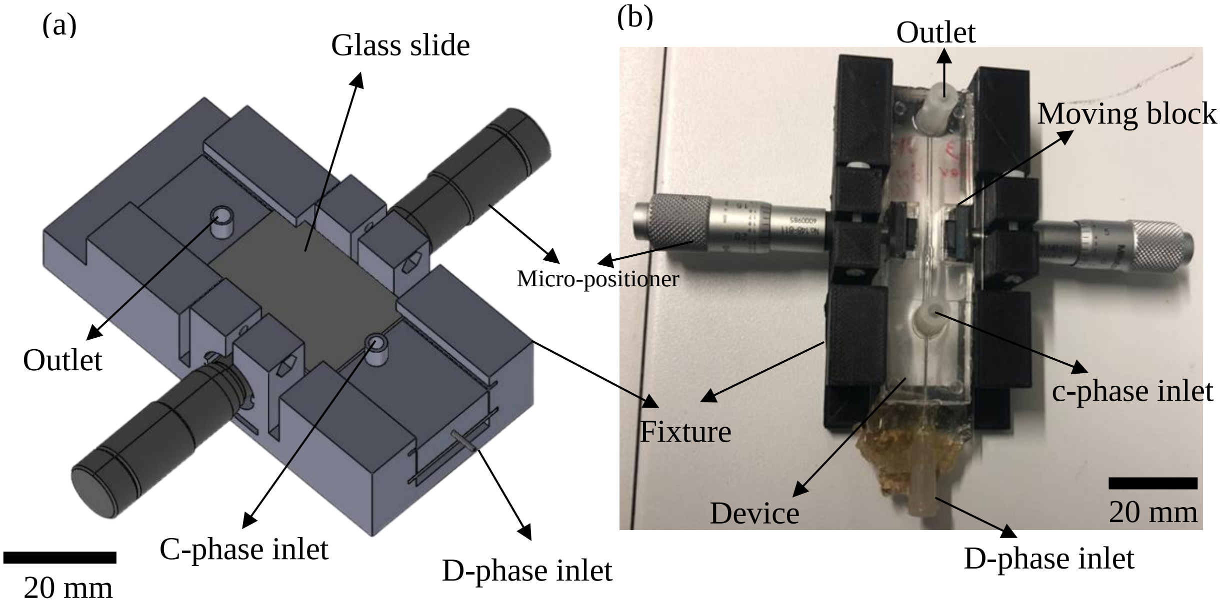

Figure 2-3. (a) CAD drawing of device and fixture, (b) Fabricated device inserted into the fixture. The system consisted of a device, two moving blocks, two micro-positioners. The micro-positioners are attached to the fixture by two bolts and nuts.

2.4.3 Experimental setup and droplet measurement

The experimental setup in Figure 2-4 consisted of the assembly of device and fixture for controlling the channel size, a high-speed camera (IL5, Fastec Imaging Corp., USA), d-phase syringe pump (210 Legacy, KD Scientific, USA), d-phase syringe pump (LEGATO 210, KD Scientific, USA), a computer, and a collecting container. Droplet diameters are measured by ImageJ. A scale was given to this software, and then diameters of droplets were measured based on the relation of the scale and the resolution of the screen.

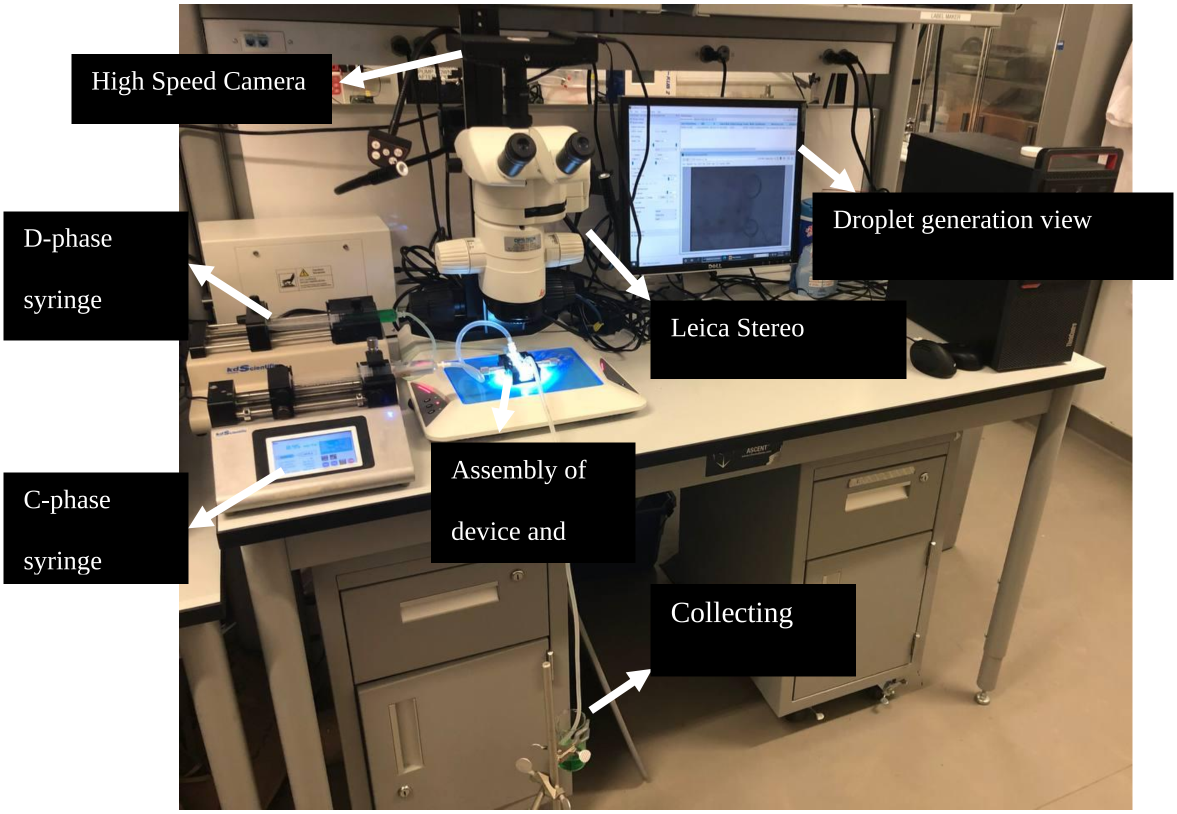

Figure 2-4. Experimental setup used for droplet generation, consisting of the assembly device and fixture, high-speed camera, microscope, computer, c-phase and d-phase syringe pumps, and collecting reservoir,

Chapter 3: DEVICE DESIGN

In this section, the design and development of the microfluidic droplet generator device are described. First, the conceptual design is introduced. Then the design was modified, as will be discussed. The design will be ultimately finalized by simulations. The modified device is then tested.

3.1 Conceptual design

Controlling the size of droplets by the c-phase flow rate (Q_c) has some limitations, as discussed earlier in Chapter 1. Parameters such as the c-phase viscosity (μ_c), interfacial tension (γ), capillary or nozzle tip diameter (D_n), and channel size (D_c) can help in controlling the droplet size. The droplet sizes can hardly be changed continuously by μ_c and γ. For instance, if the droplet diameter is supposed to increase from 100 μm by 50 μm in each step until 1 mm, the fluid(s) should be replaced 20 times. Also, capillaries in the co-flow systems are generally made of inflexible materials such as glass and 3D-printed materials. The only remaining parameter is D_c. Our design concept relied on the idea of developing a device whose channel size can be altered on-demand.

The mentioned idea was implemented using PDMS as the device material due to its low elastic modulus, allowing modification of the channel size upon compression or extension [117]–[119]. Ease of fabrication, bonding, and rapid prototyping [120], as well as optical transparency [121] and low cost [122], are among the other advantages of PDMS. One disadvantage of PDMS is, however, its high hydrophobicity which will not be problematic for aqueous d-phase fluids.

Figure 3-1 schematically shows the proposed co-flow PDMS droplet generation device with flexible walls. The design included a main body made of PDMS, a glass capillary (used as d-phase inlet), a c-phase inlet, an outlet, and two moving blocks. The channel is shown by dashed lines. The channel has two sections, a wide section and a narrow one. The capillary is placed at the beginning of the narrow section to prevent its contact with the wall. The walls of the channel can be compressed in the width direction by moving the blocks inwards towards each other. Precision in blocks movement can be provided by two micro-positioners.

In Figure 3-1, the values for some dimensions are given as follows:

- The overall width and length of the device are 20 mm and 80 mm, respectively. These values were selected so that the device fits well onto a standard glass slide that has a width of about 25 mm.
- The width of the narrow section of the channel was designed to have the size of the largest droplet (i.e., 1 mm). This width is intended to be modified by the moving blocks.
- The width of the wide section of the channel was set to 2 mm to provide a sufficient distance from the glass capillary. The capillary is fragile and should not be pressed by the walls.
- DBC was set at 4 mm to decrease the stress concentration (see Appendix A)
- WC was selected to be the lowest possible value practically (2 mm) because the channel width decreases more for a displacement of the blocks.
- The value of WB will be finalized in the following section. For now, the channel height (h) is 1 mm, although it is one of the parameters under investigation for its effect on the droplet size in the next chapter.

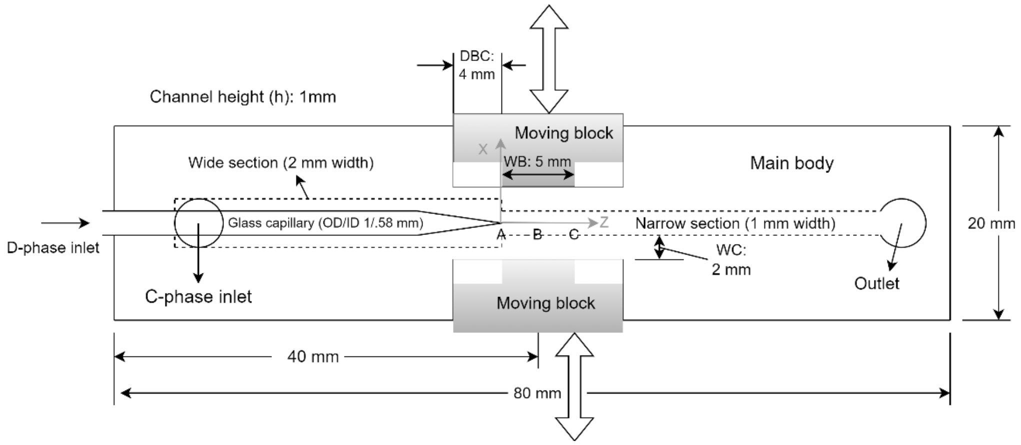

Figure 3-1. Schematic of the proposed droplet generation device with flexible walls, showing its conceptual design that consists of a main PDMS body with straight channels (dashed lines) for c-phase flow, a glass capillary for d-phase flow, and two moving blocks for channel width modulation.

Figure 3-2 shows the steps for assembling the device into a fixture for the precise displacement of the compression blocks to modify the channel width. The device is fabricated as described in Section 2.4.2 (Figure 3-2 (a)). Then, it is bonded to two glass slides from the top and bottom using an oxygen plasma bonding machine (Harrick Plasma, PDC-001, USA), as shown in Figure 3-2 (b). In this way, the top and bottom surfaces of the device become rigid, and consequently, the channel cross-section remains symmetrical after deformation. The moving blocks are also placed in the designated locations around the channel in this step. It must be noted that the PDMS-glass interfaces between the moving blocks were not bonded to the glass, so the channel size could be changed in the width direction. Then, the device and glass slides are inserted into the grooves of a 3D printed fixture, as depicted in Figure 3-2 (c). The channel walls are squeezed by two micro-positioners attached to the fixture by two bolts and nuts.

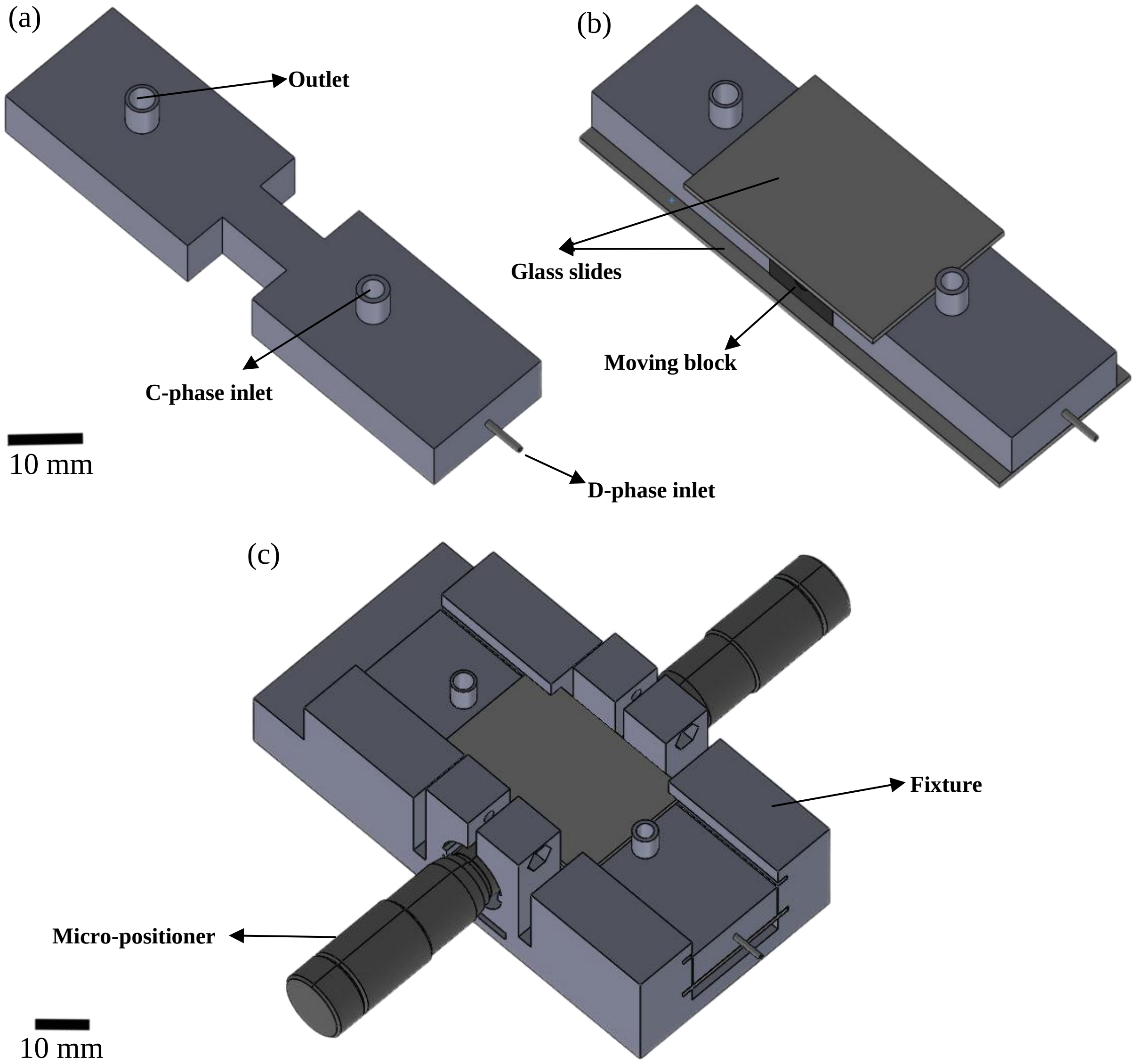

Figure 3-2. Assembly of the droplet generation device into a 3D printed fixture: (a) The co-flow droplet generation device with flexible walls, (b) The device bonded with glass slides from top and bottom using an oxygen plasma bonding machine and two moving blocks.

3.2 Finalization of the design concept

In this section, the device design is modified by modeling and simulation. Firstly, the wall surface between points A and C (see Figure 3-1) should remain flat after deformation to facilitate droplet generation analysis; otherwise, one needs to consider the effects of flow acceleration along the narrow section. For having a flat wall, the standard deviation ($\sigma_{displacement}$) or the amount of variation of wall displacement in the x-direction (blocks movement direction towards to the channel) from point A to C (ΔX_{mean}) should be sufficiently low:

$$\sigma_{displacement} = \sqrt{\frac{\sum(\Delta X_i - \Delta X_{mean})^2}{N}} \tag{3-1}$$

where ΔX_i, ΔX_{mean}, and N show the wall displacement of point i, the mean wall displacement from A to C, and the number of computational points between A and C, respectively. Secondly, the displacement around the tip of the capillary (ΔX_A) must not deviate considerably from the displacement at the middle of the deformation zone (ΔX_B). For this criterion, the defined parameter D should also be low:

$$D = \frac{\Delta X_B - \Delta X_A}{\Delta X_B} \times 100\% \tag{3-2}$$

ANSYS nonlinear finite element analysis (FEA) software was employed to analyze the deformation of the channel (see Appendix B for the boundary conditions and grid independence). Figure 3-3 illustrates the channel profile in the current design when the blocks move for 0.4 mm in the x-direction. The wall surface is not flat after deformation. The values of $\sigma_{displacement}$, and D are 0.031 mm, and 21%, respectively. These values further increase when the blocks are pushed further due to the more stretch of the channel.

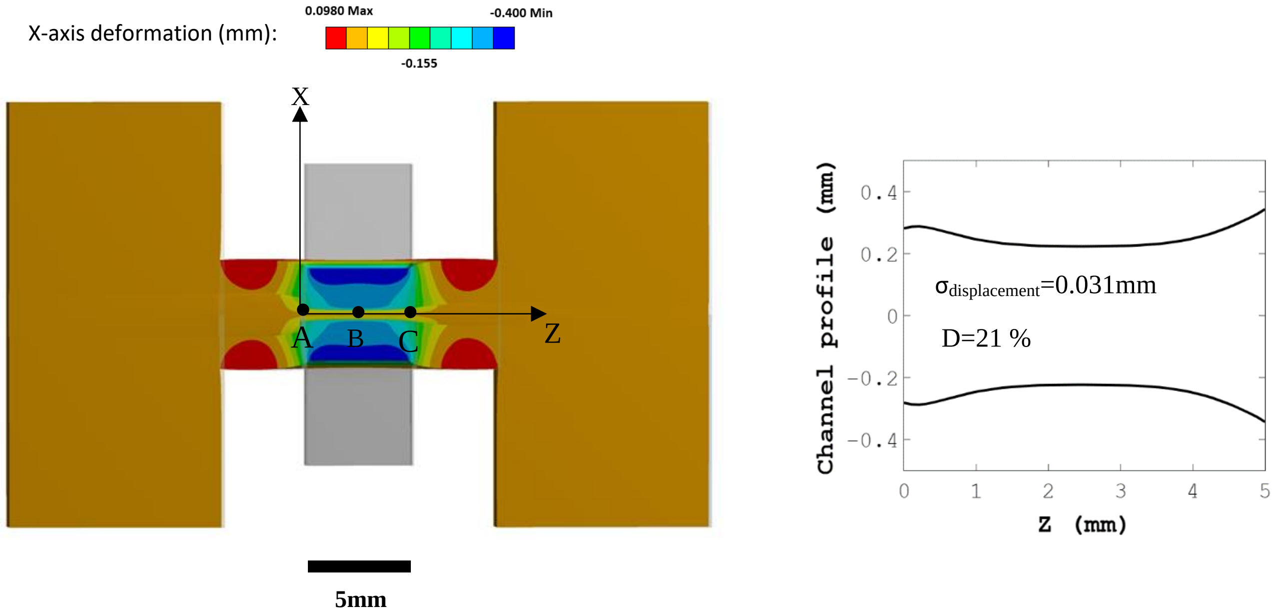

Figure 3-3. Deformation contour in the x-direction (left) and its corresponding deformed channel wall profile (right); The displacement of blocks is 0.4 mm. The values of $\sigma_{displacement}$ and D are high for the conceptual design. Some modifications are needed to have a flat wall after deformation.

The values of $\sigma_{displacement}$, and D were decreased in a 3-step modification as presented in Figure 3-4 and explained below:

- Modification 1: Curving the surfaces of the blocks (Figure 3-4 (a)): As seen in the channel profile of Figure 3-3, the wall had a convex shape after deformation due to the flat surface of moving blocks. The channel profile in Figure 3-4 (a) suggests that the strategy of curving the surfaces of the blocks decreased the $\sigma_{displacement}$ from 0.031 to 0.022 mm.

- Modification 2: Extending the width of the blocks (Figure 3-4 b): Channel profile in Figure 3-4 (a) shows that the wall surface was flat except for the beginning and the end part. A proper solution for this problem was to extend the width of moving blocks 1 mm from each side. The value of $\sigma_{displacement}$ shows a significant decline from 0.022 mm to 0.008 mm in the second modification.
- Modification 3: Gradually decreasing channel width from wide section to narrow section (Figure 3-4 c): Based on the channel profile in Figure 3-4 (b), the wall surface was flat everywhere except for the 0.5 mm of the beginning part. The value of D was about 24% which shows the significant difference between channel widths at points A and B (as depicted in. 3-3). This problem can be assigned to the sudden decrease of channel width at point A. By gradually decreasing channel width from wide section to narrow section, D decreased from 24% to 5%. As the channel profile shows in Figure 3-4 (c), the whole wall surface became flat.

Therefore, the configuration of modification 3 was selected as $\sigma_{displacement}$, and D decreased to their minimum value of 0.003 mm, and 5%, respectively (Table 3-1).

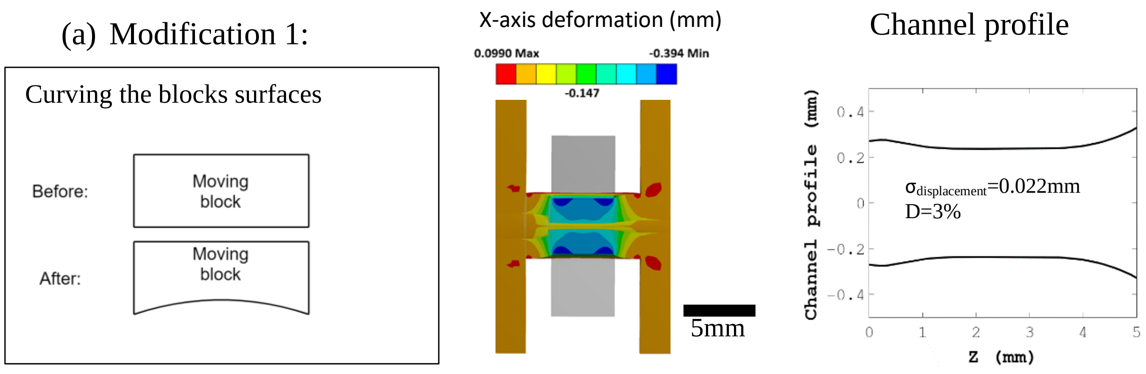
(a) Modification 1:

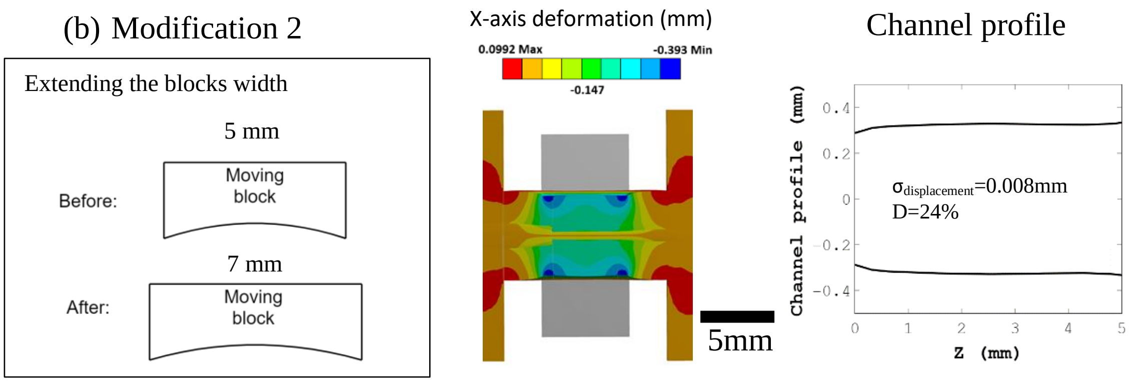
(b) Modification 2

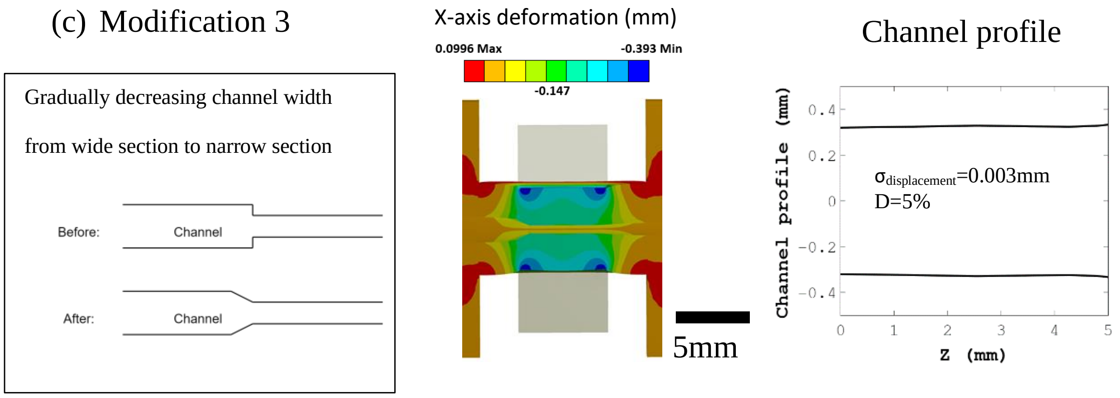
(c) Modification 3

Figure 3-4. Three-step modifications (left) and their corresponding channel deformation profiles (middle and right). In step 1, the surface of moving blocks which are in contact with the device were curved. In step 2, the width of the blocks was extended. In step 3, the channel width was gradually decreased from the wide section to the narrow section. The displacement of blocks is 0.4 mm with the coordinates being the same as Figure 3-3.

Table 3-1. The $\sigma_{displacement}$ and D values in the steps of modifications when blocks move for 0.4 mm. In step 3, $\sigma_{displacement}$ and, D reached to their minimum values.

Step	Modification	$\sigma_{displacement}$ [mm]	D
0	Original case	0.031	21%
1	Curving the blocks surface	0.022	13%
2	Extending blocks surface from 5 to 7 mm	0.008	24%
3	Adding extra parts to have a gradual decrease in channel width from wide section to narrow section	0.003	5%

In the final part of the design finalization, the channel profile was computationally tested for different displacements of the blocks. Figure 3-5 shows the channel profile for different displacements of blocks from 0.4 to 0.6 mm. The value of $\sigma_{displacement}$ increased by increasing blocks displacement as the wall stretches more at the end of the deformation zone (point C). The lack of a flat surface at point C was inevitable as the channel width should merge to its original size (i.e., 1mm) from this point. However, disregarding the ending part, the wall surface was still flat, and the value of D was low.

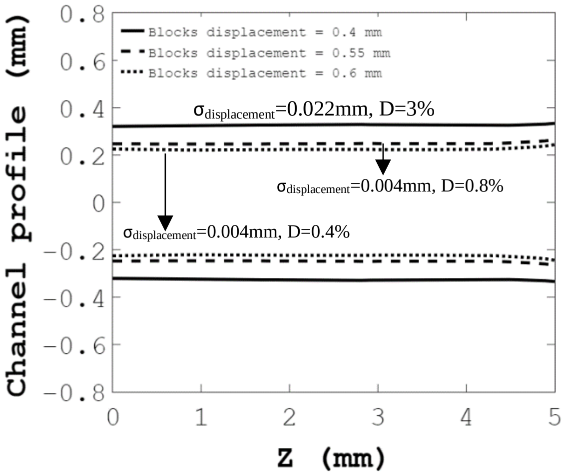

Figure 3-5. Channel profile for different displacements of blocks. At different blocks displacements, the values of $\sigma_{displacement}$ *and D were low and acceptable.*

3.3 Final Device Fabrication and Proof of Concept Testing

In this section, the device was fabricated based on the final modifications and experimentally tested for co-flow droplet generation. Figure 3-6 shows the assembly of the device and the fixture. The assembly consisted of the microfluidic device, the fixture, two moving blocks, and two micro-positioners. By altering the channel width to the desired value, the distance of the capillary tip from the side walls was measured to make sure that it was in the middle of the channel.

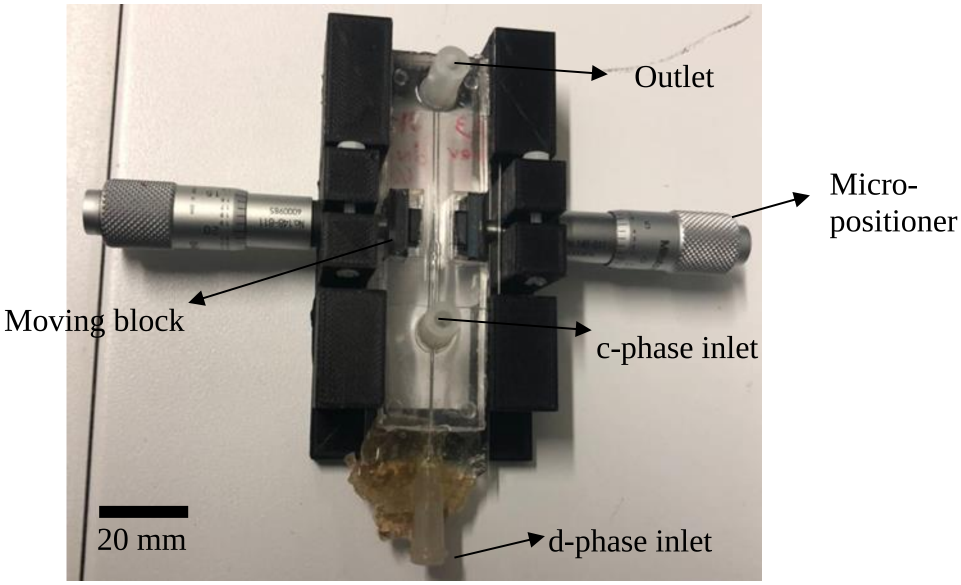

Figure 3-6. The Assembly of device and fixture consisting of the device, two moving blocks, and two micro-positioners. The channel is squeezed by the blocks which are pushed by the micro-positioners.

Widths of the channel decreased from 1 to 0.3 mm by the moving blocks to measure $\sigma_{\text{displacement}}$, and D. Figure 3-7 shows $\sigma_{\text{displacement}}$ and D versus channel width. Generally, a decline in channel width enhanced $\sigma_{\text{displacement}}$ and D. When the wall was subjected to large deformation, it tended to have a convex surface. However, until w = 0.3 mm, $\sigma_{\text{displacement}}$ was below 0.05 mm, and the wall surface still can be considered flat.

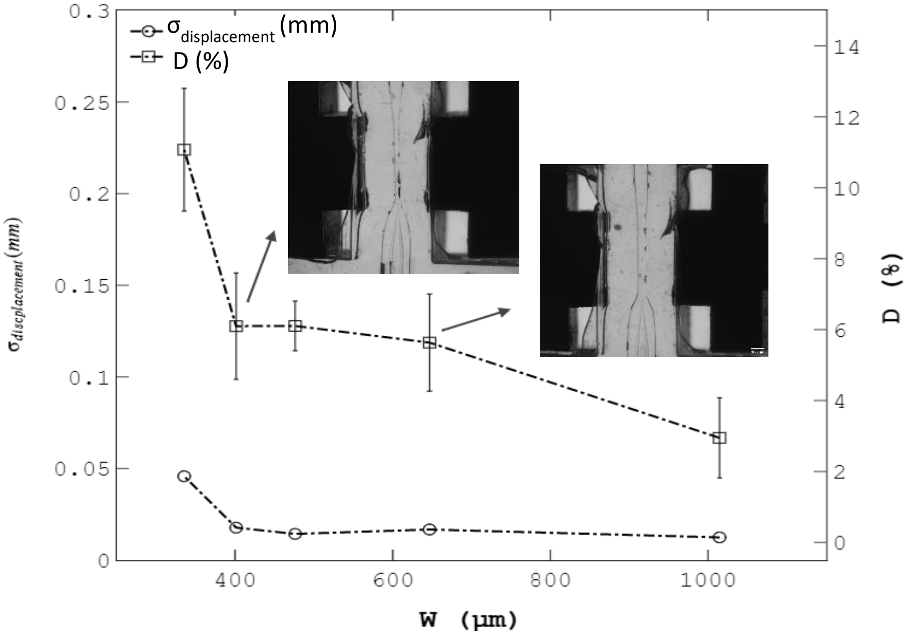

Figure 3-7. The variation of wall displacement, $\sigma_{displacement}$ and, D versus the channel width, w, was tested experimentally for the optimized device. The parameter $\sigma_{displacement}$ is approximately constant from w = 1000 to 480 µm, and increases sharply at low w. The parameter D gradually increases from w = 1000 to 400 µm and then increases sharply at w = 300 µm because the wall is highly stretched.

Figure 3-8 shows the droplets generated for three different widths at $Ca_c = 0.024$, $We_d = 0.0052$, and $u_c = 8.55$ mm/s. The decrease of droplet size with w shows the efficient operation of the device. The reason for this trend will be discussed in the next chapter.

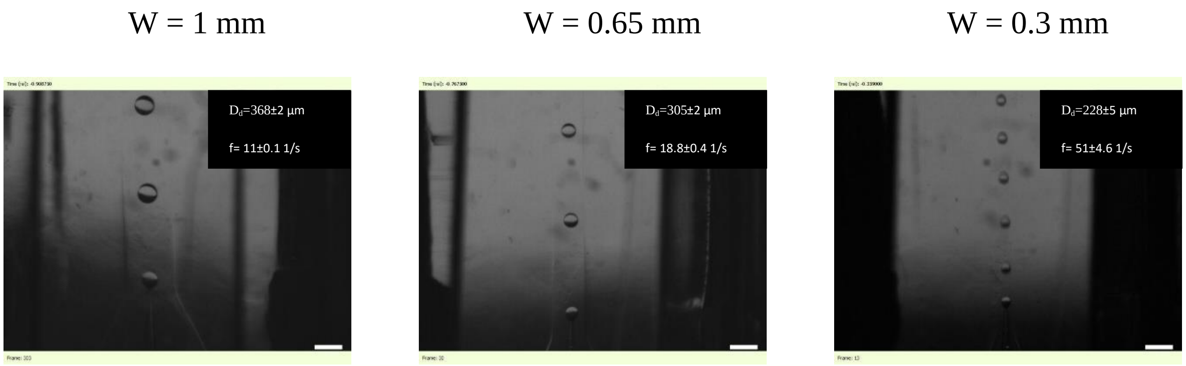

Figure 3-8. Droplets generated in the proposed device at the different channel widths (w) and at at $Ca_c = 0.024$, $We_d = 0.0052$, and $u_c = 8.55$ mm/s. The. Scale bar=500μm.

Chapter 4: RESULTS AND DISCUSSION

This chapter presents the results of droplet generation by the flexible-wall microfluidic device through the following sections:

- 4.1. Studied parameters and their levels: First, studied parameters and their various levels are introduced. The parameters included in this study are channel width (w), channel height (h), c-phase velocity (uc), c-phase flow rate (Qc), d-phase flow rate (Qd), and c-phase viscosity (μc). The channel width by which the droplet size was controlled was changed in 3 levels (w = 0.3, 0.65, and 1 mm)
- 4.2. Droplet generation regimes: Upon altering other parameters, various droplet generation regimes may be observed. Dripping, plug, and transition region from dripping to the wide jetting regime were observed in this study.
- 4.3. Droplet generation with modulating the channel width: The images of droplets at different channel widths (w) and Capillary number (Ca_c) will be shown. In a constant Ca_c, the channel width had a strong effect on droplet size through the wall effect.
- 4.4 Effect of channel width on droplet size at constant c-phase velocities for different viscosities: When channel width decreased from 1 mm to 0.3 mm at constant c-phase velocity, there was a steady decrease in droplet size. Two analytical equations were developed to predict the ratio of droplet size upon altering the channel width.
- 4.5. Effect of channel width on droplet size at constant velocities; for different channel heights: For a lower channel height, the percentage of droplet size change was higher due to the more profound wall effects.

- 4.6. Effect of channel width on droplet size at constant c-phase flow rates; for different viscosities and channel heights: Compared to the constant c-phase velocity, the decrease in droplet size at constant flow rate was more when the channel width decreased from 1 to 0.3 mm. This trend can be due to the rise of the wall effect in addition to the increment in the c-phase velocity, giving rise to the increased viscous force on the droplet size.
- 4.7. Effect of channel width on droplet size for different d-phase flow rates: The effect of d-phase flow rate on droplet size was weak for the dripping regime. D-phase flow rate affected droplet size when $We_d \sim O(0.1)$, and the regime showed a transition to the wide jetting regime.
- 4.8. Generating droplets for a wide range of sizes: In this section, the ability of the developed device is compared with the previous works in terms of the range of droplet sizes. Our device generated droplets ranging from 913 to 175 μm.
- 4.9. Droplet size prediction model: A model was developed based on Buckingham's Π theorem to predict the droplet size. The model is a function of Ca_c, h/w, and Re_c which show the effect of interfacial tension force, wall effect, and flow conditions on droplet size.

4.1 Studied parameters and their levels

In this study, the effect of channel width on droplet size was explored under different conditions. Table 4-1 shows the levels of considered parameters, including channel width (w), channel height (h), c-phase velocity (u_c), c-phase flow rate (Q_c), d-phase flow rate (Q_d), and c-phase viscosity (μ_c). The levels of some parameters were physically bound to the device geometry. As discussed in the previous chapter, the minimum possible level for w was 0.3 mm. Also, due to poor squeezing behavior in shorter channel heights, the minimum level of h was selected to be 0.7 mm. C-phase viscosity levels were also selected sufficiently high to set lower values for the c-phase velocity to reduce the research cost. To achieve higher monodispersity, droplets must be generated in the dripping regime. Therefore, values of Q_c, u_c, and Q_d were calculated to ensure droplet generation in the mentioned regime.

Table 4-1. Parameters and their levels studied in the current experiment

Parameter	Number of levels	Levels
w [mm]	3	1, 0.65, 0.3
h [mm]	2	1, 0.7
u_c [mm/s]	25	From 1.25 to 17.10[c]
Q_c [ml/hr]	29	From 2.01 to 57.27
Q_d [ml/hr]	4	1, 2, 3, and 4
μ_c [cSt]	2	50, and 100

Figure 4-1 compares Ca_c and We_d of cases of the current research with the literature [46], [82], [84], [85], [87]. The ranges of Ca_c ($0.002 < Ca_c < 0.1$), and We_d ($0.0052 < We_d < 0.1$) were selected for three important reasons. Due to instabilities at lower channel width, Ca_c should be more than 0.002. On the other hand, Ca_c and We_d were capped at 0.1 to prevent the transition to jetting regimes and consequent polydispersity. Moreover, the minimum value for We_d was

---

[c] Due to the high number of levels for u_c and Q_c, their levels are not written in Table 4-1. See Appendix C for the list of case studies in this project

selected to be 0.0052 because numerous studies [79], [82], [84] have revealed the weak effect of We_d on the droplet size at the low values of We_d.

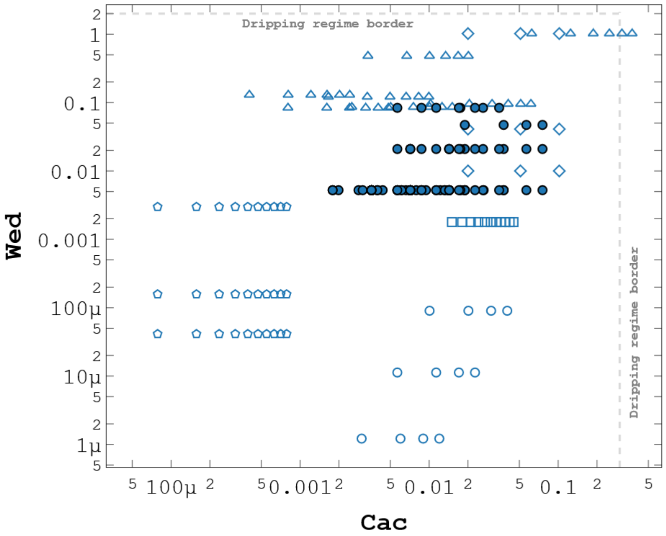

Figure 4-1. Comparing the scatter plot of d-phase Weber number, We_d, versus c-phase Capillary number, Ca_c, of the current study (●) vs. the values in the previous works of Shams et al. (◊) [84], *Chu et al. (□)* [46], *Vijayan et al. (⬠)* [87], *Erb et al. (Δ)* [85], *Deng et al. (○)* [82]

4.2 Observed droplet generation regimes

As stated in Chapter 1, there are various regimes in the co-flow droplet generation. Three distinct regimes were observed in this study, the dripping regime (Figure 4-2 (a)), the plug regime (Figure 4-2 (b)), and the transition from dripping regime to the wide jetting regime ((Figure 4-2 (c)). In the plug regime, the thread grew enough to touch the lateral walls while the channel width was at its minimum level. This was the main difference between the dripping and the plug regime. As the d-phase flow rate increased such that $We_d \sim O(0.1)$ [8], the wide jetting regime emerged (Figure 4-2 (c)). In this regime, the inertia force becomes dominant, i.e., a jet is formed, and a droplet is generated at a distance from the capillary tip. In Section 4.7, it will be shown that the polydispersity increased in this regime.

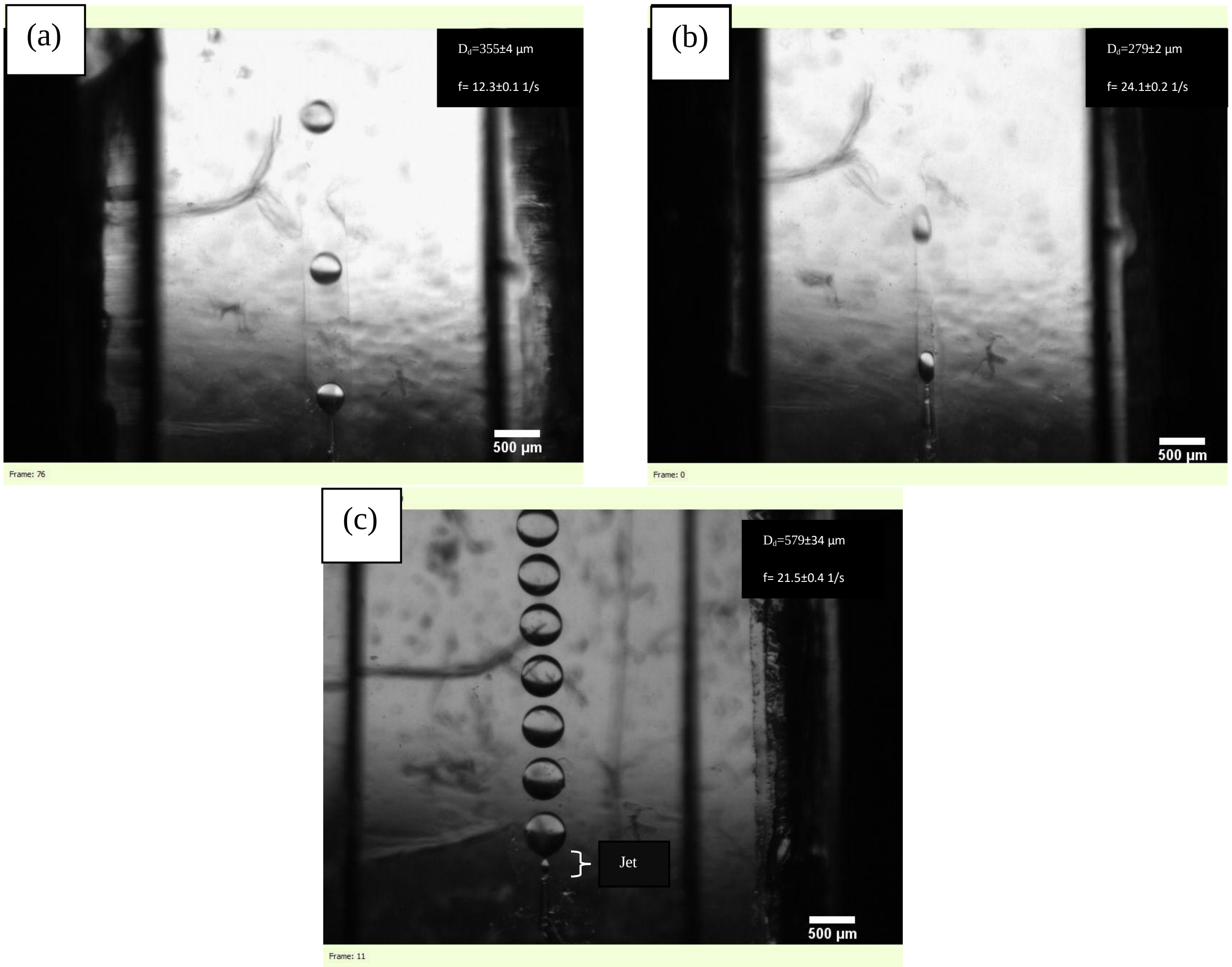

Figure 4-2. Various droplet generation regimes in the proposed device with (a) dripping regime at w=0.65mm and (b) plug regime at w=0.3mm. Cases of (a) and (b) both were under similar conditions in terms of μ_c *= 50 cSt,* u_c *= 5 mm/s, h = 0.7 mm,* Q_d *= 1 ml/hr,* Ca_c *= 0.007, and* We_d *= 0.0052.(c) Transition region from dripping to wide jetting regime. The conditions were: w = 1 mm, μc = 100 cSt, uc = 4 mm/s, Qc = 10 ml/hr, h = 0.7 mm, Qd = 4 ml/hr, Cac = 0.011, Wed = 0.084.*

Polydispersity is defined as the ratio of the standard deviation of droplet diameter to the mean diameter of the droplet population. Figure 4-3 shows the box plot of polydispersity for the regimes observed in this study. In the dripping regime, the perturbations from the system occur at a fixed location. Because of this, the median of polydispersity in the dripping regime was less than 1%. However, some outliers may be due to the experimental error. The monodispersity of droplets in the dripping regime is consistent with the literature [84], [102]. There was a slight increase in the polydispersity of droplets in the plug regime. This increase may result from the instabilities that originated from the walls. Droplets generated in the transition region to the wide jetting regime were less uniform. The existence of a jet alongside random noises led to a higher polydispersity. Polydispersity is likely to increase with a further increase of We_d because the system will operate solely in the wide jetting regime.

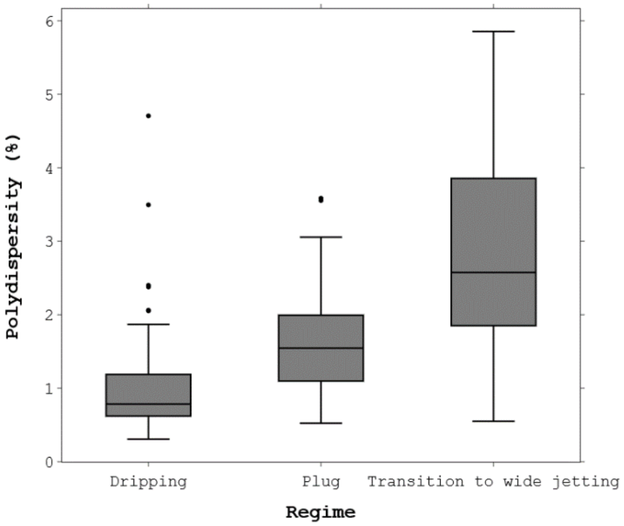

Figure 4-3. Box plot of polydispersity for the regimes observed in the current study. The median of polydispersity in the dripping and plug regimes is less than 2%. Transition to the wide jetting regime leads to the increase of polydispersity.

4.3 Droplet generation with modulating the channel width

The wall effect is not negligible when droplet sizes are comparable to the channel width; thus, different results can be observed even at constant Ca_c numbers. Figure 4-4 shows the droplets generated for different Ca_c and w values. It shows that the droplet size is not only controlled by Ca_c, but it is also significantly affected by channel width. By increasing Ca_c, smaller droplets were generated at higher throughput (rates) due to the dominance of shear forces. On the other hand, at constant Ca_c, the swelling droplet tended to break up at earlier stages in narrower channels due to impulsive effects of the wall. Therefore, as the channel width was increased, the wall effects diminished, and the growing droplet interface was more stable, yielding to larger droplets at lower rates. As a result of dominant wall effects, the “plug regime” appeared at w=0.3 mm, in which the plug was chafing the wall.

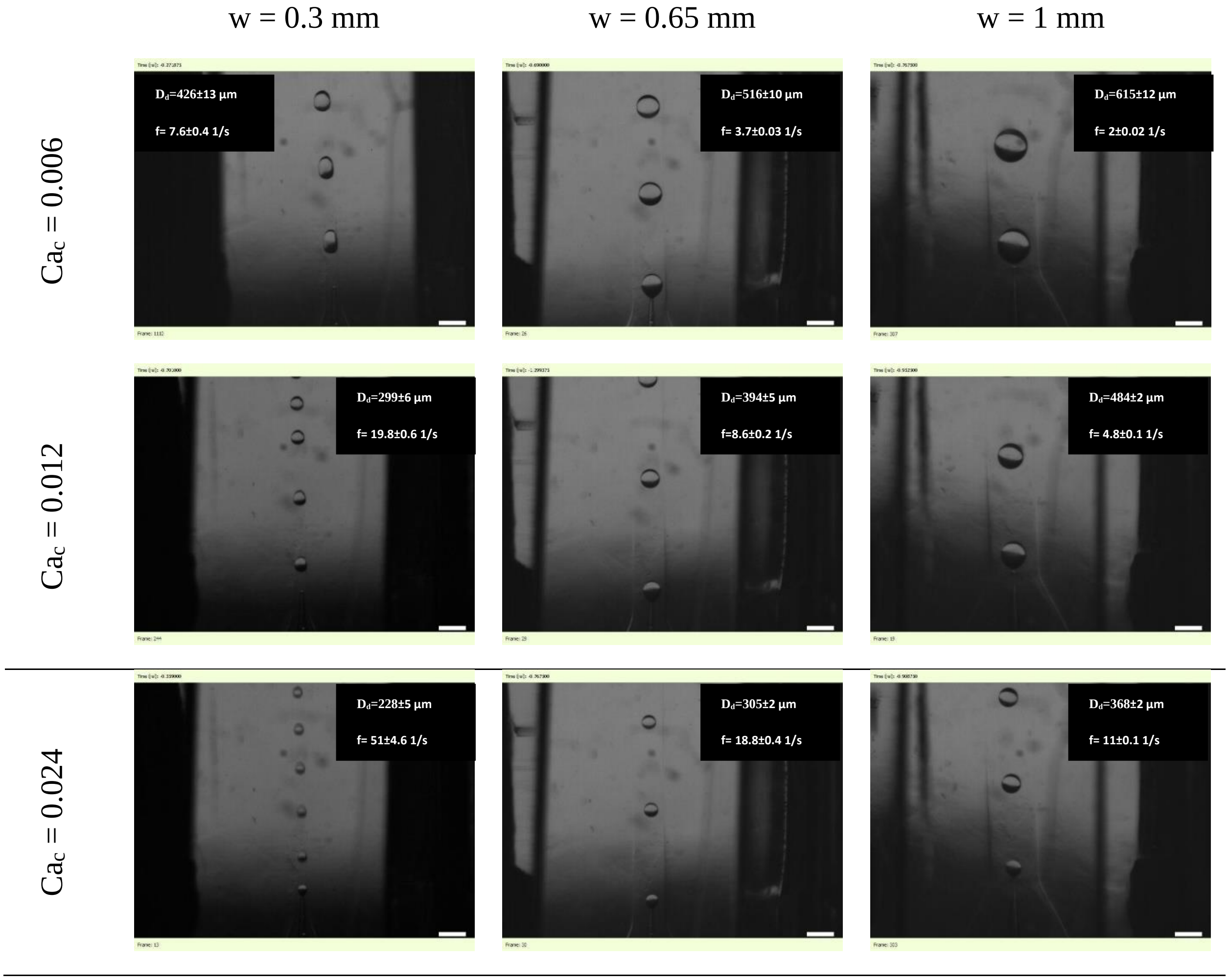

Figure 4-4. Experimental images of droplets at different Capillary numbers, Cac, and channel widths, w. At a constant Ca_c*, decreasing w led to the generation of smaller droplets due to the increase of wall effect. Scale bar=500µm*

4.4 Effect of channel width on droplet size at constant c-phase velocities; for different viscosities

The channel width was declined under two different conditions in this study: constant c-phase velocity and constant c-phase flow rate. In the former condition, we sought to better understand the wall effect on the droplet size while keeping the c-phase velocity constant (Sections 4.4 and

4.5). In the latter condition, the purpose was to increase the wall effect together with the c-phase velocity to maximize the change in droplet size when channel width was decreased (Sections 4.6, 4.7, and 4.8).

In this section, the effect of channel width on the droplet size at constant c-phase velocities and for different viscosities is studied. When the channel width was decreased from w_1 to w_2, the c-phase flow rate was decreased from Q_{c1} to Q_{c2} to keep the c-phase velocity constant ($u_{c1} = u_{c2}$). The flow rate ratio is equal to the channel area ratio:

$$u_{c1} = u_{c2} \rightarrow {}^{Q_{c2}}\!/_{Q_{c1}} = {}^{A_{c2}}\!/_{A_{c1}} \qquad (4\text{-}1)$$

where A_{c1}, and A_{c2} are the channel area at w_1, and w_2, respectively.

Figure 4-5 shows the effect of channel width on droplet size at constant velocities for two different c-phase viscosities (μc = 50 and 100 cSt). Droplet size was decreased from 42% (for μ_c = 50 cSt and u_c = 5 mm/s) to 34% (for μ_c = 100 cSt and u_c = 5 mm/s) when channel width was decremented from 1 to 0.3 mm. The decrease in droplet size for each case was considerable due to the effect of channel size on the force balance.

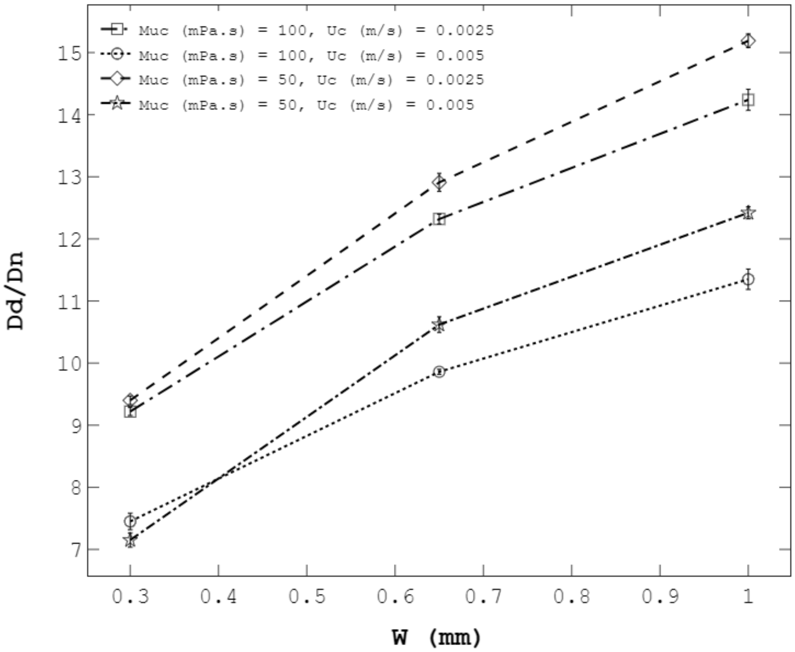

Figure 4-5. Effect of channel width, w, on droplet size, D_d, at constant c-phase velocities U_c; for different viscosities, Muc, and for h = 1 mm (for h = 0.7 mm see Appendix E). Droplet size was directly affected by the channel width and inversely affected by the c-phase velocity and c-phase viscosity.

To find a relationship between droplet size and channel width, the force balance is written. The pressure force is neglected against the viscous force in the plug regime because the plug does not block the whole channel (see Appendix D). Therefore, important forces in the plug regime are similar to that in the dripping regime, which are interfacial tension (F_γ) and viscous forces (F_τ). Therefore, Eq. 4-2 is applicable to both regimes [103]:

$$F_\tau = F_\gamma \rightarrow \mu_c \dot{\gamma} A_s \sim \gamma D_n \tag{4-2}$$

where A_s is the surface area of the droplet that is proportional to D_d^2. Here, for the plug regime, it is assumed the A_s is also proportional to D_d^2 where D_d is the droplet diameter when the plug shape changes to the droplet. This assumption greatly simplified the problem. To calculate the shear rate ($\dot{\gamma}$), the shear rate on x plane ($\dot{\gamma}_{xz} = \partial u_z/\partial x$, Figure 4-6) and on y plane ($\dot{\gamma}_{yz} = \partial u_z/\partial y$) should be considered (the coordinates are shown in Figure 4-6.). However, this section is devoted to explaining the decline in the droplet size by decreasing the channel width at constant c-phase velocity (u_c), c-phase viscosity (μ_c), and channel height (h). Therefore, just the dominating shear force was considered on the perpendicular plane to the squeezing direction or x-direction ($\dot{\gamma}_{xz}$). Two methods can be used to estimate $\dot{\gamma}_{xz}$:

- Method 1: $\dot{\gamma}_{xz}$ was approximated as $\dot{\gamma}_{xz} = u_{c-mean}/w$. The ratio of droplet diameter in w_2 (D_{d2}) to droplet diameter in w_1 (D_{d1}) can be calculated by substituting this equation in Eq. 4-2:

$$\frac{D_{d2}}{D_{d1}} = \sqrt{\frac{w_2}{w_1}} \tag{4-3}$$

- Method 2: $\dot{\gamma}_{xz}$ can be analytically calculated using the equation for axial velocity in a rectangular channel [123]:

$$u_z(x,y) = \frac{4h^2\Delta p}{\pi^3\mu_c L}\sum_{n,odd}^{\infty}\frac{1}{n^3}\left[1-\frac{\cosh\,(n\pi\frac{x}{h})}{\cosh\,(n\pi\frac{w}{h})}\right]\sin\,(n\pi\frac{y}{h}) \tag{4-4}$$

where Δp and L are pressure drop and length, respectively. The profile of $\dot{\gamma}_{xz}$ was calculated by taking derivatives of Eq. 4-4 in the x-direction. Maximum $\dot{\gamma}_{xz}$ ($\dot{\gamma}_{max}$) which occurs on the wall was selected to substitute in Eq. 4-2 because the droplet sizes in the dripping regime were in the order of channel size rather than capillary tip diameter. Therefore:

$$r = \frac{D_{d2}}{D_{d1}} = \sqrt{\frac{\dot{\gamma}_{max1}}{\dot{\gamma}_{max2}}} \tag{4-5}$$

The errors of both methods are given in Table 4-2. Here, the error is defined as: $\left|r_{pred.} - r_{exp.}\right| / r_{pred.}$. In most cases, the error of width ratio of 0.3mm/0.65mm is more than the error of 0.65mm/1mm. This is because, in the plug regime, A_s was considered to be proportional to the D_d^2, while a plug regime has a cube shape. The mean error of method 1 and method 2 are 5% and 4%, respectively. While method 2 is more detailed, the error of both methods is close to each other and satisfactory. Therefore, the first method was employed due to its simplicity. Based on this method, a decline in channel width increases the shear rate. This enhances the shear force exerted on the droplet. As a result, the shear force sooner overcomes interfacial tension force leading to smaller droplets.

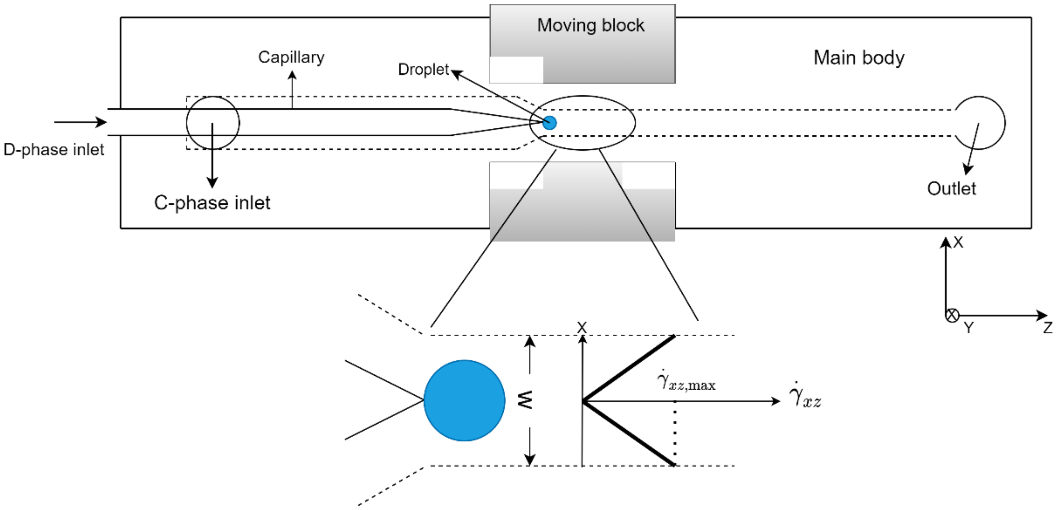

Figure 4-6. A schematic showing the dominant shear rate, $\dot{\gamma}_{xz}$, in the channel. The value of $\dot{\gamma}_{xz}$ is zero in the centerline (x = 0) and reaches to its maximum value at the wall (x = ±w/2).

Table 4-2. Comparison of the error of method 1 (Eq. 4-3) and method 2 (Eq. 4-5). The mean error of method 1 and method 2 are 5% and 4%, respectively.

#	μ_c [cSt]	u_c [m/s]	h [mm]	$w_{initial}/w_{final}$	Method 1 (Eq. 4-3) error [%]	Method 2 (Eq. 4-5) error [%]
1	100	0.005	1	0.65mm/0.3mm	11.2	1.9
				1mm/0.65mm	7.3	0.6
2	100	0.0025	1	0.65mm/0.3mm	10.2	0.9
				1mm/0.65mm	7.3	1.0
3	50	0.005	1	0.65mm/0.3mm	0.9	9.2
				1mm/0.65mm	6.1	2.1
4	50	0.0025	1	0.65mm/0.3mm	7.1	1.9
				1mm/0.65mm	5.44	2.7
5	100	0.005	0.7	0.65mm/0.3mm	3.8	6.8
				1mm/0.65mm	1.8	5.7
6	100	0.0025	0.7	0.65mm/0.3mm	11.5	0.2
				1mm/0.65mm	1.2	5.2
7	50	0.005	0.7	0.65mm/0.3mm	2.5	12.4
				1mm/0.65mm	0.2	3.9
8	50	0.0025	0.7	0.65mm/0.3mm	5.1	5.5
				1mm/0.65mm	0.2	4.2

4.5 Effect of channel width on droplet size at constant velocities; for different channel heights

The effect of channel width was explored on the droplet size at constant velocities for different channel heights as depicted in Figure 4-7 for h = 0.7 and 1 mm. For h =1 mm, a decrement in w from 1 to 0.3 mm altered the droplet size by 34-35% (depending on the velocity), and for h = 0.7

mm, that was about 40% to 44%. For the lower channel heights, the changes in the droplet size got more pronounced. In the shorter channel heights, the wall got closer to the droplet not only horizontally but also vertically; c-phase bypassing the droplet hardly enhanced the wall effect. As a result, the total viscous force exerted on the droplet increased, and the changes in droplet size were more at h = 0.7 mm.

The ratio of droplet sizes for a change in channel height can be calculated. When the channel height changes from h_1 to h_2 at constant u_c and w, the droplet size ratio (D_{d2} / D_{d1}) can be calculated similarly to Eq. 4-3:

$$rh = \frac{D_{d2}}{D_{d1}} = \sqrt{\frac{h_2}{h_1}} \tag{4-6}$$

Table 4-3 shows the error of Eq. 4-6 for different conditions. Here, the error was defined as: $\left|rh_{pred.} - rh_{exp.}\right|/rh_{pred.}$. The maximum error was about 14.4% in Case 4, while the average error is only 4.3%. This shows the mechanism by which h affects the droplet size the same holds for w. A decline in both parameters increased the shear rate which led to the generation of smaller droplets.

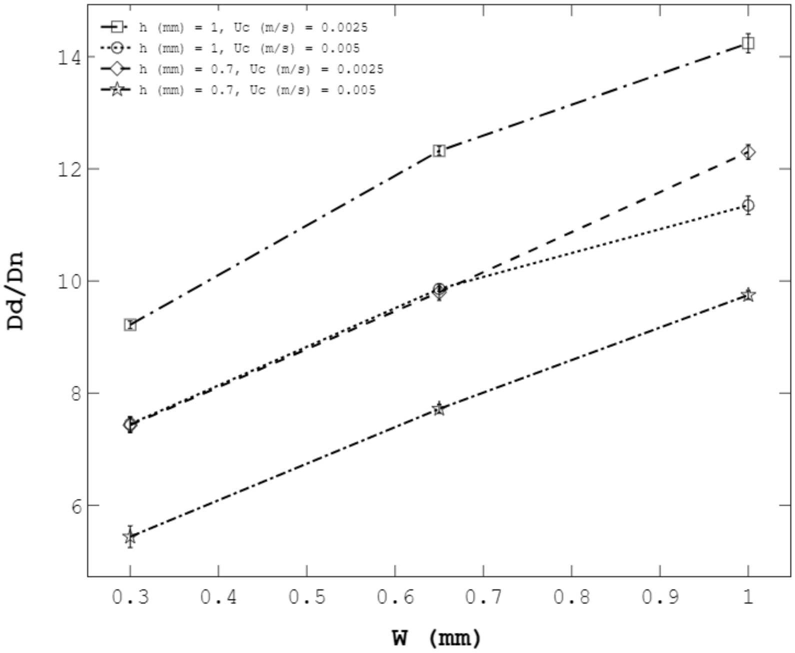

Figure 4-7. Effect of channel width, w, on the droplet size, D_d, at constant c-phase velocities, U_c, and for different channel heights,h, and μc = 100 cSt (for μc=50 cSt, see Appendix F). The height and width of the channel directly affected the droplet size through the wall effect.

Table 4-3. Error of Eq. 4-6. under different conditions. The maximum and average error were 14.4% amd 4.3%, respectively.

Case	**μ (cSt)**	**u_c (m/s)**	w (mm)	**$h_{initial}$/ h_{final}**	Error% of Eq. 4-6
1	100	0.0025	0.3	0.7mm/1mm	3.9
2	100	0.0025	0.65	0.7mm/1mm	5.1
3	100	0.0025	1	0.7mm/1mm	3.2
4	100	0.005	0.3	0.7mm/1mm	14.4
5	100	0.005	0.65	0.7mm/1mm	6.7
6	100	0.005	1	0.7mm/1mm	2.7
7	50	0.0025	0.3	0.7mm/1mm	0.4
8	50	0.0025	0.65	0.7mm/1mm	1.5
9	50	0.0025	1	0.7mm/1mm	6.8
10	50	0.005	0.3	0.7mm/1mm	1.8
11	50	0.005	0.65	0.7mm/1mm	0.1
12	50	0.005	1	0.7mm/1mm	5.5

4.6 Effect of channel width on droplet size at constant c-phase flow rates; for different viscosities and channel heights

This section addresses the effect of channel width on the droplet size at constant c-phase flow rates. Figure 4-8 and Figure 4-9 show the effect of channel width on droplet size at constant c-phase flow rates for h = 1 and 0.7mm, respectively. Droplet size change at constant c-phase flow rate, either in h = 1 or h = 0.7 mm, was more than that at constant c-phase velocity, as shown in Table 4-4. At constant flow rates, a decrease in channel width not only increased the wall effect but also increments the axial velocity. The increase of wall effect and c-phase velocity at a constant flow rate exerted a stronger viscous force on the droplet compared to that at constant c-phase velocity. As a result, the droplet underwent a greater change at a constant c-phase flow rate.

Figure 4-8 and Figure 4-9 illustrate the effect of c-phase viscosity on the droplet size in the dripping regime. At the same c-phase flow rates, the lower c-phase viscosity decreased the viscous force exerted on the droplet, delaying the droplet pinch-off. Therefore, the lower viscosity led to the generation of larger droplets. Eq. 1-2 clearly shows the inverse correlation of viscosity with the droplet size. However, the effect of viscosity on the droplet size decreased by declining the channel width to 0.3 mm for unknown reasons. Further studies are required to fully understand the effect of viscosity in the plug regime.

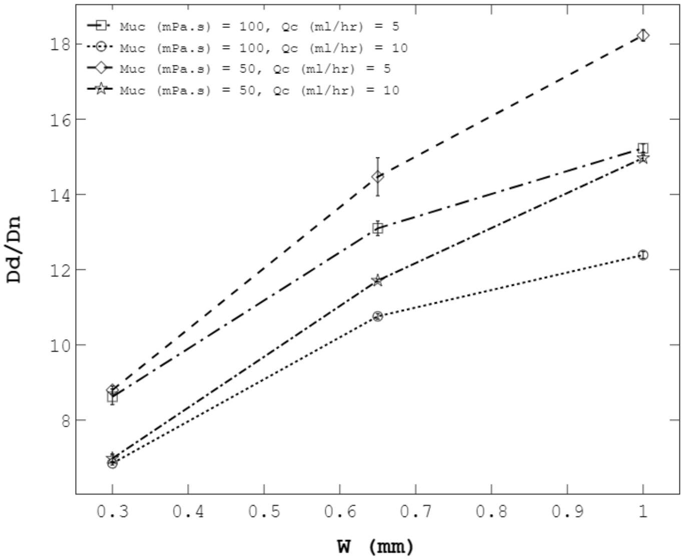

Figure 4-8. Effect of channel width, w, on the droplet size, D_d, at constant c-phase flow rates, Q_c, for h = 1mm. Decreasing channel width at a constant flow rate strongly decreased droplet size due to the increase of wall effect and c-phase velocity.

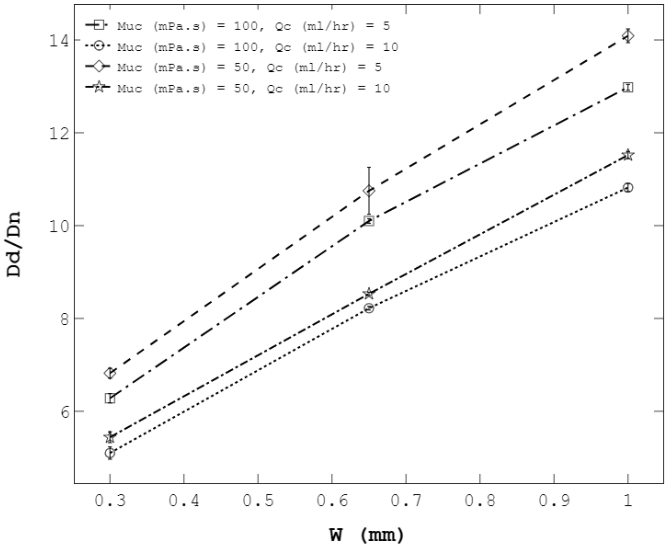

Figure 4-9. Effect of channel width, w, on the droplet size, D_d, at constant c-phase flow rates, Q_c, for h = 0.7 mm. Channel width drastically decreases the droplet size (52 to 53%) at h = 0.7 mm because c-phase bypassed the droplet hardly.

Table 4-4. Comparing range of droplet size, D_d, and droplet size change when channel width, w, changes from 1 to 0.3 mm at constant c-phase velocity, u_c, and constant c-phase viscosity, Q_c.

#	Condition	μ_c [cSt]	h [mm]	u_c range [mm/s]	Q_c range [ml/hr]	D_d range [μm]	D_d change [%]
1	u_c = 2.5 mm/s	100	1	NA	4-8.4	201	35
2	u_c = 5 mm/s	100	1	NA	8.1-16.8	156	34
3	Q_c = 5 ml/hr	100	1	1.5 - 3.1	NA	264	43
4	Q_c = 10 ml/hr	100	1	3 - 6.2	NA	222	45
5	u_c = 2.5 mm/s	50	1	NA	4-8.4	232	38
6	u_c = 5 mm/s	50	1	NA	8.1-16.8	211	42
7	Q_c = 5 ml/hr	50	1	1.5 - 3.1	NA	377	52
8	Q_c = 10 ml/hr	50	1	3 - 6.2	NA	320	53
9	u_c = 2.5 mm/s	100	0.7	NA	4-2-6-3	195	40
10	u_c = 5 mm/s	100	0.7	NA	8.4-12.5	172	44
11	Q_c = 5 ml/hr	100	0.7	2 - 3.0	NA	268	52
12	Q_c = 10 ml/hr	100	0.7	4 - 6.0	NA	229	53
13	u_c = 2.5 mm/s	50	0.7	NA	4-2-6-3	232	43
14	u_c = 5 mm/s	50	0.7	NA	8.4-12.5	204	47
15	Q_c = 5 ml/hr	50	0.7	2 - 3.0	NA	291	52
16	Q_c = 10 ml/hr	50	0.7	4 - 6.0	NA	243	53

4.7 Effect of channel width on droplet size for different d-phase flow rates

The last parameter to study is the d-phase flow rate. This study supports previous reports [79], [82] on the weak effect of Q_d on droplet size. Figure 4-10 shows the effect of channel width on droplet size for 3 levels of Q_d. For all Q_c values, when Q_d doubled from 1 to 2 ml/hr, the maximum change in droplet size was about 5%. This slight change was because, when Q_d was lower than 2 ml/hr, $We_d<O(0.1)$, droplets were still generated in the dripping regime [79] in which Q_d did not significantly alter the force balance of viscous and interfacial tension forces (Eq. 4-2). But, when Q_d increased to 4 ml/hr, droplet sizes increased by 9-24% depending on the value of Q_c and w. Also, the average polydispersity increased from 1.3% to 2.9%. The reason for these changes was the transition to the wide jetting regime at $Q_d = 4$ ml/hr. The same behavior was observed by Shams et al. [84]. They showed when We_d rose from 0.01 to 0.04, the maximum change in droplet size was about 11%, but when We_d increased to 1, the wide jetting regime was formed, and droplet sizes grew by about 34%.

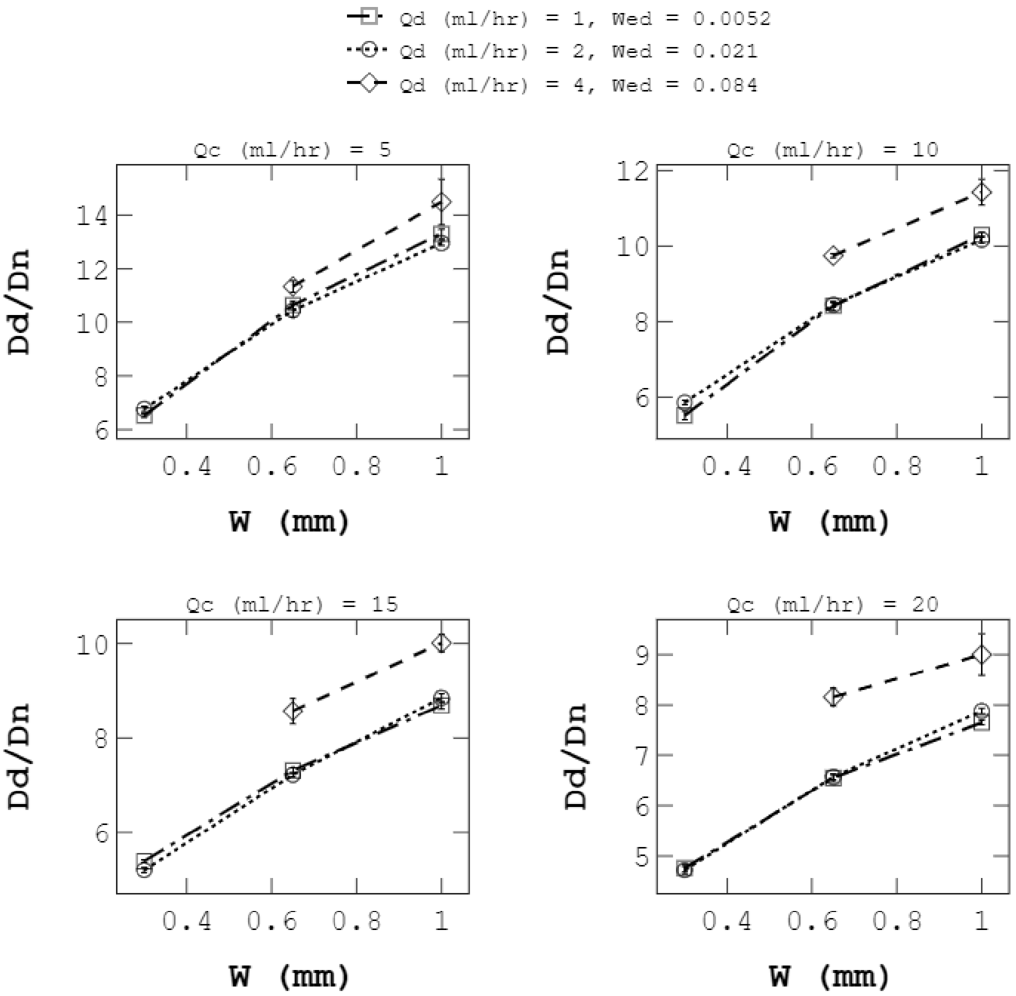

Figure 4-10. Effect of channel width, w, on droplet size, D_d, for different d-phase flow rates, Q_d. D-phase flow rate had a weak effect on droplet size at Q_d = 1 and 2 ml/hr. When Q_d increased from 2 to 4 ml/hr, the droplet size increased by 9-24 % and polydispersity increased.

4.8 Generating droplets for a wide range of sizes

This section explores the ability of the developed device to generate droplets with a wide range of sizes by tuning the channel width. Figure 4-11 shows the droplet diameter versus channel width for 4 levels of c-phase flow rate at μ_c = 50 cSt and h = 1 mm. The channel height of 1 mm was selected to generate droplets up to the size of 1 mm in the dripping regime. However, the regime may have a transition to the plug regime at w = 0.3 mm. The viscosity was set to 50 cSt as the droplet size change is higher at the lower viscosities (see Figure 4-8 and Table 4-4). Based on Figure 4-11, the size of the droplets ranged from 913 µm to 175 µm. The maximum droplet size was 913 µm because the maximum height and width of the channel were 1mm. Generating droplets smaller than 175 µm is possible at higher levels of Q_c due to higher shear rates on the droplet. However, with 4 levels of flow rates from 2 to 50 ml/hr, the range and percentage of droplet size change were 738 µm and 81%, respectively. Such a wide range was achieved without changing materials properties.

Table 4-5 compares the range of droplets generated in this study with previous studies. Here, some of the works provided full details of their experiments in the dripping regime. The device developed by Chu et al. [107] had the widest range (298 µm) in co-flow. The current device extended this range by 148%. Also, Rahimi's device [64] showed the widest range for all methods. Compared to Rahimi's work, the range increased by 111% in the current device because of the flexibility of the walls. One limitation of the device is that the width cannot decrease below 0.3 mm. In the next generation of devices, the droplet range could be increased even further by employing more flexible walls.

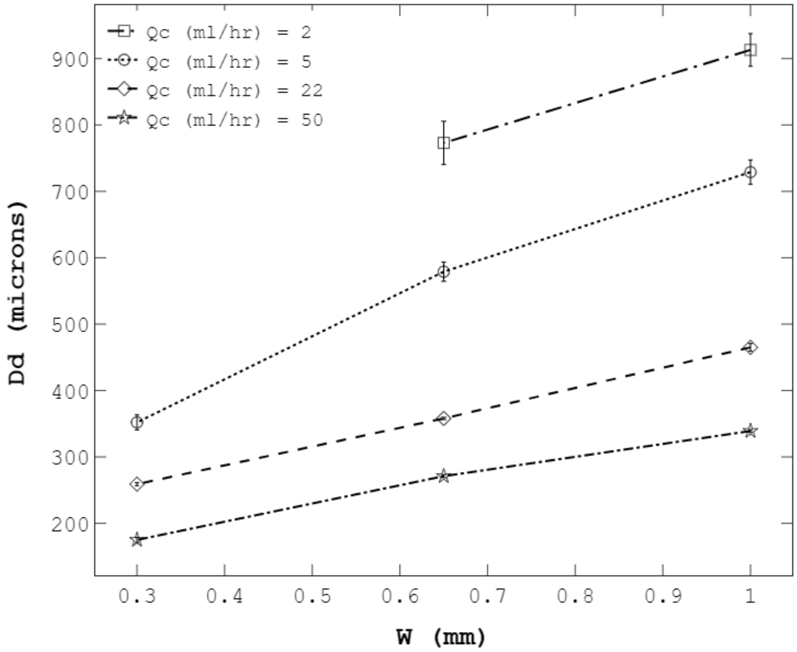

Figure 4-11. Using the flexible wall device for generating droplets with a wide range of sizes at μc=50 cSt and h = 1mm. By changing channel width, w, from 1 to 0.3 mm at 4 levels of c-phase flow rate (Q_c = 2, 5, 22, 50 ml/hr), droplets with the sizes from 913 to 175 μm were generated.

Table 4-5. Comparison of the range of droplet sizes generated in this project with previous works. The range of droplets generated in the proposed device is 738 µm. It is the widest range compared to the previous devices regardless of their methods.

	Case	Dc [µm]	w [µm]	h [µm]	µc [mPa.s]	Dn [µm]	Ca_min	Ca_max	Dd_min [µm]	Dd_max [µm]	Dd_Range [µm]	Dd change [%]	Reference
Flow-focusing method	1	NA	100	100	50	80	0.01235	0.12346	50	100	50	50	Cubaud et al. [2008][61]
	2	NA	49	96	40	126	0.3	5.91	20	60	40	66	Lee et al. [2009]
	3	NA	71	190	40	186	0.21	0.82	65	110	45	41	Lee et al. [2009]
	4	NA	45	68	40	99	0.91	2.3	48	79	31	39	Lee et al. [2009]
	5	450	NA	NA	86.4	250	0.038	0.11	150	500	350	70	Rahimi et. al [2019] [64]
	6	450	NA	NA	86.4	450	0.038	0.11	280	631	351	56	Rahimi et. al [2019] [64]
	7	450	NA	NA	86.4	650	0.05	0.11	590	805	215	36	Rahimi et. al [2019] [64]
T-junction method	8	NA	130	75	56.7	16	0.15	0.54	12	20	8	67	Okushima et al. [2004] [105]
	9	NA	150	90	1	106	0.00300	0.10	74.2	84.8	10.6	14	Okushima et al. [2004] [105]
	10	NA	NA	NA	1	NA	NA	NA	150	225	75	50	Nisisako et al. [2005] [106]
	11	NA	100	33	10	50	0.0012	0.048	85	196	111	131	Garstecki et al. [2006] [70]
	12	NA	100	33	100	50	0.0012	0.24	85	196	111	131	Garstecki et al. [2006] [70]
	13	NA	NA	NA	NA	NA	0.0020	0.010	123	216	92	75	Gupta et al. [2010] [74]
	14	NA	150	50	100	66.6	0.0001	0.50	108	185	77	71	Christopher et al. [2008] [73]
Co-flow method	15	600	NA	NA	NA	40	NA	NA	255	553	298	54	Chu et al. (2007) [107]
	16	559	NA	NA	1.2	41	0.00002	0.00096	280	550	270	49	Erb et al. (2011) [85]
	17	396	NA	NA	1.2	47.4	0.00012	0.0019	223	389	166	43	Erb et al. (2011) [85]
	18	224	NA	NA	1.2	47	0.00037	0.0060	100	200	100	50	Erb et al. (2011) [85]
	19	111	NA	NA	1.2	45.4	0.0015	0.0099	80	100	20	20	Erb et al. (2011) [85]
	20	150	NA	NA	1	40	0.00034	0.010	126	241	115	48	Perro et al. (2011) [86]
	21	300	NA	NA	49.5	40	0.11	0.51	80	168	166	43	Deng et al. (2017) [82]
	22	NA	300 to 1000	1000	100	40	0.00085	0.044	175	913	738	81	This project

4.9 Droplet generation frequency

Droplet generation frequency (f) is inversely affected by the droplet volume (V_d) and is directly appropriate to the d-phase flow rate ($f \sim Q_d/V_d$). Weber number ($We_d = \rho_d u_d^2 D_n/\Upsilon$) is capped at 0.1 in the dripping regime. Because of this, the d-phase flow rate (Q_d) cannot exceed a certain value that depends on the material properties and geometry. Droplet volume is inversely proportional to the cube of droplet diameter. Therefore, droplet generation frequency in the dripping regime highly depends on the droplet size ($f \sim 1/D_d^3$). Table 4-6 compares the droplet generation frequency of the current work with the previous works. Erb et al. [85] generated droplets with the maximum frequency of 1036 1/s because they generated the smallest droplets in the list (80 µm). In the current device, the maximum droplet generation frequency was about 185 1/s when droplets with the sizes of 175 µm were generated. The droplet size frequency in the current device is expected to reach 1039 1/s if the c-phase flow rate is increased, generating droplets of 80 µm. Therefore, the present device can generate droplets with the same frequency as previous devices. Droplet generation frequency can be increased to some extent by the parallelized microfluidic emulsifiers.

Table 4-6 Comparing droplet generation frequency of current device with previous co-flow devices. Erb et al.'s device has the highest throughput because it generated the minimum droplet size (80 µm) in the list. The current device can generate droplets with the same throughput if droplet size decreases to 80 µm.

Case	Qc,min [ml/min]	Qc, max [ml/min]	Q_{d_min} [ml/min]	Q_{d_max} [ml/min]	Dd_min [µm]	Dd_max [µm]	Dd_Range [µm]	f_{min} [1/s]	F_{max} [1/s]	Reference
1	0.016	0.660	0.0167	0.0167	280	550	270	3.2	32	Erb et al. (2011)_1 [85]
2	0.041	0.660	0.0167	0.0167	223	389	166	9.0	47.9	Erb et al. (2011)_2 [85]
3	0.041	0.660	0.0167	0.0167	100	200	100	66.3	530.8	Erb et al. (2011)_3 [85]
4	0.041	0.267	0.0167	0.0167	80	100	20	530.8	1036.7	Erb et al. (2011)_4 [85]
5	0.001	0.030	0.001	0.001	126	241	115	2.3	15.9	Perro et al. (2011) [86]
6	0.700	3.400	0.0005	0.0005	80	168	166	3.4	31.1	Deng et al. (2017) [82]
7	0.1	1.0	0.01	0.01	666	833	298	1.0	6.0	Vijayan et al. (2019) [87]
8	0.033	0.83	0.0167	0.05	175	913	738	0.7	185	This project

4.10 Droplet size prediction model

Buckingham's Π theorem was used to define dimensionless numbers to develop a model for the prediction of droplet diameter. Droplet sizes can be a function of 9 parameters as shown:

$$D_d = f(\mu_c, u_c, \gamma, w, h, \rho_c, u_d, D_n, \rho_d) \tag{4-7}$$

where $\mu_c, u_c, \gamma, w, h, \rho_c, u_d, D_n, \rho_d$ denote c-phase viscosity, c-phase velocity, interfacial tension, channel width, channel height, c-phase density, d-phase velocity, d-phase nozzle diameter, and d-phase density, respectively. Primary dimensions are selected to be R_1= u_c, R_2=ϒ, and R_3=w. Based on Buckingham's π theorem, D_d can be a function of 9-3=6 dimensionless numbers. After calculating the dimensionless numbers, dimensionless droplet size (D_d/w) can be predicted by these dimensionless numbers:

$$\frac{D_d}{w} = f(\pi_1 = \frac{\mu_c u_c}{\gamma}, \pi_2 = \frac{h}{w}, \pi_3 = \frac{\rho_c u_c^2 w}{\gamma}, \pi_4 = \frac{u_d}{u_c}, \pi_5 = \frac{D_n}{w}, \pi_6 = \frac{\rho_d u_c^2 w}{\gamma}) \tag{4-8}$$

$\pi_1 = Ca_c$ and π_2 are kept as it is in Eq. 4-8. Other dimensionless numbers were combined to make them more relevant to the physics of the problem. π_3 is divided by π_1 to obtain c-phase Reynolds number as one of the dimensionless numbers ($\pi_3' = Re_c = \frac{\rho_c u_c w}{\mu_c}$). In the literature, We_d is a dimensionless number that determines droplet generation regime [1], [79] with subtle effects on droplet size [82]. For these reasons, ${\pi_4}^2\pi_5$ is multiplied by π_6 to have We_d as the fourth dimensionless number (π_4'):

$$\pi_4' = We_d = \pi_4^2 \times \pi_5 \times \pi_6 = \left(\frac{u_d}{u_c}\right)^2 \left(\frac{D_n}{w}\right)\left(\frac{\rho_d u_c^2 w}{\gamma}\right) = \frac{\rho_d u_d^2 D_n}{\gamma} \tag{4-9}$$

As a result, droplet size can be explained as a function of these parameters:

$$\frac{D_d}{w} = f(Ca_c, \frac{h}{w}, Re_c, We_d) \tag{4-10}$$

To find the appropriate correlation, D_d/w is plotted against each dimensionless number. Figure 4-12 shows D_d/w versus Ca_c at constant h/w and μ_c. Based on Figure 4-12 and as literature proposes [82], the power function ($\frac{D_d}{w} \sim (Ca_c)^A$) was the best correlation where A is fitting parameter. Figure 4-13 shows D_d/w versus h/w at constant Ca_c and μ_c. According to Figure 4-13, linear function ($\frac{D_d}{w} \sim (\frac{h}{w} + B)$) was the best and most simple equation for the correlation between droplet size and h/w where B is the fitting parameter. For the Re_c, we assumed that the power function can be an appropriate correlation ($\frac{D_d}{w} \sim (Re_{c-phase})^C$) as it can capture nonlinear trends. Parameter C is the fitting parameter.

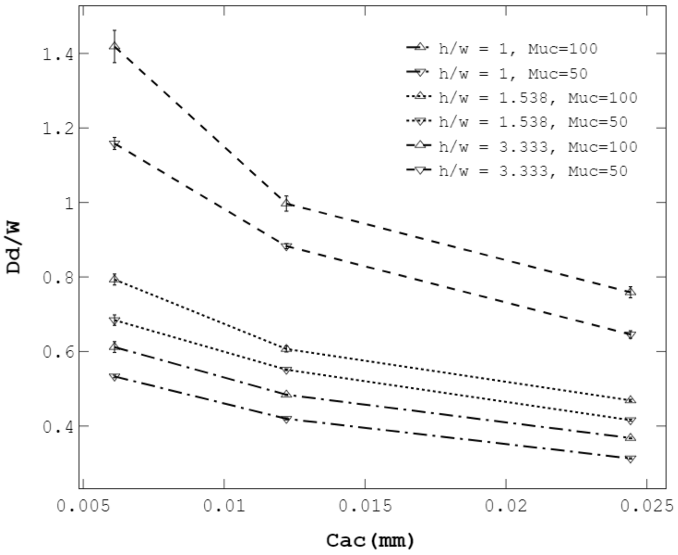

Figure 4-12. Droplet size, D_d, versus c-phase Capillary number, Ca_c, at different h/w, and c-phase viscosities, μ_c. The power function ($(\frac{D_d}{w} \sim (Ca_c)^A)$) was selected for the correlation between D_d and Ca_c where A is a fitting parameter.

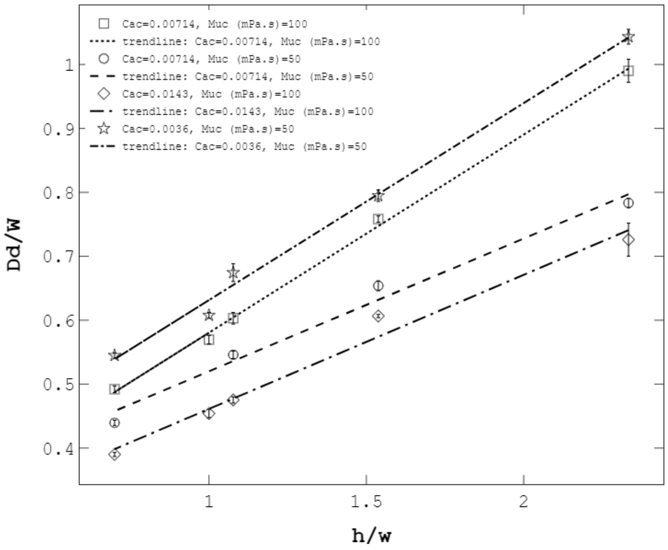

Figure 4-13. Droplet size to channel width ratio, D_d/w, versus channel height to width ratio, h/w, at different c-phase Capillary numbers, Ca_c and c-phase viscosities, μ_c. There is a linear correlation between D_d/w and h/w ($\frac{D_d}{w} \sim (\frac{h}{w} + B)$ where B is a fitting parameter)

Figure 4-14 illustrates the effect of We_d on droplet size. From We_d=0.0052 to We_d=0.021, the maximum change in droplet size was about 3%. However, from We_d=0.021 to We_d=0.084, droplet size suddenly increased (maximally by 15%) due to the transition to a wide jetting regime, as previously discussed in Section 4.7. It can be concluded that We_d weakly affects the droplet size if the regime is dripping or plug.

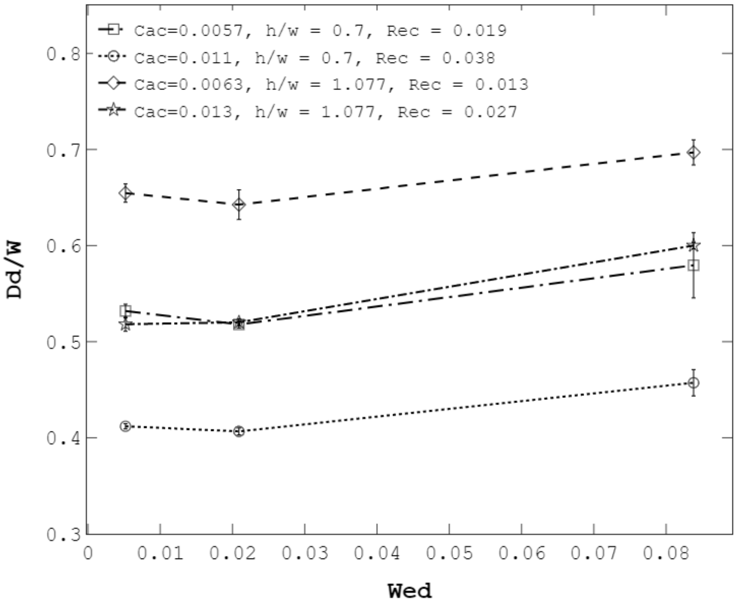

Figure 4-14 Effect of d-phase Weber number, Wed, on the ratio of droplet size to channel size, D_d/w. D-phase Weber number had a weak effect on D_d/w for low We_d, but it increased D_d/w maximally by 15% when We_d ~ O(0.1).

Analysis of variance (ANOVA) was conducted to confirm if We_d has a significant effect on the droplet size. ANOVA can explore a significant difference between two or more groups. At the presence of a significant difference, the p-value is less than 0.05, and the null hypothesis is rejected. The null hypothesis says that there is no difference among group means. Table 4-7 shows the p-values of the test. For Ca_c, h/w, and Re_c, p-values were less than 0.05; thus, we can reject the null hypothesis for these parameters. The P-value for We_d was higher than 0.05, implying the non-significant effect of We_d. As a result, one should consider Ca_c, h/w, and Re_c. In other words:

$$\frac{D_d}{w} = f(Ca_c, \frac{h}{w}, Re_c) \qquad (4\text{-}11)$$

Table 4-7. P-values in the ANOVA test showing the significance of the effect of each parameter on the droplet size, D_d. The P-value for d-phase Weber number (We_d) is more than 0.05, which shows a weak effect of We_d on D_d

Dimensionless numbers	P-Value
Ca_c	0.002
h/w	0.047
Re_c	0.006
We_d	0.256

Therefore, the final form of correlation is Eq. 4-12. The fitting parameters in Eq. 4-13 were calculated based on the minimum root mean square error. Figure 4-15 shows that the proposed equation has an appropriate functional form. Thus, the model can be used for the prediction of intermediate values.

$$\frac{D_d}{w} = DCa^A\left(\frac{h}{w} + B\right)Re^C \qquad (4\text{-}12)$$

$$\frac{D_d}{w} = 0.0415Ca^{-0.235}\left(\frac{h}{w} + 1.696\right)Re^{-0.125} \qquad (4\text{-}13)$$

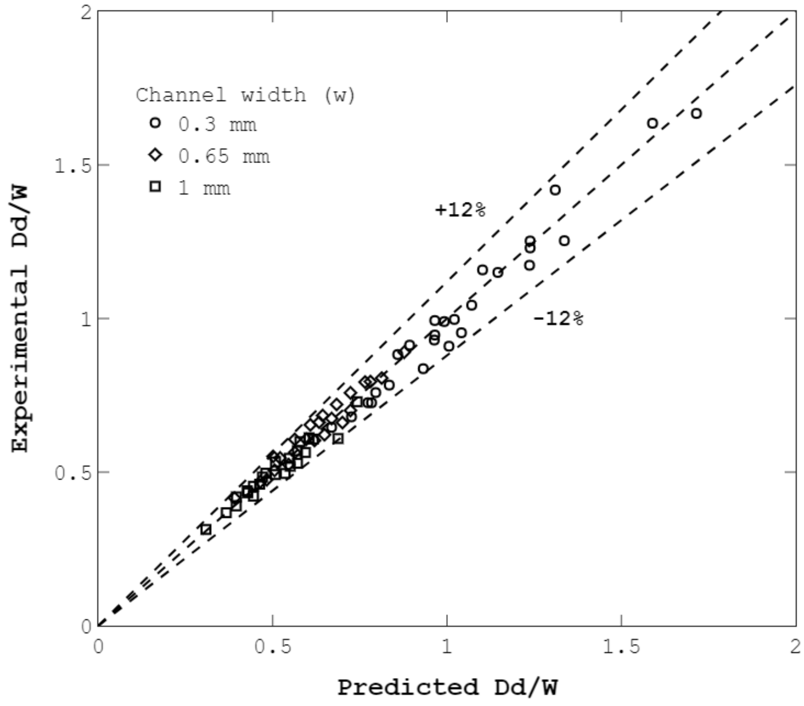

Figure 4-15. Comparison of predicted and experimental results. The maximum error is 11.4 %, and the average error is 3.9 %.

Table 4-8 lists the proposed correlation and the correlations previously developed for the co-flow droplet generation method. It is very difficult to compare the correlation of Eq. 4-13 with the Eq. 4-14 and 4-15. Firstly, these two correlation equations are too simple and lack important parameters required for a good correlation, such as Ca_c, and Re. Secondly, the accuracy of these correlations was not provided for an acceptable amount of data [46], [86]. In contrast to the first two correlations in Table 4-8, Eq. 4-16 is comprehensive and contains necessary dimensionless numbers. Eq. 4-16 shares several key features with the proposed correlation equation in the current project (Eq. 4-13): they are multiplying function, both contain Ca and wall effect parameter, and the error of both correlations is low (the maximum and average error of correlation Eq. 4-16 are 9.2% and 3.8%, respectively [82]). However, Eq. 4-16 is different from Eq. 4-13 in several respects. The most important one is that Eq. 4-13 is proposed for the rectangular channels while Eq. 4-16 was for the circular ones. Thus, a new correlation should be proposed in the current study. In general, a multiplying function containing important dimensionless numbers could be a proper functional form for the prediction of droplet sizes for both circular and rectangular geometries.

Table 4-8. Correlations developed for the co-flow droplet generation method

Equation	Parameters	Equation	Reference
$\frac{D_d}{w} = 0.0415Ca^{-0.235}\left(\frac{h}{w} + 1.696\right)Re^{-0.125}$	w: Channel width h: Channel height	(4-13)	This study
$D_d = D_n^3(a\left({}^{Q_d}/_{Q_c}\right) + b)$	a, b: Fitting parameters	(4-14)	[46]
$D_d = A({}^{Q_c}/_{Q_d})^{-\alpha}$	A, α: Fitting parameters	(4-15)	[86]
$D_d = 0.234.D_nK.Ca_c^{-0.312}.Ca_d^{0.187}.Re_d^{-0.20}$	$K = {}^{0.327}/_{\lambda^{-1.765} + 0.095} + 1.039$ $\lambda = \frac{D_n}{D_c}, Ca_c = {}^{\mu_c u_c}/_{\sigma}$ $Ca_d = {}^{\mu_d u_d}/_{\sigma}, Re_d = {}^{\rho_d D_n u_d}/_{\mu_d}$	(4-16)	[82]

Chapter 5: SUMMARY AND THESIS PROSPECTS

5.1 Summary

This project was aimed to design a co-flow device with flexible walls and evaluate the effect of channel width on droplet size at constant c-phase velocities and c-phase flow rates. First, the effect of channel width was investigated at constant c-phase velocities. For a constant c-phase velocity (i.e., a constant Ca_C), a decrease in channel width (from 1 mm to 0.3 mm) led to a steady decline in the droplet size (34% up to 42%), mainly due to the increase of shear rate. Droplet sizes were directly proportional to the square root of channel width.

Then the effect of channel width was examined on the droplet size at constant c-phase velocity for different channel heights (h = 0.7 and 1 mm). The parameters of w and h synergistically affected the droplet size through the increase of shear rate in the directions perpendicular to the flow direction. This explains why, for h = 0.7 mm, the droplet sizes declined more (43% up to 47%) compared to h = 1 mm (34% up to 42%) when the channel width decreased from 1 mm to 0.3 mm. Moreover, for a constant channel width, droplet size was directly proportional to the square root of channel heights. The correlations of channel height and channel width with droplet size are the same because both parameters affect droplet size through the wall effect.

Then the effect of channel width on droplet size was explored at constant c-phase flow rates. The percentage of droplet size change was more at constant flow rates (43% up to 53%) when compared with the constant c-phase velocities (35% up to 47%). This is because decreasing channel width in a constant flow rate increased not only the wall effect but also the c-phase velocity.

The effect of channel width on droplet size was also examined for different d-phase flow rates. Several reports showed the weak effect of the d-phase flow rate on droplet size in the dripping regime. Interestingly, the influence of the d-phase flow rate on the droplet size in the plug regime was similar to that of the dripping regime due to the similarity of the dominant forces (viscous and interfacial tension forces) in both regimes.

Furthermore, flexible walls allow generating droplets with a wider size range. The device developed in the current project generated droplets from 913 μm to 175 μm for four levels of c-phase flow rates (Q_c = 2, 5, 22, and 50 ml/hr) and three levels of channel width (w = 1, 0.65, and 0.3 mm).

Finally, Buckingham's Π theorem was used to develop a model for the prediction of the droplet diameters. The proposed model had three dimensionless numbers, Ca_c, h/w, and Re_c showing the effect of interfacial forces, wall effect, and flow conditions on the droplet size, respectively. Comparing the experimental droplet diameter versus predicted droplet diameter showed that the proposed equation had an appropriate functional form, and the model can be used for the prediction of intermediate values.

This work contributes to our understanding of the effect of channel size on droplet size in the co-flow droplet generators. Firstly, this study showed that droplet size could be fine-tuned using a moving-wall structure. Such systems can generate droplets over a wider range. In addition to that, droplets sizes are controlled by changing the local flow conditions. This makes the current device suitable for the applications in which it is intended to change droplet size at a constant flow rate. Secondly, the present study appears to be the first study to investigate the effect of different parameters on the effect of channel size on the droplet size. This study has found that droplet size decreases by decreasing channel width at constant c-phase velocity (or Capillary number) due to the increase of wall effect. Another significant finding was that droplet size can be changed more when channel width is decreased at a constant flow rate.

5.2 Thesis Prospects

The current project presented a device with flexible walls to study the effect of channel width on droplet sizes under different conditions. Further investigations are required in the future as listed below:

- The inclusion of interfacial tension and d-phase viscosity can offer a comprehensive insight into the effects of all parameters on the droplet size.
- One of the limitations of this study was that only two levels of h and μ_c were considered. Further research considering wider ranges of these two parameters is recommended to comprehensively explore their effect on the range of droplet sizes.
- The effect of c-phase viscosity on droplet size was weakened at narrower channel widths. The theoretical description can be obtained with the aid of simulation.
- One of the more significant findings of this study was that declining the channel width from 1 mm to 0.3 mm altered the droplet size by 53%. The range of generated droplets can be further extended by optimizing the device to decrement channel width below 0.3 mm or designing a device with tunable channel height.
- The idea of flexible walls can be used in the two-step double emulsions systems. The middle phase flow rate is mainly used to control the core sizes in these systems. The problem is that the change of the middle phase flow rate also affects the shell size. If one

needs to change the core size without changing the shell size, it is reasonable to use flexible walls as it locally alters flow conditions.

APPENDICES

Appendix A: Effect of parameter DBC (see Figure 3-1) on the stress concentration

In Chapter 3, DBC was one of the design parameters defined as the horizontal gap between the device body and the blocks (Figure A-1). The value of DBC was not selected too small because it increases the stress concentration. Figure A-1 shows a decline in $\sigma_{\text{von-Mises}}$ at the encircled point from 0.038 MPa to 0.024 MPa upon enhancing DBC from 2 to 4 mm. This is the reason that DBC was 4 mm in the conceptual design.

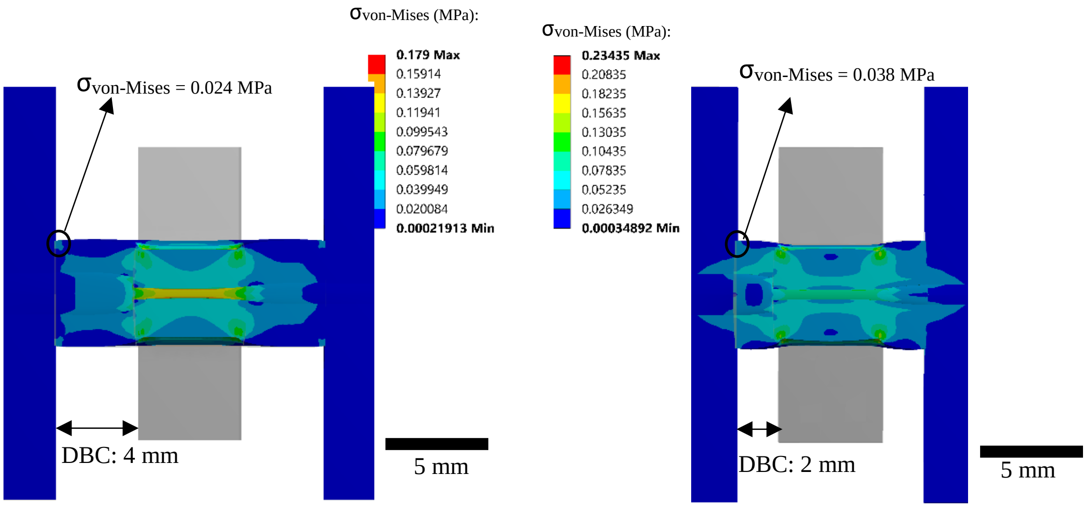

Figure A-1. Von-Mises stress stress, $\sigma_{\text{von-Mises}}$, contour for two levels of DBC (2 and 4 mm) when the blocks move 0.4 mm inwards towards each other. The value of $\sigma_{\text{von-Mises}}$ at the encircled point decreases from 0.038 to 0.024 MPa when DBC increases from 2 to 4 mm.

Appendix B: Boundary conditions and grid independency

Figure B-1. (a) shows the boundary conditions for the simulations in Chapter 3. All sides (except the part squeezed by the blocks) are free with no restrictions. The device is bonded to the glasses from the top and bottom surfaces in parts P1 and P5. Therefore, the boundary conditions of the top and bottom of parts P1 and P5 can be defined as fixed supports. The top and bottom of parts P2, P3, and P4 are not bonded to the glasses, and the surface slides on the glasses in these parts. Therefore, the boundary condition is just fixed along the Y-axis for these surfaces. The side that is squeezed by the blocks can only move along the X-axis for the desired displacement.

Figure B-1. (b) depicts the mesh used for the simulation. The geometry is divided into 3 parts to utilize different mesh sizes for each part. Smaller cells were selected for the middle part (Part 3), where the channel is squeezed to improve the accuracy of the simulation. The computational costs were decremented by using larger cells for the other parts. Figure B-2. (a) shows the channel profile for different mesh sizes and cell numbers (NC). Here the mesh size is the cell size of P3. Figure B-2. (b) shows the average channel width ($w_{average}$) for different NC. The value of $w_{average}$ changed from 0.504 to 0.502 mm (0.3%) when NC was incremented from 6685 to 9590. Therefore, acceptable mesh independence was achieved at NC = 6685.

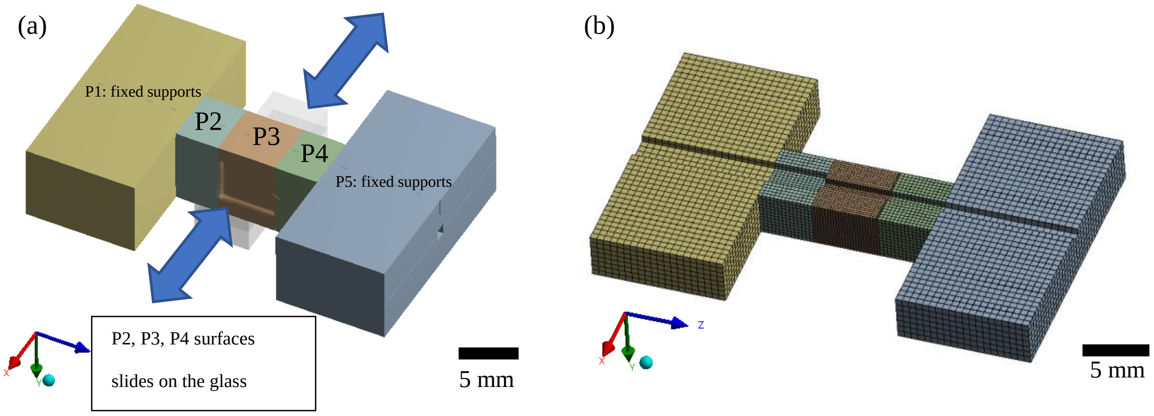

Figure B-1. (a) Boundary conditions, and (b) mesh model used for the FEA to finalize the conceptual design of design.

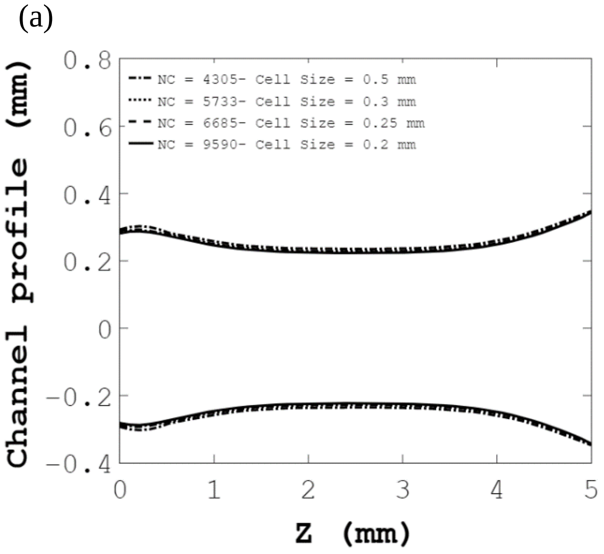

(b)

NC	$w_{average}$ (mm)
4305	0.525
5733	0.510
6685	0.504
9590	0.502

Figure B-2. (a) Channel profile of conceptual design for different mesh sizes (Cell size is the size of middle part), (b) Average channel width for different mesh sizes. Acceptable mesh independence was achieved at NC = 6685

Appendix C: Table of case studies of droplet generation

Case	Muc [mPa.s]	Uc [mm/s]	w [mm]	h [mm]	Qc [ml/hr]	Qd (ml/hr)	h/w	Cac (*10^3)	Rec (*100)	Wed (*10^3)
1	100	2.98	0.3	0.7	5.0	1	2.33	8.50	0.84	5.24
2	100	2.20	0.65	0.7	5.0	1	1.08	6.30	1.35	5.24
3	100	2.00	1	0.7	5.0	1	0.70	5.71	1.88	5.24
4	100	5.95	0.3	0.7	10.0	1	2.33	17.01	1.68	5.24
5	100	4.41	0.65	0.7	10.0	1	1.08	12.59	2.69	5.24
6	100	4.00	1	0.7	10.0	1	0.70	11.42	3.76	5.24
7	100	3.10	0.3	1	5.0	1	3.33	8.86	0.87	5.24
8	100	1.81	0.65	1	5.0	1	1.54	5.16	1.10	5.24
9	100	1.49	1	1	5.0	1	1.00	4.26	1.40	5.24
10	100	6.20	0.3	1	10.0	1	3.33	17.73	1.75	5.24
11	100	3.61	0.65	1	10.0	1	1.54	10.33	2.21	5.24
12	100	2.98	1	1	10.0	1	1.00	8.53	2.81	5.24
13	100	2.50	0.3	0.7	4.2	1	2.33	7.14	0.71	5.24
14	100	2.50	0.65	0.7	5.7	1	1.08	7.14	1.53	5.24
15	100	2.50	1	0.7	6.3	1	0.70	7.14	2.35	5.24
16	100	5.00	0.3	0.7	8.4	1	2.33	14.29	1.41	5.24
17	100	5.00	0.65	0.7	11.3	1	1.08	14.29	3.06	5.24
18	100	2.50	0.3	1	4.0	1	3.33	7.14	0.71	5.24
19	100	5.00	1	0.7	12.5	1	0.70	14.29	4.70	5.24
20	100	2.50	0.65	1	6.9	1	1.54	7.14	1.53	5.24
21	100	2.50	1	1	8.4	1	1.00	7.14	2.35	5.24
22	100	5.00	0.3	1	8.1	1	3.33	14.29	1.41	5.24
23	100	5.00	0.65	1	13.8	1	1.54	14.29	3.06	5.24
24	100	5.00	1	1	16.8	1	1.00	14.29	4.70	5.24
25	50	2.50	0.3	0.7	4.2	1	2.33	3.57	1.41	5.24
26	50	2.50	0.65	0.7	5.7	1	1.08	3.57	3.06	5.24
27	50	2.50	1	0.7	6.3	1	0.70	3.57	4.70	5.24
28	50	5.00	0.3	0.7	8.4	1	2.33	7.14	2.82	5.24
29	50	5.00	0.65	0.7	11.3	1	1.08	7.14	6.11	5.24
30	50	5.00	1	0.7	12.5	1	0.70	7.14	9.40	5.24
31	50	2.50	0.3	1	4.0	1	3.33	3.57	1.41	5.24
32	50	2.50	0.65	1	6.9	1	1.54	3.57	3.06	5.24
33	50	2.50	1	1	8.4	1	1.00	3.57	4.70	5.24
34	50	5.00	0.3	1	8.1	1	3.33	7.14	2.82	5.24
35	50	5.00	0.65	1	13.8	1	1.54	7.14	6.11	5.24
36	50	5.00	1	1	16.8	1	1.00	7.14	9.40	5.24
37	50	2.98	0.3	0.7	5.0	1	2.33	4.25	1.68	5.24
38	50	2.20	0.65	0.7	5.0	1	1.08	3.15	2.69	5.24

39	50	2.00	1	0.7	5.0	1	0.70	2.85	3.76	5.24
40	50	5.95	0.3	0.7	10.0	1	2.33	8.50	3.36	5.24
41	50	4.41	0.65	0.7	10.0	1	1.08	6.30	5.39	5.24
42	50	4.00	1	0.7	10.0	1	0.70	5.71	7.51	5.24
43	50	3.10	0.3	1	5.0	1	3.33	4.43	1.75	5.24
44	50	1.81	0.65	1	5.0	1	1.54	2.58	2.21	5.24
45	50	1.49	1	1	5.0	1	1.00	2.13	2.81	5.24
46	50	6.20	0.3	1	10.0	1	3.33	8.86	3.50	5.24
47	50	3.61	0.65	1	10.0	1	1.54	5.16	4.42	5.24
48	50	2.98	1	1	10.0	1	1.00	4.26	5.61	5.24
49	50	1.25	0.3	1	2.0	1	3.33	1.79	0.71	5.24
50	100	1.25	0.3	1	2.0	1	3.33	3.57	0.35	5.24
51	100	5.00	0.3	1	8.1	1	3.33	14.29	1.41	5.24
52	100	2.00	1	0.7	5.0	1	0.70	5.71	1.88	5.24
53	100	4.00	1	0.7	10.0	1	0.70	11.42	3.76	5.24
54	100	5.99	1	0.7	15.0	1	0.70	17.12	5.63	5.24
55	100	7.99	1	0.7	20.0	1	0.70	22.83	7.51	5.24
56	100	2.00	1	0.7	5.0	2	0.70	5.71	1.88	20.94
57	100	4.00	1	0.7	10.0	2	0.70	11.42	3.76	20.94
58	100	5.99	1	0.7	15.0	2	0.70	17.12	5.63	20.94
59	100	7.99	1	0.7	20.0	2	0.70	22.83	7.51	20.94
60	100	2.00	1	0.7	5.0	4	0.70	5.71	1.88	83.76
61	100	4.00	1	0.7	10.0	4	0.70	11.42	3.76	83.76
62	100	5.99	1	0.7	15.0	4	0.70	17.12	5.63	83.76
63	100	7.99	1	0.7	20.0	4	0.70	22.83	7.51	83.76
64	100	2.20	0.65	0.7	5.0	1	1.08	6.30	1.35	5.24
65	100	4.41	0.65	0.7	10.0	1	1.08	12.59	2.69	5.24
66	100	6.61	0.65	0.7	15.0	1	1.08	18.89	4.04	5.24
67	100	8.82	0.65	0.7	20.0	1	1.08	25.19	5.39	5.24
68	100	2.20	0.65	0.7	5.0	2	1.08	6.30	1.35	20.94
69	100	4.41	0.65	0.7	10.0	2	1.08	12.59	2.69	20.94
70	100	6.61	0.65	0.7	15.0	2	1.08	18.89	4.04	20.94
71	100	8.82	0.65	0.7	20.0	2	1.08	25.19	5.39	20.94
72	100	2.20	0.65	0.7	5.0	4	1.08	6.30	1.35	83.76
73	100	4.41	0.65	0.7	10.0	4	1.08	12.59	2.69	83.76
74	100	6.61	0.65	0.7	15.0	4	1.08	18.89	4.04	83.76
75	100	8.82	0.65	0.7	20.0	4	1.08	25.19	5.39	83.76
76	100	2.98	0.3	0.7	5.0	1	2.33	8.50	0.84	5.24
77	100	5.95	0.3	0.7	10.0	1	2.33	17.01	1.68	5.24
78	100	8.93	0.3	0.7	15.0	1	2.33	25.51	2.52	5.24
79	100	11.90	0.3	0.7	20.0	1	2.33	34.01	3.36	5.24
80	100	2.98	0.3	0.7	5.0	2	2.33	8.50	0.84	20.94
81	100	5.95	0.3	0.7	10.0	2	2.33	17.01	1.68	20.94

82	100	8.93	0.3	0.7	15.0	2	2.33	25.51	2.52	20.94
83	100	11.90	0.3	0.7	20.0	2	2.33	34.01	3.36	20.94
84	50	4.27	1	1	14.3	1	1.00	6.11	8.03	5.24
85	50	8.55	1	1	28.6	1	1.00	12.21	16.07	5.24
86	50	17.09	1	1	57.3	1	1.00	24.42	32.14	5.24
87	50	4.27	0.65	1	11.8	1	1.54	6.11	5.22	5.24
88	50	8.55	0.65	1	23.6	1	1.54	12.21	10.44	5.24
89	50	17.09	0.65	1	47.3	1	1.54	24.42	20.89	5.24
90	50	4.27	0.3	1	6.9	1	3.33	6.11	2.41	5.24
91	50	8.55	0.3	1	13.8	1	3.33	12.21	4.82	5.24
92	50	17.09	0.3	1	27.6	1	3.33	24.42	9.64	5.24
93	100	2.14	1	1	7.2	1	1.00	6.11	2.01	5.24
94	100	4.27	1	1	14.3	1	1.00	12.21	4.02	5.24
95	100	8.55	1	1	28.6	1	1.00	24.42	8.03	5.24
96	100	2.14	0.65	1	5.9	1	1.54	6.11	1.31	5.24
97	100	4.27	0.65	1	11.8	1	1.54	12.21	2.61	5.24
98	100	8.55	0.65	1	23.6	1	1.54	24.42	5.22	5.24
99	100	2.14	0.3	1	3.4	1	3.33	6.11	0.60	5.24
100	100	4.27	0.3	1	6.9	1	3.33	12.21	1.21	5.24
101	100	8.55	0.3	1	13.8	1	3.33	24.42	2.41	5.24

Appendix D: Important forces in the plug regime

As mentioned in the literature review in Chapter 1, the important forces in the dripping regime are the viscous and interfacial tension forces. The purpose of this section is to introduce important forces in the plug regime of this project. In this project, the plug just touched side walls rather than blocking the whole channel, as shown in Figure D-1. This was the major difference in the plug regime of this project with the conventional plug regime in the previous works [70], [72], in which the pressure force was considered as an important force. Figure D-2 schematically illustrates the plug regime in this project. Here, it is assumed that the thread is a cube, and there is a thin film (with a thickness of ε) between the thread and the wall [95]. The pressure force on the back of the thread is equal to ΔpA, where Δp is the pressure drop over the length of the thread (L) and A denotes the surface area of the back of the thread. Δp is calculated by Hagen-Poiseulle equation: $\Delta p \approx \mu_c Q_c L/(2d)^2 w^2$ [1], [70] and the corresponding pressure force is:

$$F_p = \Delta p A \approx \frac{\mu_c Q_c L}{4d^2 w^2} \times h_t w = \frac{\mu_c (u_c 2dw) L}{4d^2 w^2} \times h_t w = \frac{\mu_c u_c L}{2d} \times h_t \tag{A-1}$$

where h_t, d, w, L, and ε are geometric dimensions presented in Figure D-2.

The viscous force on the sides of the plug is much greater than the viscous forces on the top and bottom sides. The viscous force on the lateral sides can be expressed by:

$$F_\tau = \mu_c \frac{\partial u_z}{\partial x} A_{lateral} = \mu_c \frac{u_c}{\mathcal{E}} h_t L \tag{A-2}$$

The ratio of pressure to viscous force is equal to $F_p/F_\tau = \varepsilon/d \ll 1$. Therefore, in contrast to the previous works [70], [72], the pressure force can be ignored against the viscous force because the c-phase bypasses the plug easily through the large gap. Together this analysis shows that the important forces in the plug regime are similar to that in the dripping regime, which are interfacial tension and viscous forces.

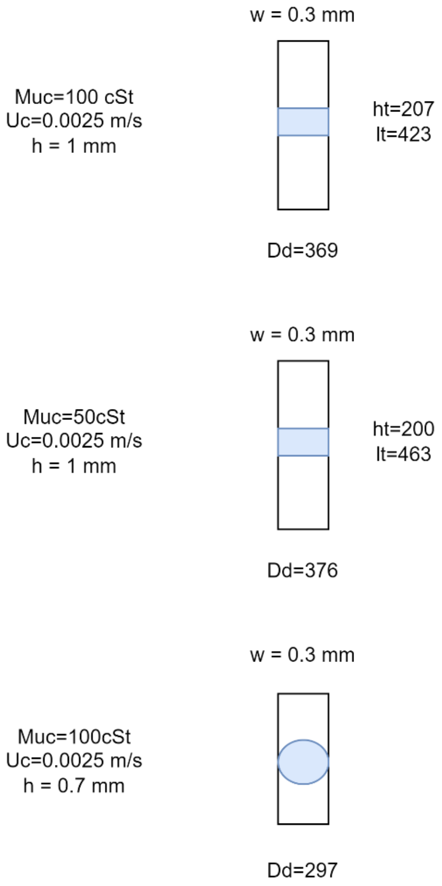

Figure D-1. The distance of plug to the top and bottom of channel (d) under different conditions in the plug regime. C-phase can bypass the plug easily due to the large gap between the plug and the top and bottom surfaces of channel.

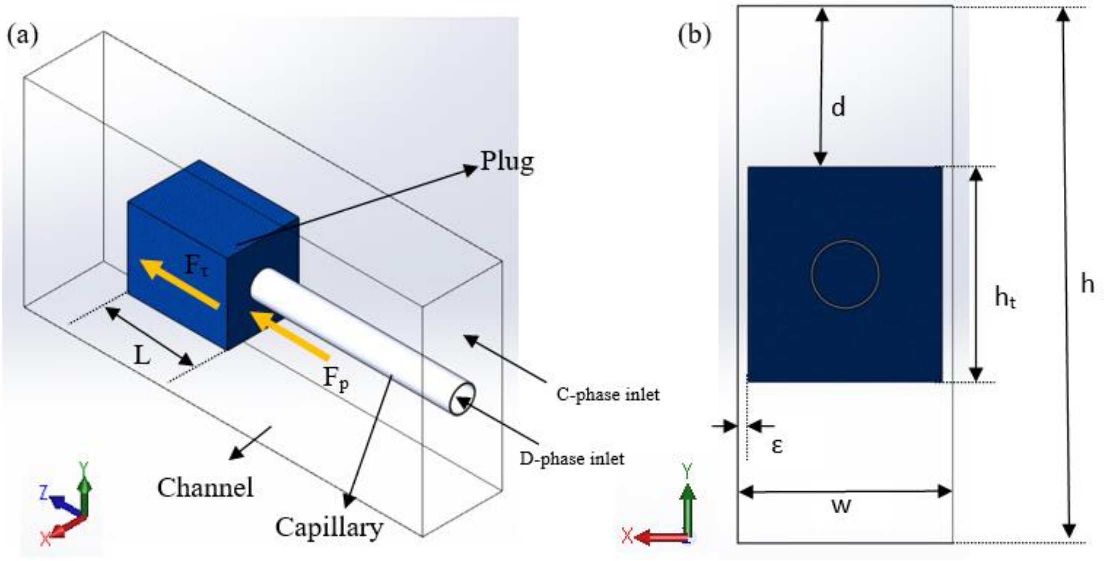

Figure D-2. A schematic drawing of plug regime, (a) Isometric view, (b) Back view. The parameters L, d, h_t*, ε, h, and w are the length of the plug, the distance between the plug and the top or bottom surface of channel, the height of plug, the thin film between the plug and side walls, and the width of the channel, respectively.*

Appendix E: Effect of channel width on droplet size at constant c-phase velocities; for different viscosities and h=0.7 mm

Figure E-1. shows the effect of channel width on the droplet size at constant c-phase velocities and h=0.7 mm. Droplet size alters from 40% to 47% depending on the c-phase viscosity and c-phase velocity.

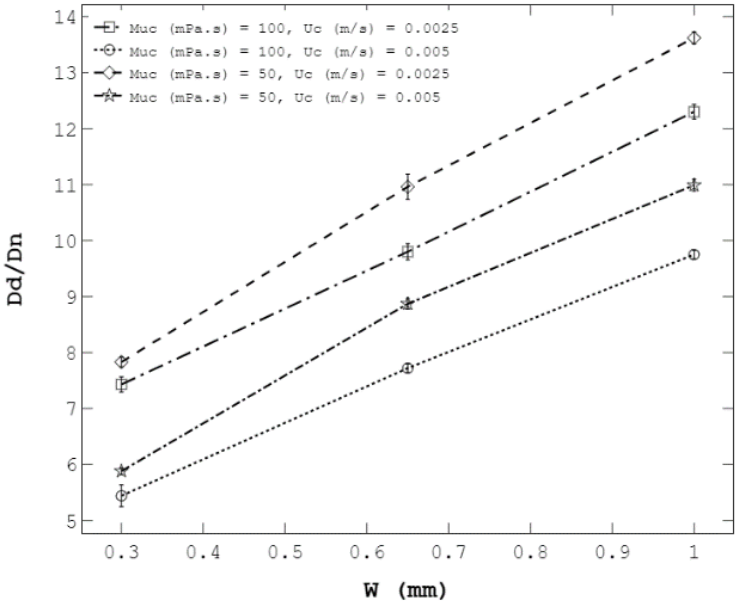

Figure E-1. Effect of channel width, w, on droplet size, D_d, at constant c-phase velocities, u_c; for different c-phase viscosities, μ_c, and h = 0.7 mm

Appendix F: Effect of channel width on droplet size at constant c-phase velocities; for different channel heights and μ_c=50 cSt

Figure F-1. depicts the effect of channel width on the droplet size at constant c-phase velocities and for μ_c=50 cSt. Droplet size shows higher changes for h = 0.7 mm (40% up to 47%) comparing to that for h = 1 mm (38% up to 42%)

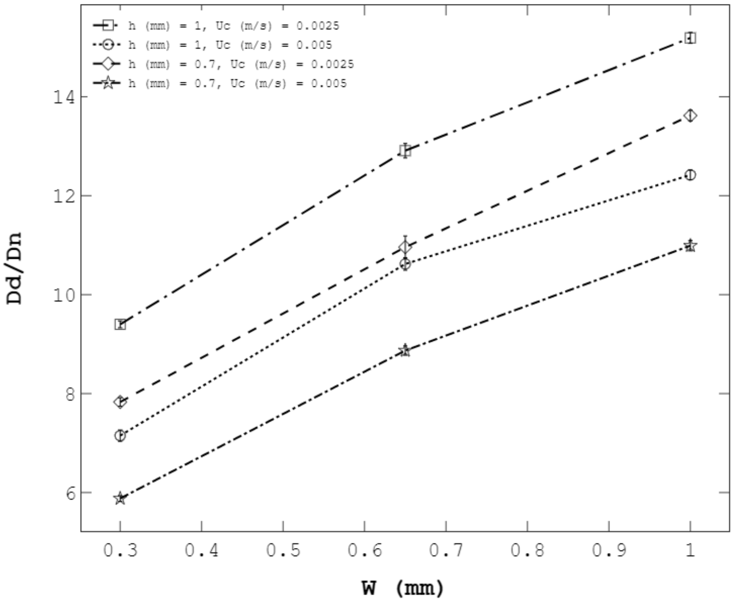

Figure F-1. Effect of channel width, w, on the droplet size, D_d, at constant c-phase velocities, u_c for different channel heights, h, and μ_c=50 cSt

References

[1] C. N. Baroud, F. Gallaire, and R. Dangla, “Dynamics of microfluidic droplets,” *Lab Chip*, vol. 10, no. 16, pp. 2032–2045, 2010.

[2] W.-L. Chou, P.-Y. Lee, C.-L. Yang, W.-Y. Huang, and Y.-S. Lin, “Recent advances in applications of droplet microfluidics,” *Micromachines*, vol. 6, no. 9, pp. 1249–1271, 2015.

[3] L. Shang, Y. Cheng, and Y. Zhao, “Emerging droplet microfluidics,” *Chem. Rev.*, vol. 117, no. 12, pp. 7964–8040, 2017.

[4] S. Hattori *et al.*, “Development of microdroplet generation method for organic solvents used in chemical synthesis,” *Molecules*, vol. 25, no. 22, p. 5360, 2020.

[5] H. Norian, R. M. Field, I. Kymissis, and K. L. Shepard, “An integrated CMOS quantitative-polymerase-chain-reaction lab-on-chip for point-of-care diagnostics,” *Lab Chip*, vol. 14, no. 20, pp. 4076–4084, 2014.

[6] A. Golberg, M. L. Yarmush, and T. Konry, “Picoliter droplet microfluidic immunosorbent platform for point-of-care diagnostics of tetanus,” *Microchim. Acta*, vol. 180, no. 9–10, pp. 855–860, 2013.

[7] J. Pessi, H. A. Santos, I. Miroshnyk, D. A. Weitz, and S. Mirza, “Microfluidics-assisted engineering of polymeric microcapsules with high encapsulation efficiency for protein drug delivery,” *Int. J. Pharm.*, vol. 472, no. 1–2, pp. 82–87, 2014.

[8] B. Herranz-Blanco *et al.*, “Microfluidic assembly of multistage porous silicon–lipid vesicles for controlled drug release,” *Lab Chip*, vol. 14, no. 6, pp. 1083–1086, 2014.

[9] H. Song, D. L. Chen, and R. F. Ismagilov, “Reactions in droplets in microfluidic channels,” *Angew. chemie Int. Ed.*, vol. 45, no. 44, pp. 7336–7356, 2006.

[10] P. Rademeyer, D. Carugo, J. Y. Lee, and E. Stride, “Microfluidic system for high throughput characterisation of echogenic particles,” *Lab Chip*, vol. 15, no. 2, pp. 417–428, 2015.

[11] W. J. Duncanson, L. R. Arriaga, W. L. Ung, J. A. Kopechek, T. M. Porter, and D. A. Weitz, “Microfluidic fabrication of perfluorohexane-shelled double emulsions for controlled loading and acoustic-triggered release of hydrophilic agents,” *Langmuir*, vol. 30, no. 46, pp. 13765–13770, 2014.

[12] P. S. Sheeran, J. D. Rojas, C. Puett, J. Hjelmquist, C. B. Arena, and P. A. Dayton, “Contrast-enhanced ultrasound imaging and in vivo circulatory kinetics with low-boiling-point nanoscale phase-change perfluorocarbon agents,” *Ultrasound Med. Biol.*, vol. 41, no. 3, pp. 814–831, 2015.

[13] A. A. Maan, A. Nazir, M. K. I. Khan, R. Boom, and K. Schroën, “Microfluidic emulsification in food processing,” *J. Food Eng.*, vol. 147, pp. 1–7, 2015.

[14] H. M. Shewan and J. R. Stokes, “Review of techniques to manufacture micro-hydrogel particles for the food industry and their applications,” *J. Food Eng.*, vol. 119, no. 4, pp. 781–792, 2013.

[15] K. Keshoju and L. Sun, “Mechanical characterization of magnetic nanowire–polydimethylsiloxane composites,” *J. Appl. Phys.*, vol. 105, no. 2, p. 23515, 2009.

[16] T. S. Shim, S. Kim, and S. Yang, “Elaborate design strategies toward novel microcarriers for controlled encapsulation and release,” *Part. Part. Syst. Charact.*, vol. 30, no. 1, pp. 9–45, 2013.

[17] I. Polenz, Q. Brosseau, and J.-C. Baret, “Monitoring reactive microencapsulation dynamics using microfluidics,” *Soft Matter*, vol. 11, no. 15, pp. 2916–2923, 2015.

[18] G. T. Vladisavljević *et al.*, “Industrial lab-on-a-chip: Design, applications and scale-up for drug discovery and delivery,” *Adv. Drug Deliv. Rev.*, vol. 65, no. 11–12, pp. 1626–1663, 2013.

[19] A. M. Gañán-Calvo, J. M. Montanero, L. Martín-Banderas, and M. Flores-Mosquera, “Building functional materials for health care and pharmacy from microfluidic principles and flow focusing,” *Adv. Drug Deliv. Rev.*, vol. 65, no. 11–12, pp. 1447–1469, 2013.

[20] W. E. I. Wang, M.-J. Zhang, and L.-Y. Chu, “Functional polymeric microparticles engineered from controllable microfluidic emulsions,” *Acc. Chem. Res.*, vol. 47, no. 2, pp. 373–384, 2014.

[21] S. Seiffert, “Small but smart: sensitive microgel capsules,” *Angew. Chemie Int. Ed.*, vol. 52, no. 44, pp. 11462–11468, 2013.

[22] S. M. Joscelyne and G. Trägårdh, “Membrane emulsification—a literature review,” *J. Memb. Sci.*, vol. 169, no. 1, pp. 107–117, 2000.

[23] G. T. Vladisavljević, I. Kobayashi, and M. Nakajima, “Production of uniform droplets using membrane, microchannel and microfluidic emulsification devices,” *Microfluid. Nanofluidics*, vol. 13, no. 1, pp. 151–178, 2012.

[24] A. Manz *et al.*, “Planar chips technology for miniaturization and integration of separation techniques into monitoring systems: capillary electrophoresis on a chip,” *J. Chromatogr. A*, vol. 593, no. 1–2, pp. 253–258, 1992.

[25] J. Tong, M. Nakajima, H. Nabetani, Y. Kikuchi, and Y. Maruta, “Production of oil-in-water microspheres using a stainless steel microchannel,” *J. Colloid Interface Sci.*, vol. 237, no. 2, pp. 239–248, 2001.

[26] H. Liu, M. Nakajima, T. Nishi, and T. Kimura, “Effect of channel structure on preparation of a water-in-oil emulsion by polymer microchannels,” *Eur. J. lipid Sci. Technol.*, vol. 107, no. 7-8, pp. 481–487, 2005.

[27] S.-K. Hsiung, C.-T. Chen, and G.-B. Lee, “Micro-droplet formation utilizing microfluidic flow focusing and controllable moving-wall chopping techniques,” *J. Micromechanics Microengineering*, vol. 16, no. 11, p. 2403, 2006.

[28] Y. Cui, Y. Li, K. Wang, J. Deng, and G. Luo, “High-throughput preparation of uniform tiny droplets in multiple capillaries embedded stepwise microchannels,” *J. Flow Chem.*, vol. 10, no. 1, pp. 271–282, 2020.

[29] I. Kobayashi, Y. Wada, Y. Hori, M. A. Neves, K. Uemura, and M. Nakajima, “Microchannel Emulsification Using Stainless-Steel Chips: Oil Droplet Generation Characteristics,” *Chem. Eng. Technol.*, vol. 35, no. 10, pp. 1865–1871, 2012.

[30] X. Xu *et al.*, “Microfluidic production of nanoscale perfluorocarbon droplets as liquid contrast agents for ultrasound imaging,” *Lab Chip*, vol. 17, no. 20, pp. 3504–3513, 2017.

[31] A. S. Utada, E. L. Lorenceau, D. R. Link, P. D. Kaplan, H. A. Stone, and D. A. Weitz, “Monodisperse double emulsions generated from a microcapillary device,” *Science (80-.).*, vol. 308, no. 5721, pp. 537–541, 2005.

[32] S. A. Nabavi, G. T. Vladisavljević, S. Gu, and E. E. Ekanem, “Double emulsion production in glass capillary microfluidic device: Parametric investigation of droplet generation behaviour,” *Chem. Eng. Sci.*, vol. 130, pp. 183–196, 2015.

[33] S. A. Nabavi, G. T. Vladisavljević, and V. Manović, “Mechanisms and control of single-step microfluidic generation of multi-core double emulsion droplets,” *Chem. Eng. J.*, vol. 322, pp. 140–148, 2017.

[34] Q. Wu *et al.*, “Multiplex coaxial flow focusing for producing multicompartment Janus microcapsules with tunable material compositions and structural characteristics,” *Lab Chip*, vol. 17, no. 18, pp. 3168–3175, 2017.

[35] L. Yobas, S. Martens, W.-L. Ong, and N. Ranganathan, “High-performance flow-focusing geometry for spontaneous generation of monodispersed droplets,” *Lab Chip*, vol. 6, no. 8, pp. 1073–1079, 2006.

[36] S.-Y. Park, T.-H. Wu, Y. Chen, M. A. Teitell, and P.-Y. Chiou, “High-speed droplet generation on demand driven by pulse laser-induced cavitation,” *Lab Chip*, vol. 11, no. 6, pp. 1010–1012, 2011.

[37] P. Gelin *et al.*, “Microfluidic Device for High-Throughput Production of Monodisperse Droplets,” *Ind. Eng. Chem. Res.*, 2020.

[38] D. Bardin, M. R. Kendall, P. A. Dayton, and A. P. Lee, “Parallel generation of uniform

fine droplets at hundreds of kilohertz in a flow-focusing module," *Biomicrofluidics*, vol. 7, no. 3, p. 34112, 2013.

[39] T. Nisisako and T. Torii, "Microfluidic large-scale integration on a chip for mass production of monodisperse droplets and particles," *Lab Chip*, vol. 8, no. 2, pp. 287–293, 2008.

[40] S. van der Graaf, C. Schroën, and R. M. Boom, "Preparation of double emulsions by membrane emulsification—a review," *J. Memb. Sci.*, vol. 251, no. 1–2, pp. 7–15, 2005.

[41] S. Ma, J. M. Sherwood, W. T. S. Huck, and S. Balabani, "The microenvironment of double emulsions in rectangular microchannels," *Lab Chip*, vol. 15, no. 10, pp. 2327–2334, 2015.

[42] H. Song, J. D. Tice, and R. F. Ismagilov, "A microfluidic system for controlling reaction networks in time," *Angew. Chemie*, vol. 115, no. 7, pp. 792–796, 2003.

[43] B. Rotman, "Measurement of activity of single molecules of β-D-galactosidase," *Proc. Natl. Acad. Sci. U. S. A.*, vol. 47, no. 12, p. 1981, 1961.

[44] D. S. Tawfik and A. D. Griffiths, "Man-made cell-like compartments for molecular evolution," *Nat. Biotechnol.*, vol. 16, no. 7, pp. 652–656, 1998.

[45] M. V Bandulasena, G. T. Vladisavljević, and B. Benyahia, "Versatile reconfigurable glass capillary microfluidic devices with Lego® inspired blocks for drop generation and micromixing," *J. Colloid Interface Sci.*, vol. 542, pp. 23–32, 2019.

[46] L. Chu, A. S. Utada, R. K. Shah, J. Kim, and D. A. Weitz, "Controllable monodisperse multiple emulsions," *Angew. Chemie Int. Ed.*, vol. 46, no. 47, pp. 8970–8974, 2007.

[47] O. Ozen, N. Aubry, D. T. Papageorgiou, and P. G. Petropoulos, "Monodisperse drop formation in square microchannels," *Phys. Rev. Lett.*, vol. 96, no. 14, p. 144501, 2006.

[48] L. Feng, T. Kawahara, Y. Yamanishi, M. Hagiwara, K. Kosuge, and F. Arai, "On-demand and size-controlled production of droplets by magnetically driven microtool," *J. Robot. Mechatronics*, vol. 24, no. 1, pp. 133–140, 2012.

[49] S. Haeberle, R. Zengerle, and J. Ducrée, "Centrifugal generation and manipulation of droplet emulsions," *Microfluid. Nanofluidics*, vol. 3, no. 1, pp. 65–75, 2007.

[50] D. Chakraborty and S. Chakraborty, "Controlled microbubble generation on a compact disk," *Appl. Phys. Lett.*, vol. 97, no. 23, p. 234103, 2010.

[51] C. N. Baroud, M. R. de Saint Vincent, and J.-P. Delville, "An optical toolbox for total control of droplet microfluidics," *Lab Chip*, vol. 7, no. 8, pp. 1029–1033, 2007.

[52] M. R. de Saint Vincent and J.-P. Delville, "Microfluidic transport driven by opto-thermal

effects," *Adv. Microfluid.*, 2012.

[53] M. R. de Saint Vincent, H. Chraibi, and J.-P. Delville, "Optical flow focusing: Light-induced destabilization of stable liquid threads," *Phys. Rev. Appl.*, vol. 4, no. 4, p. 44005, 2015.

[54] S. M. S. Murshed, S. H. Tan, N. T. Nguyen, T. N. Wong, and L. Yobas, "Microdroplet formation of water and nanofluids in heat-induced microfluidic T-junction," *Microfluid. Nanofluidics*, vol. 6, no. 2, pp. 253–259, 2009.

[55] S.-H. Tan, S. M. S. Murshed, N.-T. Nguyen, T. N. Wong, and L. Yobas, "Thermally controlled droplet formation in flow focusing geometry: formation regimes and effect of nanoparticle suspension," *J. Phys. D. Appl. Phys.*, vol. 41, no. 16, p. 165501, 2008.

[56] S. M. S. Murshed, S.-H. Tan, and N.-T. Nguyen, "Temperature dependence of interfacial properties and viscosity of nanofluids for droplet-based microfluidics," *J. Phys. D. Appl. Phys.*, vol. 41, no. 8, p. 85502, 2008.

[57] P. Zhu, X. Tang, and L. Wang, "Droplet generation in co-flow microfluidic channels with vibration," *Microfluid. Nanofluidics*, vol. 20, no. 3, p. 47, 2016.

[58] S. L. Anna, N. Bontoux, and H. A. Stone, "Formation of dispersions using 'flow focusing' in microchannels," *Appl. Phys. Lett.*, vol. 82, no. 3, pp. 364–366, 2003.

[59] R. Dreyfus, P. Tabeling, and H. Willaime, "Ordered and disordered patterns in two-phase flows in microchannels," *Phys. Rev. Lett.*, vol. 90, no. 14, p. 144505, 2003.

[60] T. Ward, M. Faivre, M. Abkarian, and H. A. Stone, "Microfluidic flow focusing: Drop size and scaling in pressure versus flow-rate-driven pumping," *Electrophoresis*, vol. 26, no. 19, pp. 3716–3724, 2005.

[61] T. Cubaud and T. G. Mason, "Capillary threads and viscous droplets in square microchannels," *Phys. fluids*, vol. 20, no. 5, p. 53302, 2008.

[62] W. Lee, L. M. Walker, and S. L. Anna, "Role of geometry and fluid properties in droplet and thread formation processes in planar flow focusing," *Phys. Fluids*, vol. 21, no. 3, p. 32103, 2009.

[63] D. Funfschilling, H. Debas, H.-Z. Li, and T. G. Mason, "Flow-field dynamics during droplet formation by dripping in hydrodynamic-focusing microfluidics," *Phys. Rev. E*, vol. 80, no. 1, p. 15301, 2009.

[64] M. Rahimi, A. S. Khorrami, and P. Rezai, "Effect of device geometry on droplet size in co-axial flow-focusing microfluidic droplet generation devices," *Colloids Surfaces A Physicochem. Eng. Asp.*, vol. 570, pp. 510–517, 2019.

[65] M. Rahimi, S. Yazdanparast, and P. Rezai, "Parametric study of droplet size in an

axisymmetric flow-focusing capillary device," *Chinese J. Chem. Eng.*, vol. 28, no. 4, pp. 1016–1022, 2020.

[66] T. Thorsen, R. W. Roberts, F. H. Arnold, and S. R. Quake, "Dynamic pattern formation in a vesicle-generating microfluidic device," *Phys. Rev. Lett.*, vol. 86, no. 18, p. 4163, 2001.

[67] S. Van der Graaf, M. L. J. Steegmans, R. G. M. Van Der Sman, C. Schroën, and R. M. Boom, "Droplet formation in a T-shaped microchannel junction: a model system for membrane emulsification," *Colloids Surfaces A Physicochem. Eng. Asp.*, vol. 266, no. 1–3, pp. 106–116, 2005.

[68] J. D. Wehking, M. Gabany, L. Chew, and R. Kumar, "Effects of viscosity, interfacial tension, and flow geometry on droplet formation in a microfluidic T-junction," *Microfluid. Nanofluidics*, vol. 16, no. 3, pp. 441–453, 2014.

[69] M. Y. A. Jamalabadi, M. DaqiqShirazi, A. Kosar, and M. S. Shadloo, "Effect of injection angle, density ratio, and viscosity on droplet formation in a microfluidic T-junction," *Theor. Appl. Mech. Lett.*, vol. 7, no. 4, pp. 243–251, 2017.

[70] P. Garstecki, M. J. Fuerstman, H. A. Stone, and G. M. Whitesides, "Formation of droplets and bubbles in a microfluidic T-junction—scaling and mechanism of break-up," *Lab Chip*, vol. 6, no. 3, pp. 437–446, 2006.

[71] G. F. Christopher and S. L. Anna, "Microfluidic methods for generating continuous droplet streams," *J. Phys. D. Appl. Phys.*, vol. 40, no. 19, p. R319, 2007.

[72] M. De Menech, P. Garstecki, F. Jousse, and H. A. Stone, "Transition from squeezing to dripping in a microfluidic T-shaped junction," *J. Fluid Mech.*, vol. 595, pp. 141–161, 2008.

[73] G. F. Christopher, N. N. Noharuddin, J. A. Taylor, and S. L. Anna, "Experimental observations of the squeezing-to-dripping transition in T-shaped microfluidic junctions," *Phys. Rev. E*, vol. 78, no. 3, p. 36317, 2008.

[74] A. Gupta and R. Kumar, "Effect of geometry on droplet formation in the squeezing regime in a microfluidic T-junction," *Microfluid. Nanofluidics*, vol. 8, no. 6, pp. 799–812, 2010.

[75] J. Sivasamy, T.-N. Wong, N.-T. Nguyen, and L. T.-H. Kao, "An investigation on the mechanism of droplet formation in a microfluidic T-junction," *Microfluid. Nanofluidics*, vol. 11, no. 1, pp. 1–10, 2011.

[76] N. Tarchichi, F. Chollet, and J.-F. Manceau, "New regime of droplet generation in a T-shape microfluidic junction," *Microfluid. Nanofluidics*, vol. 14, no. 1–2, pp. 45–51, 2013.

[77] H. Yang, Q. Zhou, and L.-S. Fan, "Three-dimensional numerical study on droplet formation and cell encapsulation process in a micro T-junction," *Chem. Eng. Sci.*, vol. 87,

pp. 100–110, 2013.

[78] C. Cramer, P. Fischer, and E. J. Windhab, “Drop formation in a co-flowing ambient fluid,” *Chem. Eng. Sci.*, vol. 59, no. 15, pp. 3045–3058, 2004.

[79] A. S. Utada, A. Fernandez-Nieves, H. A. Stone, and D. A. Weitz, “Dripping to jetting transitions in coflowing liquid streams,” *Phys. Rev. Lett.*, vol. 99, no. 9, p. 94502, 2007.

[80] P. Guillot, A. Colin, A. S. Utada, and A. Ajdari, “Stability of a jet in confined pressure-driven biphasic flows at low Reynolds numbers,” *Phys. Rev. Lett.*, vol. 99, no. 10, p. 104502, 2007.

[81] A. S. Utada, A. Fernandez-Nieves, J. M. Gordillo, and D. A. Weitz, “Absolute instability of a liquid jet in a coflowing stream,” *Phys. Rev. Lett.*, vol. 100, no. 1, p. 14502, 2008.

[82] C. Deng, H. Wang, W. Huang, and S. Cheng, “Numerical and experimental study of oil-in-water (O/W) droplet formation in a co-flowing capillary device,” *Colloids Surfaces A Physicochem. Eng. Asp.*, vol. 533, pp. 1–8, 2017.

[83] A. S. Khorrami and P. Rezai, “Oscillating dispersed-phase co-flow microfluidic droplet generation: jet length reduction effect,” *Soft Matter*, vol. 14, no. 48, pp. 9870–9876, 2018.

[84] A. Shams Khorrami and P. Rezai, “Oscillating dispersed-phase co-flow microfluidic droplet generation: Multi-droplet size effect,” *Biomicrofluidics*, vol. 12, no. 3, p. 34113, 2018.

[85] R. M. Erb, D. Obrist, P. W. Chen, J. Studer, and A. R. Studart, “Predicting sizes of droplets made by microfluidic flow-induced dripping,” *Soft Matter*, vol. 7, no. 19, pp. 8757–8761, 2011.

[86] A. Perro, C. Nicolet, J. Angly, S. Lecommandoux, J.-F. Le Meins, and A. Colin, “Mastering a double emulsion in a simple co-flow microfluidic to generate complex polymersomes,” *Langmuir*, vol. 27, no. 14, pp. 9034–9042, 2011.

[87] S. Vijayan and M. Hashimoto, “3D printed fittings and fluidic modules for customizable droplet generators,” *RSC Adv.*, vol. 9, no. 5, pp. 2822–2828, 2019.

[88] M. B. Romanowsky, A. R. Abate, A. Rotem, C. Holtze, and D. A. Weitz, “High throughput production of single core double emulsions in a parallelized microfluidic device,” *Lab Chip*, vol. 12, no. 4, pp. 802–807, 2012.

[89] W. Li, J. Greener, D. Voicu, and E. Kumacheva, “Multiple modular microfluidic (M 3) reactors for the synthesis of polymer particles,” *Lab Chip*, vol. 9, no. 18, pp. 2715–2721, 2009.

[90] T. Nisisako, T. Ando, and T. Hatsuzawa, “High-volume production of single and compound emulsions in a microfluidic parallelization arrangement coupled with coaxial

annular world-to-chip interfaces," *Lab Chip*, vol. 12, no. 18, pp. 3426–3435, 2012.

[91] T. Cubaud and T. G. Mason, "Folding of viscous threads in diverging microchannels," *Phys. Rev. Lett.*, vol. 96, no. 11, p. 114501, 2006.

[92] D. D. Joseph and Y. Y. Renardy, *Fundamentals of two-fluid dynamics: part II: lubricated transport, drops and miscible liquids*, vol. 4. Springer Science & Business Media, 2013.

[93] C. R. Carrigan and J. C. Eichelberger, "Zoning of magmas by viscosity in volcanic conduits," *Nature*, vol. 343, no. 6255, pp. 248–251, 1990.

[94] T. Glawdel, C. Elbuken, and C. L. Ren, "Droplet formation in microfluidic T-junction generators operating in the transitional regime. I. Experimental observations," *Phys. Rev. E*, vol. 85, no. 1, p. 16322, 2012.

[95] J. C. McDonald *et al.*, "Fabrication of microfluidic systems in poly (dimethylsiloxane)," *Electrophor. An Int. J.*, vol. 21, no. 1, pp. 27–40, 2000.

[96] A. Rotem, A. R. Abate, A. S. Utada, V. Van Steijn, and D. A. Weitz, "Drop formation in non-planar microfluidic devices," *Lab Chip*, vol. 12, no. 21, pp. 4263–4268, 2012.

[97] R. Song, M. S. Abbasi, and J. Lee, "Fabrication of 3D printed modular microfluidic system for generating and manipulating complex emulsion droplets," *Microfluid. Nanofluidics*, vol. 23, no. 7, p. 92, 2019.

[98] Z. Zhou, T. Kong, H. Mkaouar, K. N. Salama, and J. M. Zhang, "A hybrid modular microfluidic device for emulsion generation," *Sensors Actuators A Phys.*, vol. 280, pp. 422–428, 2018.

[99] C. Martino, S. Berger, R. C. R. Wootton, and A. J. deMello, "A 3D-printed microcapillary assembly for facile double emulsion generation," *Lab Chip*, vol. 14, no. 21, pp. 4178–4182, 2014.

[100] P. Huerre and P. A. Monkewitz, "Local and global instabilities in spatially developing flows," *Annu. Rev. Fluid Mech.*, vol. 22, no. 1, pp. 473–537, 1990.

[101] J.-M. Chomaz, "Global instabilities in spatially developing flows: non-normality and nonlinearity," *Annu. Rev. Fluid Mech.*, vol. 37, pp. 357–392, 2005.

[102] P. B. Umbanhowar, V. Prasad, and D. A. Weitz, "Monodisperse emulsion generation via drop break off in a coflowing stream," *Langmuir*, vol. 16, no. 2, pp. 347–351, 2000.

[103] R. Seemann, M. Brinkmann, T. Pfohl, and S. Herminghaus, "Droplet based microfluidics," *Reports Prog. Phys.*, vol. 75, no. 1, p. 16601, 2011.

[104] P. Zhu and L. Wang, "Passive and active droplet generation with microfluidics: a review," *Lab Chip*, vol. 17, no. 1, pp. 34–75, 2017.

[105] S. Okushima, T. Nisisako, T. Torii, and T. Higuchi, “Controlled production of monodisperse double emulsions by two-step droplet breakup in microfluidic devices,” *Langmuir*, vol. 20, no. 23, pp. 9905–9908, 2004.

[106] T. Nisisako, S. Okushima, and T. Torii, “Controlled formulation of monodisperse double emulsions in a multiple-phase microfluidic system,” *Soft Matter*, vol. 1, no. 1, p. 23, 2005, doi: 10.1039/b501972a.

[107] C.-H. Lee, S.-K. Hsiung, and G.-B. Lee, “A tunable microflow focusing device utilizing controllable moving walls and its applications for formation of micro-droplets in liquids,” *J. Micromechanics Microengineering*, vol. 17, no. 6, p. 1121, 2007.

[108] Y.-H. Lin, C.-H. Lee, and G.-B. Lee, “Droplet formation utilizing controllable moving-wall structures for double-emulsion applications,” *J. Microelectromechanical Syst.*, vol. 17, no. 3, pp. 573–581, 2008.

[109] H.-W. Wu, Y.-C. Huang, C.-L. Wu, and G.-B. Lee, “Exploitation of a microfluidic device capable of generating size-tunable droplets for gene delivery,” *Microfluid. Nanofluidics*, vol. 7, no. 1, pp. 45–56, 2009.

[110] X. Zhang, “Dynamics of drop formation in viscous flows,” *Chem. Eng. Sci.*, vol. 54, no. 12, pp. 1759–1774, 1999.

[111] X. Chen, T. Glawdel, N. Cui, and C. L. Ren, “Model of droplet generation in flow focusing generators operating in the squeezing regime,” *Microfluid. Nanofluidics*, vol. 18, no. 5–6, pp. 1341–1353, 2015.

[112] A. Sauret and H. C. Shum, “Beating the jetting regime,” *Int. J. Nonlinear Sci. Numer. Simul.*, vol. 13, no. 5, pp. 351–362, 2012.

[113] C. K. Batchelor and G. K. Batchelor, *An introduction to fluid dynamics*. Cambridge university press, 2000.

[114] R. Cliff, J. R. Grace, and M. E. Weber, “Bubbles, Drops and Particles. 1978.” New York: Academic Press.

[115] H. Fox, P. Taylor, and W. Zisman, “Polyorganosiloxanes... surface active properties,” *Ind. Eng. Chem.*, vol. 39, no. 11, pp. 1401–1409, 1947.

[116] F. Peters and D. Arabali, “Interfacial tension between oil and water measured with a modified contour method,” *Colloids Surfaces A Physicochem. Eng. Asp.*, vol. 426, pp. 1–5, 2013.

[117] I. D. Johnston, D. K. McCluskey, C. K. L. Tan, and M. C. Tracey, “Mechanical characterization of bulk Sylgard 184 for microfluidics and microengineering,” *J. Micromechanics Microengineering*, vol. 24, no. 3, p. 35017, 2014.

[118] M. Liu, J. Sun, Y. Sun, C. Bock, and Q. Chen, “Thickness-dependent mechanical properties of polydimethylsiloxane membranes,” *J. micromechanics microengineering*, vol. 19, no. 3, p. 35028, 2009.

[119] J. C. Lötters, W. Olthuis, P. H. Veltink, and P. Bergveld, “The mechanical properties of the rubber elastic polymer polydimethylsiloxane for sensor applications,” *J. micromechanics microengineering*, vol. 7, no. 3, p. 145, 1997.

[120] S. K. Sia and G. M. Whitesides, “Microfluidic devices fabricated in poly (dimethylsiloxane) for biological studies,” *Electrophoresis*, vol. 24, no. 21, pp. 3563–3576, 2003.

[121] J. N. Patel, B. Kaminska, B. L. Gray, and B. D. Gates, “PDMS as a sacrificial substrate for SU-8-based biomedical and microfluidic applications,” *J. Micromechanics Microengineering*, vol. 18, no. 9, p. 95028, 2008.

[122] M. Fleger and A. Neyer, “PDMS microfluidic chip with integrated waveguides for optical detection,” *Microelectron. Eng.*, vol. 83, no. 4–9, pp. 1291–1293, 2006.

[123] N. Kashaninejad, “A New Form of Velocity Distribution in Rectangular Microchannels with Finite Aspect Ratios,” 2019.